CRANFIELD UNIVERSITY

AVANISH MISHRA

NUMERICAL AND EXPERIMENTAL INVESTIGATION OF A CONFINED PLUNGING LIQUID JET SYSTEM

DEPARTMENT OF ENGINEERING AND APPLIED SCIENCE

MSc (Research)

MSc
Academic Year: 2010 - 2011

Supervisor: Dr. Amer Hameed
July 2011

CRANFIELD UNIVERSITY

DEPARTMENT OF ENGINEERING AND APPLIED SCIENCE
MSc (Research)

MSc

Academic Year 2010 - 2011

AVANISH MISHRA

NUMERICAL AND EXPERIMENTAL INVESTIGATION OF A CONFINED PLUNGING LIQUID JET SYSTEM

Supervisor: Dr. Amer Hameed

July 2011

ABSTRACT

In a confined plunging liquid jet (CPLJ) system, a liquid jet is allowed to fall in a partially submerged narrow downcomer tube. Liquid jet impingement at gas-liquid interface leads to entrainment of gas, which is dispersed down the downcomer tube in to outer pool in form of bubbles. This simple phenomenon of gas entrainment bears great industrial significance. It facilitates an efficient gas liquid contacting device, which can be used for waste water aeration and lake destratification etc. In present work, a confined plunging liquid jet system was experimentally and numerically analyzed. On experimental front, a laboratory scale CPLJ setup was developed. Impact of change in jet height, water flow rate and nozzle diameter on, bubble plume size and surrounding flow field was investigated through high speed camera photography and Particle Image Velocimetry. Image processing programs were developed in MATLAB for extracting plume boundaries in high speed camera images. Experimental results showed that, bubble plume width and flow field is only weakly dependent on jet height. With increase in water flow rate, bubble plume size and air lifted water velocity increases. Increase in nozzle diameter, at constant water flow rate and jet height, decreases both the plume size and upward water velocity.

On numerical front, a 3D Euler-Euler two-fluid CFD simulation of bubble plume dispersion was performed for the test case of 7 mm nozzle diameter, 100 mm jet length and 12.5 LPM water flow rate. Grid generation was done in GAMBIT while CFD software ANSYS CFX 12.1 was used for CFD simulations. Air phase was modelled as a polydispersed fluid with eight size bins. In CFD modelling, interfacial drag, lift, wall lubrication and turbulent dispersion forces were incorporated through appropriate correlations. Numerical and experimental results were found to be in agreement with each other. CFD results showed that at least 85% of the inlet air breaks thorough the downcomer tube in to outer water tank.

Keywords:

Aeration, air entrainment, destratification, downcomer, digital image processing

ACKNOWLEDGEMENTS

I would like to express my deep sincere gratitude to my supervisor Dr. Amer Hameed, for providing financial support and his guidance throughout the project duration. Despite his very busy schedule, he was always available to help and guide me.

I am also thankful to Rajeev Bhatnagar for providing suggestions and comments which saved considerable amount of time and shaped the present work.

I am highly grateful to Professor Kevin Knowles and Dr. Alistair Saddington for allowing me to use their lab space and resources for experimental work.

It would have been difficult to finish this work without administrative support of Ros Gibson.

TABLE OF CONTENTS

LIST OF FIGURES

LIST OF TABLES

LIST OF EQUATIONS

NOMENCLATURE

D_C	Downcomer diameter
D_N	Nozzle diameter
H_N	Jet height or jet length
α_k	Void fraction of the k^{th} phase
k	Represents air or water phase
ρ_k	Density of the k^{th} phase
$\vec{U}_k$	Velocity vector for the k^{th} phase
I_k	Interfacial mass transfer term for k^{th} phase
$\mu_{eff,k}$	Effective viscosity of phase k
I	Identity tensor
p	Pressure
τ_k	Shear stress tensor for k^{th} phase
$\vec{g}$	Gravity vector
$\vec{M}_{ik}$	Interfacial momentum transfer term for k^{th} phase
$\vec{M}_{iL}$	Interfacial momentum transfer term for liquid phase
$\vec{M}_{iG}$	Interfacial momentum transfer term for gas phase
$\vec{M}_L^D$	Interfacial drag force
$\vec{M}_L^L$	Interfacial lift force

$\vec{M}_L^{WL}$	Interfacial wall lubrication force
$\vec{M}_L^{VM}$	Interfacial virtual mass force
$\vec{M}_L^{TD}$	Interfacial turbulent dispersion force
C_D	Drag coefficient
α_G	Gas void fraction
ρ_L	Density of liquid phase
d_B	Mean bubble diameter of gas phase
$\vec{U}_G$	Velocity vector of gas phase
$\vec{U}_L$	Velocity vector of liquid phase
V_B	Volume of a bubble
Re_B	Bubble Reynolds Number
σ	Surface tension coefficient between air and water
μ_L	Dynamic viscosity of liquid phase
U_T	Bubble terminal velocity
E_O	Eötvös Number
M_O	Morton Number
μ_{ref}	Reference viscosity in drag force model
$C_{D,1}$	Drag coefficient for flow past a single bubble
n	Volume fraction correction exponent

C_L	Lift force coefficient
E_{O_d}	Modified Eötvös Number
d_H	Characteristic length scale for deformed bubble
C_{WL}	Wall lubrication force coefficient
$\vec{n}_w$	Unit normal vector away from the wall
Y_w	Distance of bubble centre from the wall
C_{w1}, C_{w2}, C_{W3}	Coefficients in wall lubrication force model
C_{WC}	Cut-off coefficient in wall lubrication force model
C_{WD}	Damping coefficient in wall lubrication force model
p_w	Power law constant in wall lubrication force model
C_{VM}	Virtual mass coefficient
$\frac{D_G}{Dt}$	Material derivative with respect to gas phase
$\frac{D_L}{Dt}$	Material derivative with respect to liquid phase
C_{TD}	Turbulent dispersion force coefficient
ν_{tL}	Kinematic eddy viscosity of liquid phase
$\sigma_{\alpha L}$	Turbulent Schmidt Number for liquid phase volume fraction
k_L	Turbulent kinetic energy of liquid phase
ε_L	Turbulent dissipation rate of liquid phase
ω	Specific turbulent dissipation rate of liquid phase

ω_f	Free stream values of specific turbulent dissipation rate
F_1	Blending function in the shear stress transport model
μ_{tL}	Liquid phase dynamic eddy viscosity
μ_{tG}	Gas phase dynamic eddy viscosity
Pr_t	Turbulent Prandtl Number
μ_{tL}^B	Bubble induced eddy viscosity
$\mu_{eff,L}$	Effective viscosity for liquid phase
$\mu_{Lam,L}$	Dynamic viscosity of liquid phase
V_N	Water jet velocity at the nozzle exit
V_J	Water jet velocity at impingement point
D_J	Jet diameter at impingement point
D^*	Effective diameter of film gas entrainment
Q_a	Air entrainment rate
V_a	Air velocity in air inflow region at the impingement point
h_3, h_2, h_1	Representative global grid sizes
ΔV_i^E	Volume occupied by an element in a grid
p_u	Apparent order of solver method
$\mathrm{e}_{\mathrm{a}}^{21}$	Approximate relative error
$\mathrm{e}_{\mathrm{ext}}^{21}$	Extrapolated relative error
$\mathrm{GCI}_{\mathrm{fine}}^{21}$	Fine grid convergence index

$\emptyset_1, \emptyset_2, \emptyset_3$	Variables for estimation of discretization error

ABBREVIATIONS

CPLJ	Confined plunging liquid jet
PIV	Particle image velocimetry
CFD	Computational fluid dynamics
rms	Root mean square
LPM	Litre per minute

1 Introduction

1.1 Motivation

A liquid jet plunging in a pool of liquid entrains gas at the gas-liquid interface. Entrained gas is dispersed in liquid pool in form of bubbles. This simple phenomenon of gas entrainment is widely observed in nature and bears great industrial significance. For example oceans absorb atmospheric gases including human generated CO_2 emissions by plunging breaking water waves (Chanson et al., 2006). The same mechanism of air entrainment is responsible for formation of long bubbly wakes behind naval ships by breaking bow waves. This bubbly flow alters flow hydrodynamics around the ship and produces unintended acoustic and optical signatures (Moraga et al., 2008). Extensive research on plunging jets is also driven by an important application in nuclear industry. During loss of a coolant accident (LOCA) in a nuclear power plant, Emergency Core Cooling (ECC) is activated. In the process of ECC a cold water jet is injected in a cold leg partially filled with hot water and steam. Plunging cold water jet entrains steam which subsequently affects cold and hot water mixing. It is important to understand the cold and hot water mixing because this mixed water is used to cool reactor pressure vessel. Undesirably cold water may result in high thermal loads at reactor pressure vessel wall and affect its integrity (Schmidtke et al., 2009).

Plunging liquid jets have also been demonstrated as an efficient gas liquid contacting device (Atkinson et al., 2003). Plunging jet based systems are in use as chemical or biological reactors. Bin (1993), in his review article demonstrated that plunging liquid jet based downflow bubble columns have higher gas transfer efficiency than conventional bubble columns and stirred tanks. Due to this favourable property plunging jet based downflow bubble columns have been used in the areas of mineral flotation, wastewater treatment and other chemical industries. Jameson Cell is a widely used flotation unit based on this concept (Tasdemir et al., 2007).

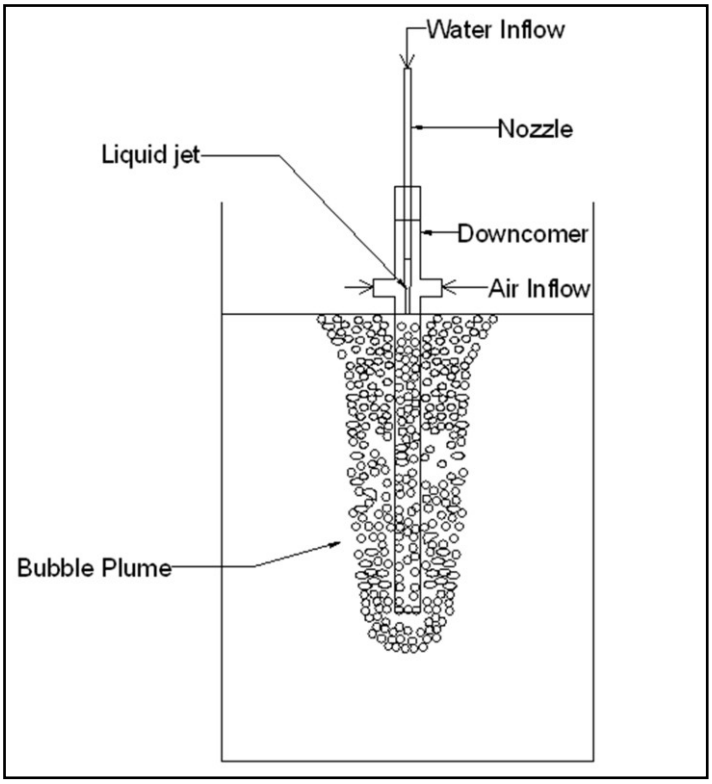

Figure 1-1 Confined Plunging Liquid Jet System

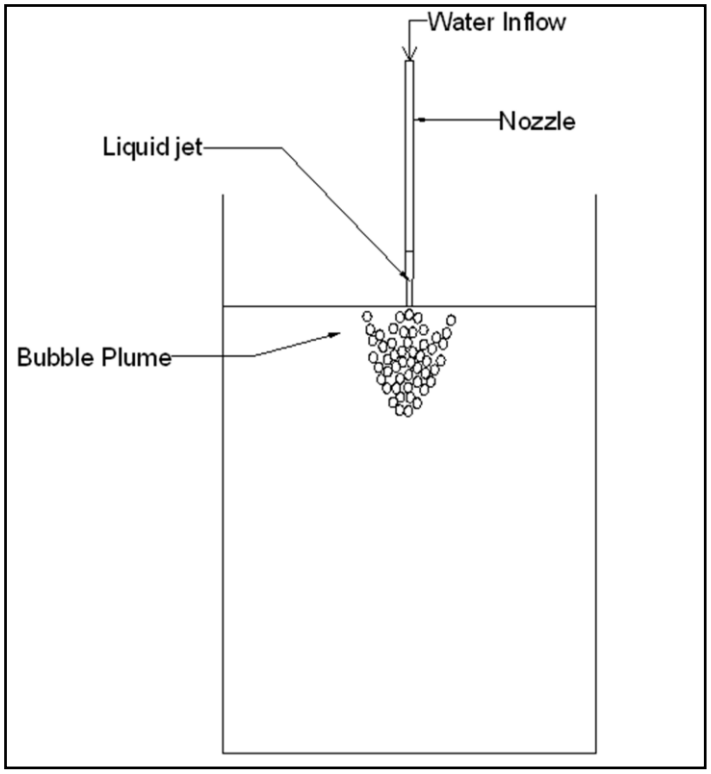

Figure 1-2 Plunging Liquid Jet System

Application of a confined plunging liquid jet system (CPLJ) in waste water treatment and lake destratification is the area of investigation for present work. In a CPLJ system, as shown in figure 1-1, jet is allowed to fall in a narrow space of liquid. This leads to an increase in penetration depth of bubbles over conventional plunging jet systems, figure 1-2. Before proceeding to further discussion, it is important to understand the process of lake destratification.

1.1.1 Lake Destratification

During summers, lakes are often thermally stratified in three layers, warm upper layer (Epilimnion), thin middle layer (Metalimnion) and bottom cold layer (Hypolimnion), see figure 1-3. Warm upper Epilimnion layer is rich in nutrients and receives sufficient amount of sun light in summer to promote algal growth. Moreover, as the wind blows during summers water in Epilimnion layer is mixed well, which ensures that oxygen rich water from surface is transported throughout the Epilimnion layer. However, wind head is often not enough to move the cold water in Hypolimnion, which leads to negligible supply of oxygen to this layer. Over summer, limited amount of the oxygen contained in the Hypolimnion layer is gradually consumed by aerobic bacteria and other living animals.

Most of the nutrients are contained in the lake bottom (Hypolimnion), so lack of mixing in whole lake also means that nutrients can not be supplied to Epilimnion. Hence, Epilimnion has limited amount of nutrients at the beginning of summer, which are consumed over summer to promote algal boom. As the nutrients in Epilimnion dwindle, large destruction of algae may occur, which settles as organic matter at the bottom. Since most of the oxygen in Hypolimnion has already been consumed, this extra organic matter may lead the lake to anoxic condition, where anaerobic bacteria may start to decompose the organic matter leading to generation of harmful gases such as H_2S (Hydrogen Sulfide) and NH_3 (Ammonia). Lack of oxygen and presence of harmful gases may lead to destruction of aquatic life and in fact whole ecosystem in lower part of lake may be affected.

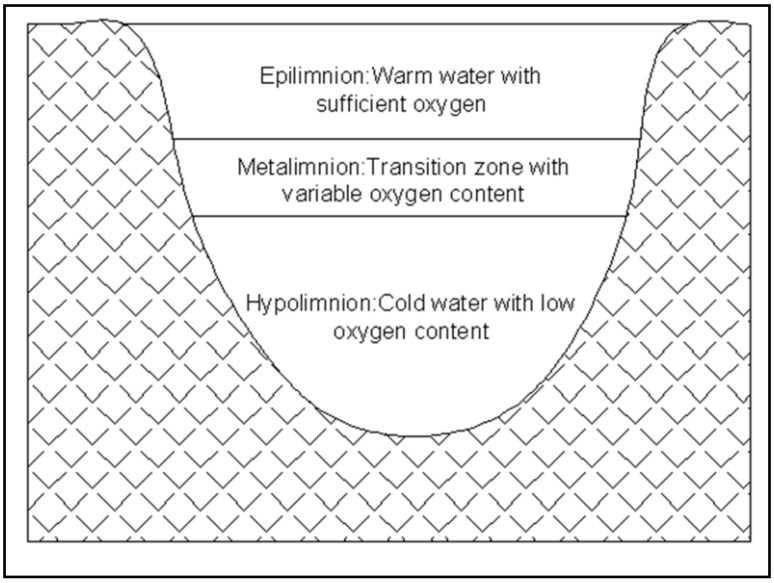

Figure 1-3 Stratification in a lake

In such cases an artificial destratification of lake is often recommended. Commonly, mechanical pumping technique or bubble curtains are applied. Recently, bubble curtains have emerged as a favourable technology. In bubble curtain technique, compressed air is injected in to the lake bottom through an air diffuser. Rising air bubbles entrain the water and lift it to the lake surface, resulting in large scale water circulation which not only breaks stratification but also performs aeration. However, this technology is cost prohibitive due to high initial investments and operating costs. Michele and Michele (2002) proposed a free jet submerged in lake for promoting artificial destratification. This liquid jet can transfer the oxygen enriched water from surface of the lake to the Hypolimnion. It is believed to be energetically more attractive than bubble curtains as it involves pumping of water which is mechanically more efficient than air-compression process. However, using free jet for destratification will require considerable operation time as aeration is dependent on recirculation of natural oxygen rich surface water, which is a slow process. A CPLJ system combines the strength of both these systems and offers a better prospect. It can not only provide aeration and destratification of the lake by dispersing the entrained air in the Hypolimnion Layer (same as bubble curtains) but also transfer the oxygen enriched warm water from surface of the lake to the cold Hypolimnion (same as free liquid jet), leading to considerably faster

destratification than bubble curtains or the free liquid jet. Similar requirements also exist in waste water treatment plants, where waste water containing a large amount of organic matter is needed to be aerated for removal of the organic content by oxidation process.

Apart from the above mentioned advantages, CPLJ based systems offer other benefits too. It has already been demonstrated to be more efficient for waste water aeration than conventional bubble columns and stirring devices (Bin, 1993). A CPLJ system does not require any compressor or stirring devices, leads to a closed loop hydraulic system, which is easier to operate and maintain. Since bubbles move against their buoyancy, in these systems gas residence time is considerably higher than conventional systems.

1.2 Thesis Objectives

A single CPLJ system is a base unit for the above mentioned applications. Successful design of a CPLJ based lake destratification or waste water treatment system will not be possible without detailed understanding and ability to predict the oxygen mass transfer and hydrodynamic behaviour of the flow. Present work serves as a first step towards these goals. In this study, our objective is experimental and numerical characterization of a confined plunging liquid jet system, as shown in figure 1-1. Focus of numerical analysis has been turbulent, Euler-Euler two-fluid multiphase flow simulation of bubble plume dispersion.

There is a systematic lack of quantitative data on plume extents (width and depth). Bubble plume size in a CPLJ system is expected to be affected by nozzle diameter (D_N), jet length (H_N) and water flow rate. Therefore, on experimental front, our objective has been quantification of effect of these parameters on bubble plume profiles and water flow field, through High Speed Camera Photography and Particle Image Velocimetry (PIV). For more clarity, key objectives are listed below:

- Development of a confined plunging liquid jet setup for conducting PIV and high speed camera experiments
- Experimental assessment of effect of change in inlet water flow rate, jet height and nozzle diameter on water flow field around bubble plume through PIV technique
- Development of image processing programs in MATLAB for segmentation of bubble plume boundaries in high speed camera photographs
- Experimental analyses of effect of change in inlet water flow rate, jet height and nozzle diameter on bubble plume width and depth, through high speed camera photography and digital image processing.
- CFD simulation of bubble plume dispersion for the test case of 7 mm nozzle diameter, 100 mm jet length and 12.5 LPM water flow rate

1.3 Physical Model

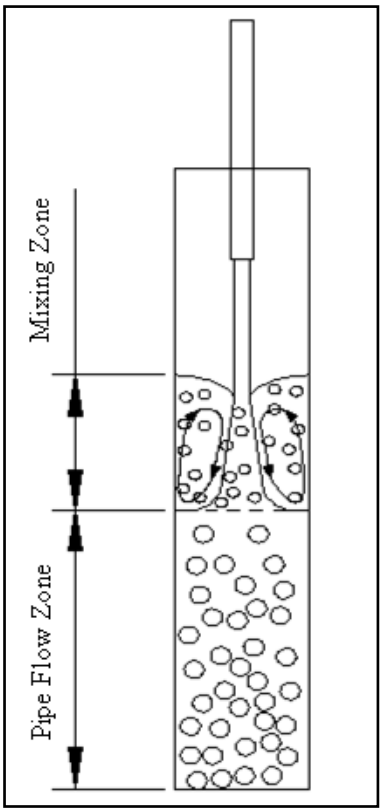

Figure 1-4 Schematics of air entrainment in a downcomer

Exact physical mechanism of air entrainment by a plunging jet is still unclear. Yet, it is known that the phenomenon of air entrainment involves wide range of length scales varying from jet surface instabilities (few hundred micrometers in our case) to system length scale (around 0.5 m for our case). Time resolution can be as low as few hundred microseconds for resolving air entrainment phenomenon at the air-water interface.

As the jet impinges in water, very small bubbles are generated and a distinct biphasic conical zone is formed which expands to meet downcomer pipe walls (Evans and Machniewski, 1999), figure 1-4. This conical zone from point of impingement to the position where it meets pipe walls is known as mixing zone. After mixing zone, a uniform air-water two phase flow (also known as uniform pipe flow) is established where bubbles move downward under water velocity and escape from the downcomer into outer pool. Figure 1-5, a high speed camera photograph at the impingement point obtained during experiments substantiates above thesis. Here, a biphasic conical zone and commencement of uniform pipe flow can be clearly observed. Around biphasic conical zone some large bubbles tend to rise to surface and a re-circulatory pattern, as shown in figure 1-4 is generated.

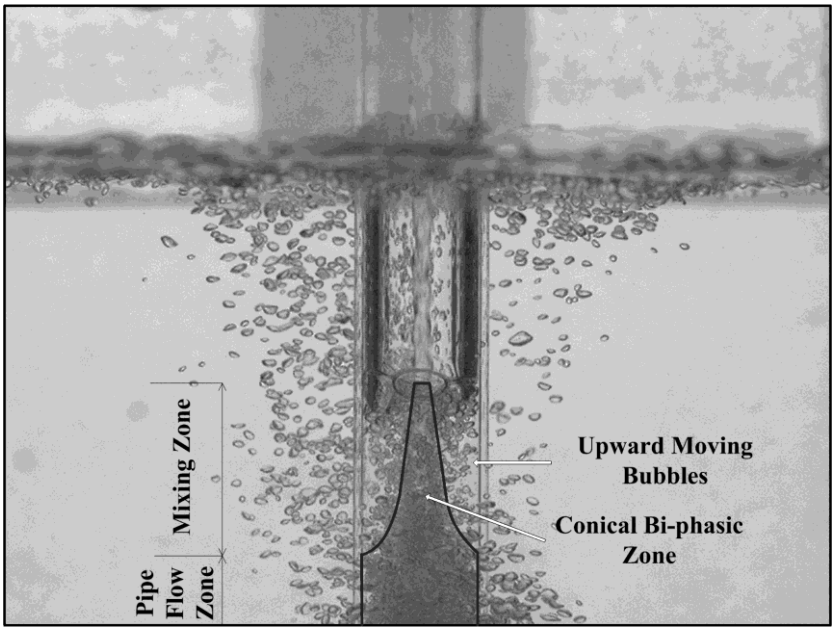

Figure 1-5 High speed camera photograph at plunging point

1.4 Literature Review

Mechanism of air entrainment by a liquid jet plunging in a liquid pool has been investigated by many authors. However, there is no conclusive information available about the mechanics of air entrainment at the impact point. Despite this, previous studies have successfully identified key parameters involved in the process of air entrainment. Early publications in this area showed that air entrainment occurs when liquid velocity exceeds a minimum critical velocity value (Ervine and Elsawy, 1975, Cummings and Chanson, 1999 and Danciu et al., 2009). For a given liquid-gas interface, apart from physical properties of the gas and liquid, air entrainment rate is mainly controlled by jet surface turbulence, nozzle geometry, jet length and liquid flow rate (Van de Sande and Smith, 1976, Lin and Donnelly, 1966). Oguz (1998) showed that maximum bubble size is correlated to jet surface disturbance. He found maximum bubble size to be 1/4 of the jet surface disturbances. Bin (1993) published a comprehensive review on plunging jets detailing various mechanisms of air entrainment and empirical correlations of bubble size, plume penetration depth, and air entrainment rate. Ohkawa et al. (1986) proposed that if a liquid jet is allowed to plunge in a confined space, e.g. a tube of 4-6 times diameter of nozzle, then sufficient liquid flow velocity can be obtained in downward direction in the tube to overcome buoyancy forces on the bubbles and bubble penetration depth can be increased. Subsequently various studies probing the confined plunging liquid jet bubble columns have been published, where pressurized gas is externally supplied to the downcomer through an air inlet and liquid to gas flow rate is independently controlled (Atkinson et al., 2003 and Majumder et al., 2005). Contrary to the setup used in those studies, in present study and in the work of Ohkawa et al. (1986) gas is entrained naturally by a plunging jet and no external gas compressor is needed. Ohkawa et al. (1986) also demonstrated that for same nozzle liquid velocity (V_N), diameter of nozzle (D_N) and free jet length (distance from the nozzle to free surface of liquid, H_N) gas entrainment rate is higher in a CPLJ system than in an ordinary plunging liquid jet system.

Deswal (2007) obtained volumetric oxygen transfer coefficient by conducting aeration studies on a deoxygenated water pool. He showed plunging liquid jet system to have higher oxygen transfer efficiency (kg O_2/kWh) than turbine agitators and small and large bubble size dispersers (bubble curtains). Recently, Botton and Cosserat et al. (2009) published oxygen mass transfer studies on a gas-liquid contacting system similar in spirit to that of Ohkawa et al. (1986). They found plunging jet aerator to provide higher volumetric gas-liquid mass transfer coefficient for same input power per unit volume of liquid than conventional gas-liquid stirred tanks and bubble columns.

Contrary to numerous studies reported on experimental analysis of a plunging jet system, there have been very few numerical studies. It is only recently that developments in Computational Multiphase Flow have started to achieve a level that such complex turbulent multiphase flow problems can be investigated. Readers are referred to studies investigating CFD simulation of air-water flow in bubble columns (Akhtar et al., 2006, Becker et al., 1994, Becker et al., 1999, Rampure et al., 2007, Ranade and Tayalia, 2001, Sokolichin and Eigenberger, 1994 and Ali et al., 2008). Sanyal et al. (1999) presented a comprehensive study on simulation of bubble column reactors using CFD software Fluent. Bravo et al. (2007) discussed potential of commercially available CFD codes for simulation of bubble plumes. Chen et al. (2005) discussed application of population balance modelling in three dimensional simulation of a bubble column.

Ma et al. (2010) developed a sub-grid air entrainment model for prediction of the rate of air entrainment. They implemented this sub-grid air entrainment model as a source term in bubble population balance equation in a RANS type two-fluid Euler-Euler CFD code. They obtained close agreements with corresponding experimental results of time and circumferentially-averaged void fraction distributions reported by Chanson et al. (2002) and Chanson et al. (2004). Schmidtke et al. (2009) tested impact of various drag models on air void fraction and discussed various approaches for modelling air entrainment by a plunging jet. Krepper et al. (2011) also performed two-fluid Euler-Euler

simulation of liquid flow field generated by a plunging water jet and assessed its impact on fibre transport in a sump.

1.5 Contribution to the Knowledge

- First known experimental study of water flow field around bubble plume in a CPLJ system through PIV technique
- First known quantitative study of impact of change in inlet water flow rate, H_N and D_N on bubble plume extents using high speed camera photography and digital image processing.
- Contribution of image processing algorithms for bubble plume boundary detection in high speed camera images
- Numerical simulation of bubble plume dispersion in a confined plunging liquid jet system using commercial CFD software ANSYS CFX 12.1.

1.6 Summary of the Thesis

Thesis has been broadly divided in Experimental and Numerical work. In Chapter 2, detailed information about factors involved in design of the experimental set up and test matrices has been provided. In Chapter 3, PIV flow field measurements around bubble plumes have been presented. High speed camera observations and digital image processing algorithm for segmentation of plume boundaries have been discussed in Chapter 4. It presents time averaged bubble plume profiles for different test cases. Methodology of CFD simulation and reconciliation of CFD results with high speed camera observations and PIV experiments have been discussed in Chapter 5. Finally, Chapter 6 presents recommendations for future work.

2 Experimental Setup and Test Matrix

2.1 Introduction

Experimental setup prepared during present work is shown in Figure 2-1. Three main objectives were established for setup design, 1) ability to vary distance from nozzle exit to free surface of water (H_N), 2) facility to allow use of nozzles of variable diameter and 3) ability to vary water flow rate and hence nozzle water velocity (V_N).

Figure 2-1 Experimental Setup

The setup consists of a transparent acrylic rectangular water tank, as shown in Figure 2-2. Based on the work done by previous investigators (Danciu et al., 2009, Schmidtke et al., 2009 and Krepper et al., 2011), tank length, breadth and height are decided to be 520 mm, 520 mm and 760 mm. It was prepared by 10 mm thick transparent acrylic sheets, glued together by TENSOL 12 acrylic cement.

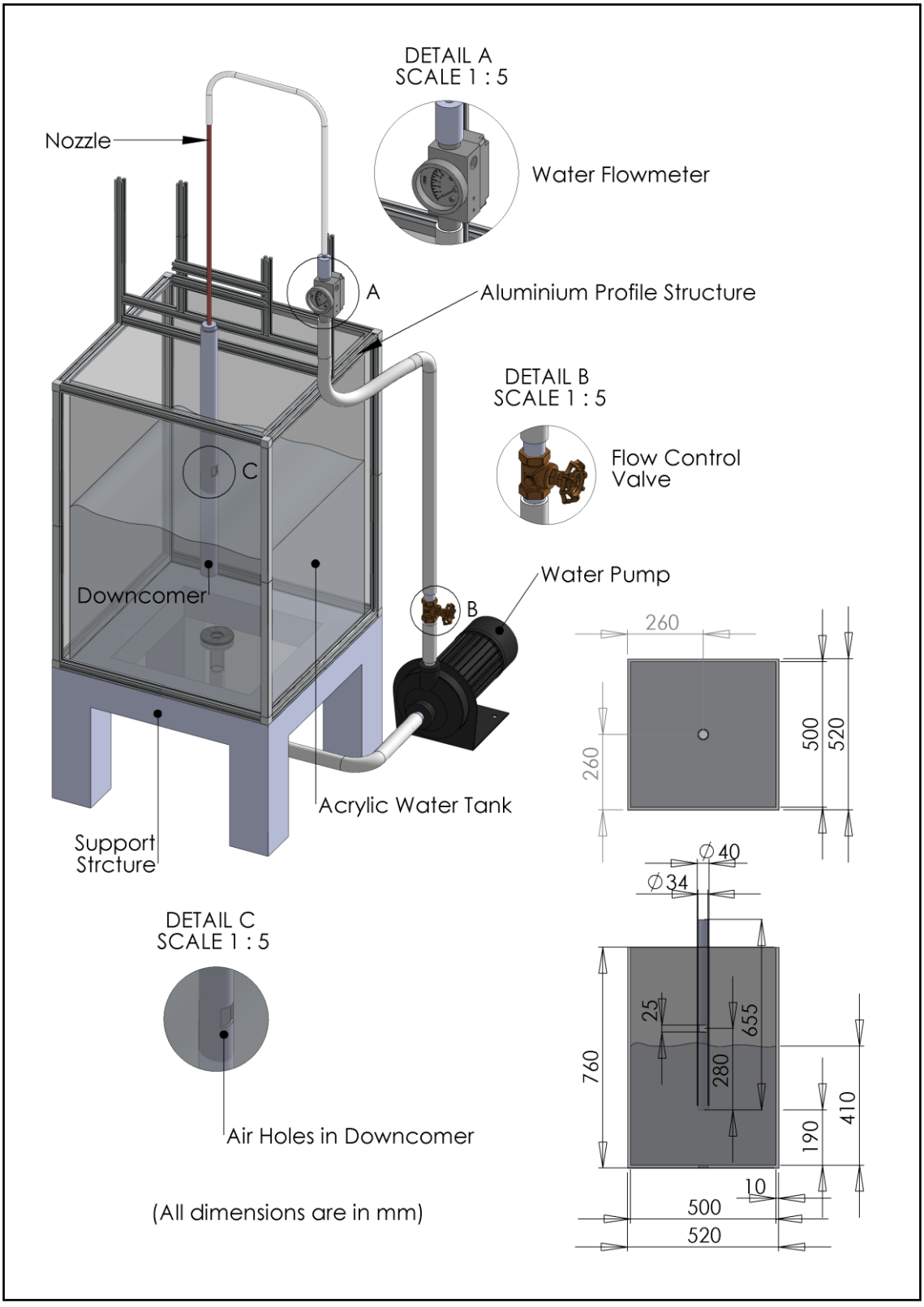

Figure 2-2 Detailed CAD Drawing of Setup

Inner dimensions of the tank were, length = 500 mm, breadth = 500 mm and height = 750 mm. An exit nozzle of 25.4 mm was provided at the bottom of the tank. The exit nozzle was connected to inlet port of 0.37 kW, stainless steel centrifugal water pump. Outlet of the pump was connected to a Globe Control Valve, which facilitated variation of water flow rate. The control valve was connected to an acrylic inlet nozzle through a Turbine Flow Meter made available by Cross Instrumentation, USA. Least count of flow meter was 0.01 LPM. Nozzle length to diameter ratio is maintained above 40 for all test cases to ensure that flow is fully developed at the nozzle exit. Nozzle is connected to the downcomer through a rubber cork.

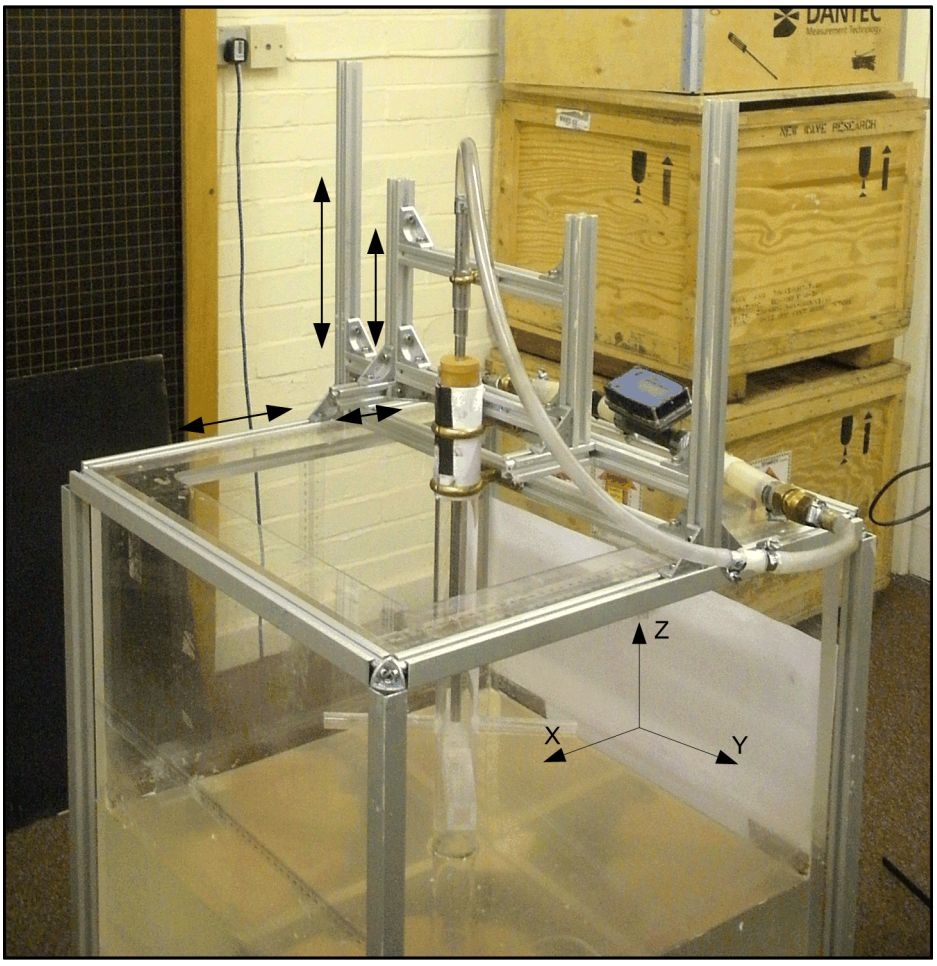

Figure 2-3 Aluminium structure on the water tank

The downcomer and nozzle are clamped on an aluminium profile structure provided at the top of the water tank, as shown in Figure 2-3. Components of

profile structure can be manipulated to locate downcomer at any position in XY and YZ plane. In a similar manner nozzle can also be moved in Z direction to achieve any height, H_N from free surface of the water. In this work, nozzle and downcomer were centralized at centre of the rectangular tank, so that distance from sidewalls of the tank to centreline of the downcomer and the nozzle is 260 mm, as shown in Figure 2-2. Water level was maintained at a height of 410 mm from bottom surface of the tank and downcomer was inserted 220 mm below the water level. Water tank with aluminium structures is kept on a support structure. Whole assembly is located in two big sumps to accommodate water leakage in case of a tank breakage or failure.

The downcomer is a cylindrical acrylic tube of 40 mm outer diameter, 34 mm inner diameter with a height of 655 mm. Two square recesses of 20 mm×20 mm, opposite to each other are provided in it at a height of 280 mm from the bottom of the downcomer. During air entrainment process air flows inside the downcomer through these two slots.

2.2 Test Matrix

Test matrices have been constructed to observe impact of change in inlet water flow rate, nozzle height from the free water surface (H_N) and variation in nozzle diameter (D_N) on flow hydrodynamics and bubble plume extents. Two circular nozzles of 7 mm and 10 mm diameters have been used during experiments. Test matrices are being shown below in the form of Tables 2-1 and 2-2. For each nozzle, H_N is varied from 100 mm to 250 mm in steps of 50 mm. For each $H_{N,}$ water flow rate is varied from 7.5 LPM to 15.0 LPM in steps of 2.5 LPM.

Table 2-1 Test Matrix 1

Downcomer Diameter = 34 mm ID				
Nozzle Diameter = 7 mm ID				
Jet Length (mm)	**Water Flow Rate (LPM)**			
100	7.5	10.0	12.5	15.0
150	7.5	10.0	12.5	15.0
200	7.5	10.0	12.5	15.0

250	7.5	10.0	12.5	15.0

Table 2-2 Test Matrix 2

Downcomer Diameter = 34 mm ID				
Nozzle Diameter = 10 mm ID				
Jet Length (mm)	**Water Flow Rate (LPM)**			
100	7.5	10.0	12.5	15.0
150	7.5	10.0	12.5	15.0
200	7.5	10.0	12.5	15.0
250	7.5	10.0	12.5	15.0

3 Flow Field around Bubble Plume: PIV Experiments

3.1 Introduction

Particle Image Velocimetry (PIV) is a whole-field flow measurement technique, which is widely used for velocity field estimation in single-phase flows. In this technique, flow is seeded with tracer particles and a laser light sheet is allowed to fall on the tracer particles in plane of investigation. Tracer particles scatter the incident laser light. An image of the illuminated particles is captured by a digital camera placed perpendicular to the light sheet. Two successive images are taken at a very short time interval. Each image is divided in to a number of interrogation windows. For each interrogation window a displacement vector is evaluated using statistical techniques such as Auto-correlation or Cross-correlation. A detailed review on PIV can be found in Raffel et al. (2007).

Application of PIV in air-water two-phase flow requires phase discrimination. Sridhar et al. (1991), Bröder and Sommerfeld (2002), and Lindken and Merzkirch (2002) published manuscripts detailing a combined Particle Image Velocimetry and Laser Induced Fluorescence (LIF) technique which is also known as PIV/LIF. This technique allows separation of velocity information of air and water phases. A detailed description of the PIV/LIF method which has been utilized in present study can be found below.

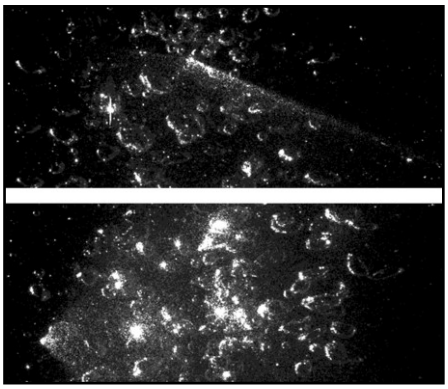

Figure 3-1 Laser flares generated by bubbles

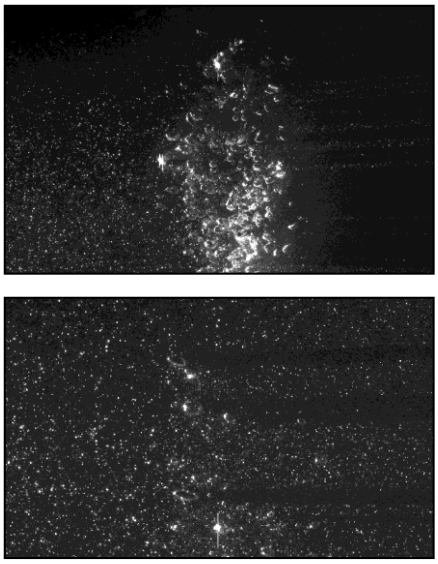

Figure 3-2 Shadows behind bubbles due to light sheet refraction and reflection at bubble surfaces

3.2 PIV/LIF Technique

Conventionally for liquid velocity measurement sliver coated hollow glass spheres or Polystyrene spheres are used. These tracer particles scatter light at the wavelength of the incident laser. In a dispersed air-water flow, flow space is marked by abrupt changes in optical properties at bubble-water interfaces. During PIV investigation, the laser light sheet is strongly refracted and reflected at the bubble surfaces. It results in laser flares in recordings (see figure 3-1), and decrease in light sheet intensity behind the air bubbles (as shown in figure 3-2). Moreover, laser light reflected by bubbles can directly fall on camera CCD sensor and damage it. A PIV/LIF system avoids these difficulties by using fluorescent dye coated tracer particles, and a corresponding optical high pass filter in front of the camera. For example, in present work 20-50 μm Rhodamine B coated PMMA (Polymethyl methacrylate) particles have been used. For these tracer particles, maximum absorption occurs at an incident wavelength of 540 nm which is close to 532 nm wavelength of the laser light used in the current study (LaVision GmbH, 2006). Hence, tracer particles efficiently absorb laser light and emit photons at a wavelength greater than 532 nm with a fluorescence maximum at 625 nm. The recording Camera is equipped with a fluorescence

edge filter designed for Rhodamine B dye. It cuts off wavelengths lower than 540 nm and provides more than 80% transmission efficiency for light in the LIF emission range, as shown in figure 3-3 (LaVision GmbH, 2009). Contrary to particles, bubbles scatter light at the laser wavelength which is cut off by the edge filter. Hence, present PIV/LIF system separates signals from air phase and contains data for only water velocity measurement.

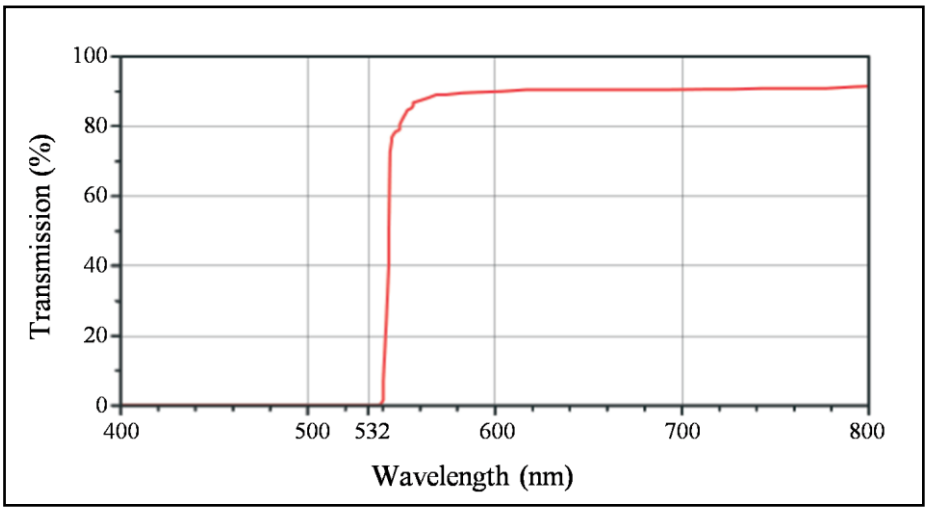

Figure 3-3 Transmission-Wavelength graph of Fluorescence Edge Filter (Source: LaVision GmbH, 2009)

3.3 PIV System

Experimental setup, as shown in figure 3-4, employed a 532 nm Nd:YAG laser. Light beam from laser box was converted into a 1-1.5 mm thick light sheet by a spherical and cylindrical lens combination. Particle images were recorded by a Kodak Mega Plus ES1.0 camera having 1016×1008 pixel resolution. Camera CCD sensor was 9.16 mm wide and 9.07 mm high. Physical pixel size was 9 µm. A 50 mm (focal length) Nikkor lens was used as the camera optics. Image acquisition and laser control was done through the FlowManager software, provided by Dantec Dynamics. Laser light sheet was carefully adjusted perpendicular to the east wall of the water tank by ensuring the same distance of 260 mm on east and west walls from the south wall of the tank. It also ensured that light sheet is centralized. Flow was incessantly seeded until 6-9

particles were observed in most of the interrogation windows, figure 3-5. In order to maintain a mean particle separation greater than 0.1 pixel and less than a quarter of interrogation window size, pulse separation time between two recordings was varied between 14-30 ms for different test cases (LaVision GmbH, 2002). For Test Matrix 1, irrespective of H_N, a time difference of 14 ms was used for the flow rate of 10.0, 12.5 and 15.0 LPM and 20 ms for the flow rate of 7.5 LPM. For Test Matrix 2, a time difference of 30 ms was used for the flow rate of 7.5 LPM, 25 ms for the flow rate of 10.0 LPM, 20 ms for the flow rate of 12.5 LPM and 15 ms for the flow rate of 15.0 LPM. Since laser light sheet was adjusted in the plane of symmetry, therefore out of plane displacement of particles can be assumed to be negligible. Light sheet is not available beyond bubble plume, therefore only right side of the bubble plume is investigated with an area of investigation of 230 mm×230 mm, as shown in figure 3-4.

3.4 Experimental Procedure

Experiments were performed as per the test matrices provided in the Tables 2-1 and 2-2, in chapter 2. For each test case 840 image pairs were acquired in 12 experimental runs. In each experimental run 70 image pairs were recorded in a continuous mode at an operating frequency of 15 Hz. After completion of a test run, flow was stopped and 5-10 minutes were consumed in preparation of the experimental setup for new test condition. This often resulted in sinking of a considerable number of particles under gravity to the bottom of the tank. Hence, before starting an experiment particles were stirred and adequate time was allowed for flow to achieve natural test conditions before recording was commenced. In most test conditions due to stirring action of re-circulating water, particles remained suspended in water after being stirred.

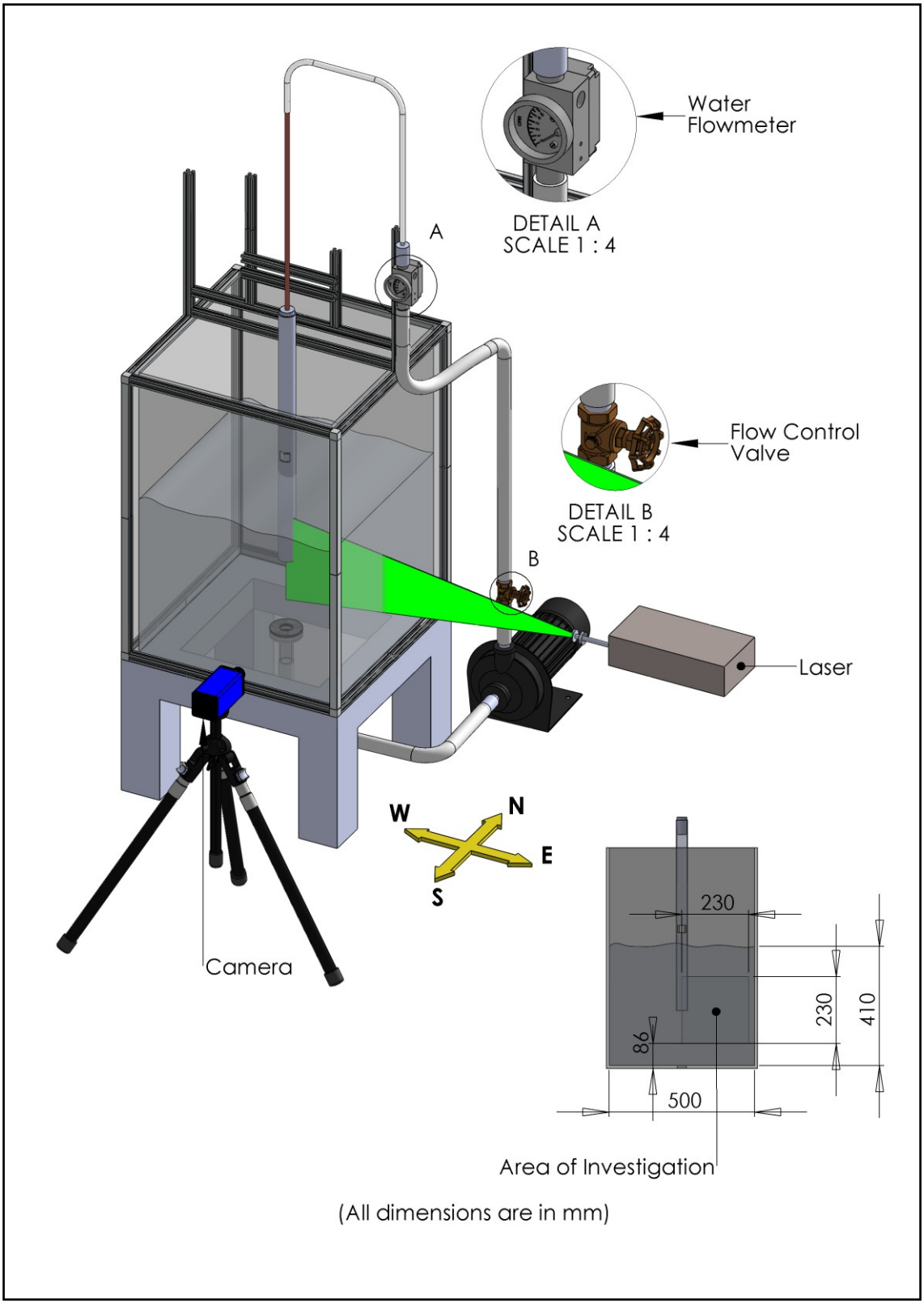

Figure 3-4 PIV Experimental Setup

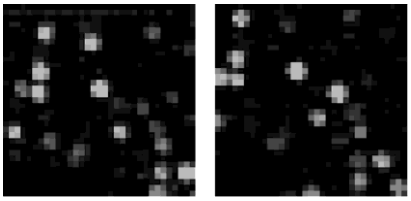

Figure 3-5 Illuminated particles in a typical 32×32 pixel interrogation window pair

3.5 Data Processing

Experimental recordings were converted into IMX format and processed in LaVision DaVis 6.2 Software. Figure 3-6 in left hand side shows a captured PIV recording for the test case of 7 mm nozzle diameter (D_N), 100 mm jet length (H_N) and 12.5 LPM water flow rate. It can be observed that a considerable area in the PIV recording is marked by presence of bubbles. It was important to mask the area occupied by air bubbles before PIV vector processing can be implemented. Therefore, recordings of all the test cases were rigorously analyzed and masks were developed in MATLAB. One such mask for the above mentioned test case is shown in figure 3-6.

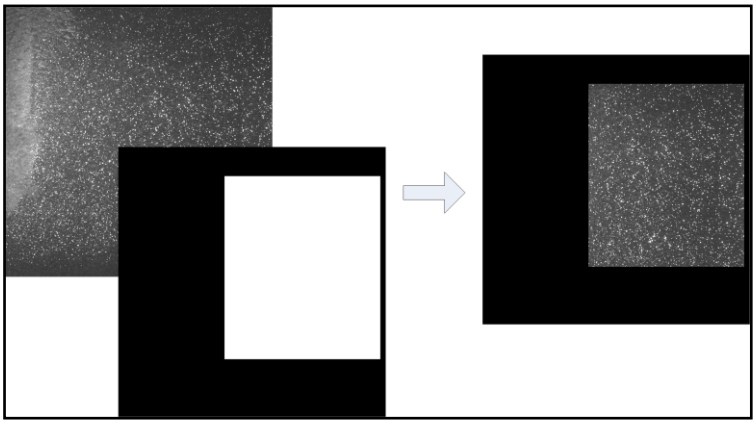

Figure 3-6 A PIV recording for the test case of 7 mm D_N, 100 mm H_N and 12.5 LPM water flow rate and corresponding mask

For PIV vector calculations, at first images were preprocessed by subtracting a sliding background with a scale length of 20 pixels. It filters out large spatial fluctuations in image intensity and generates an image with approximately

constant background level. An adaptive multi-pass algorithm with reducing window size from 64×64 to 32×32 pixels was utilized. For initial window size of 64×64 pixels, 2 iterations were performed. In first iteration, PIV evaluation leads to a reference vector field which is used as a high-confidence window shift for the second iteration. This facilitates higher likelihood of correlating same particles even with smaller window sizes, which in turn improves the signal to noise ratio of correct correlation peak. For final window size of 32×32 pixels, 3 iterations were performed. A 50% window overlap in final pass led to an effective grid spacing of 16 pixels. For vector evaluation, second order, fast standard FFT-Correlation with deformed interrogation windows was used.

In order to achieve sub-pixel accuracy, DaVis uses three-point Gaussian peak fit which requires particle image diameter to be maintained slightly greater than 2 pixels. This criterion was satisfied as most of the particles in captured images were found to be greater than 2 pixels. For adaptive multi-pass, a relative vector range restriction of reference displacement vector±(interrogation window size)/4 and an absolute vector range restriction of reference displacement ±20 pixels was used. In order to remove spurious vectors, results were post processed in each pass and vectors with peak ratio less than 1.3 were removed. Median filter with strongly remove and iteratively replace option was used to remove groups of spurious vectors. For each vector, median filter computes the median of 8 surrounding vectors and keeps the central vector if it lies within the range of median vector±(1.8×root mean square (rms) of neighbor displacement vectors). In second pass it removes those vectors which do not have 3 or more neighboring vectors left from first pass. In third pass all the good vectors are filled which fall in the range of median vector±(2.1×rms of neighbour displacement vectors). Finally, in fourth pass groups with less than 10 vectors are removed.

Vector post processing was also performed with same median filter parameters as described above. In vector post processing, after removal of bad vectors all empty spaces were filled with new vectors by interpolation. It is important to

note that less than 1% vectors were needed to be filled by interpolation in all the cases.

3.6 Uncertainty Analysis

During PIV evaluation outlier and root mean square (rms) errors can be quantified. Outliers were eliminated by the conservative median filter discussed in data processing section. RMS error was quantified by the method proposed by Willert and Gharib (1991), which has been discussed in Ansari et al. (2009). In this method tank was first allowed to settle for 10 minutes. Then particle images were recorded at a very small pulse separation of 2 μs. Such small time difference and still water tank means that physical particle displacement can be confidently assumed to be zero. Hence, displacement values calculated for these recordings show random errors manifested by the evaluation algorithm. Seventy recordings were captured and processed to calculate the typical rms error of 0.08 pixel. For the Test Matrix 1, rms error of 0.08 pixel translates to an rms error of 0.0013 m/s for the flow rates of 15.0 LPM, 12.5 LPM, 10.0 LPM and 0.0009 m/s for the flow rate of 7.5 LPM. For the Test matrix 2, it leads to an rms error of 0.0012 m/s for the flow rate of 15.0 LPM, 0.0009 m/s for the flow rate of 12.5 LPM, 0.0007 m/s for the flow rate of 10.0 LPM and 0.0006 m/s for the flow rate of 7.5 LPM.

Apart from these errors, small random vibrations of experimental setup, spatial error of 1-3 mm in perfectly locating the downcomer at the center of the square tank, small errors in vertical alignment of downcomer and variation in water flow rate of ±0.1 LPM also contributed to overall error in PIV recordings. However, it is difficult to quantify the impact of these errors.

3.7 Results and Discussion

Ensemble Averaged velocity field for the test case of 7 mm D_N, 100 mm H_N and 12.5 LPM water flow rate is shown in figure 3-7. Such ensemble averaged water velocity fields have been compiled for all the test cases, as per the Tables 2-1 and 2-2, in Appendix A.

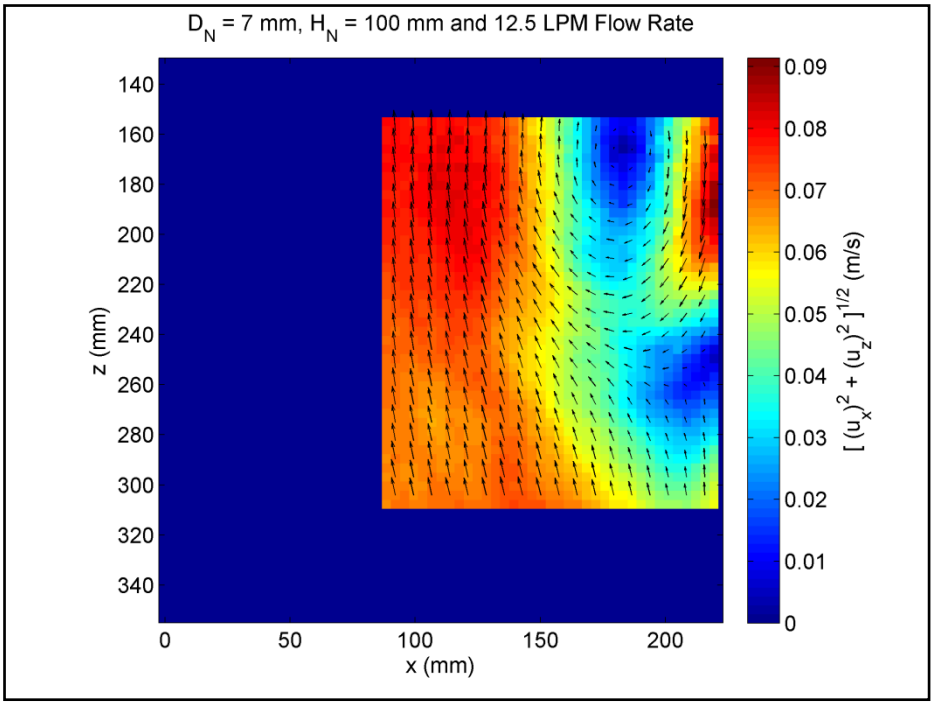

Figure 3-7 Ensemble averaged water velocity field for 7 mm D_N, 100 mm H_N and 12.5 LPM water flow rate

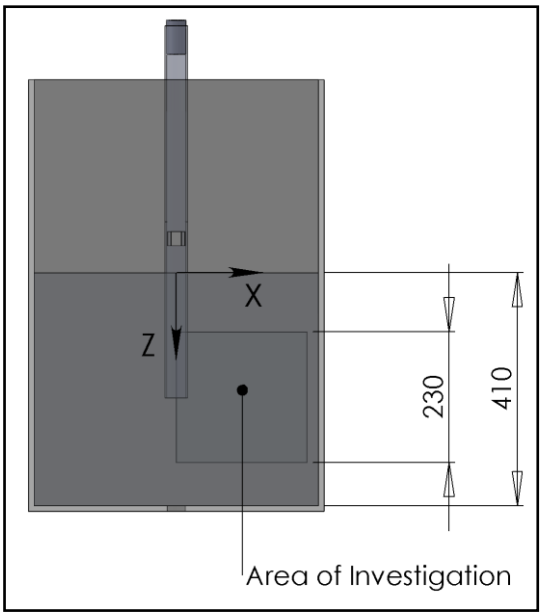

Figure 3-8 Coordinate system

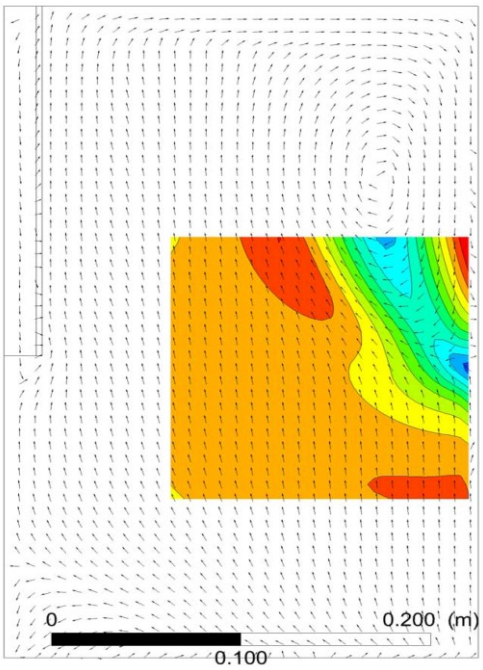

Figure 3-9 Flow field from CFD result

In figure 3-7, x = 0 denotes centerline of the downcomer, while z = 0 is located at the free water surface. Positive Z direction is from free water surface towards the bottom of the tank. Coordinate system is shown in figure 3-8. PIV experiments capture only a partial part of the flow field. So, in order to explain flow field more clearly, this result is being discussed with CFD results from Chapter-5, figure 3-9. From figure 3-7 and 3-9, it can be observed that close to the bubble plume, water is entrained in the plume and lifted upwards. At the free water surface, the air lifted water turns towards the tank wall and returns in downward direction close to the wall. It results in a large scale circulatory feature. A partial part of this circulatory feature has been captured in the PIV area of investigation (as shown in top right), in figure 3-7.

In present work, PIV experiments were conducted with dual objectives of generating data for validation of CFD models, and to investigate the effect of change in water flow rate, H_N and D_N on air-lifted water flow field.

3.7.1 Effect of change in water flow rate

During experiments, water flow rate was increased from 7.5 LPM to 15 LPM in steps of 2.5 LPM, while maintaining same H_N and D_N. Figure 3-10 to 3-13 show the water flow field for 100 mm H_N and 7 mm D_N. It can be observed that with increase in water flow rate, water velocity around bubble plume increases in the upward direction. This phenomenon can be explained by the fact that with rise in water flow rate, bubble plume outside the downcomer tube increases in size. Larger plume means increased air hold-up or presence of more bubbles at any instant of time. Greater amount of air bubbles result in higher buoyancy forces on the surrounding water which leads to increased water velocity in the upward direction. This trend has been observed in all the test cases.

This conclusion is important for application of a CPLJ system in lake destratification. It shows that air lifted water velocity around bubble plume increases with rise in inlet water flow rate. Hence, a CPLJ system operating at a greater water flow rate would lead to faster destratification.

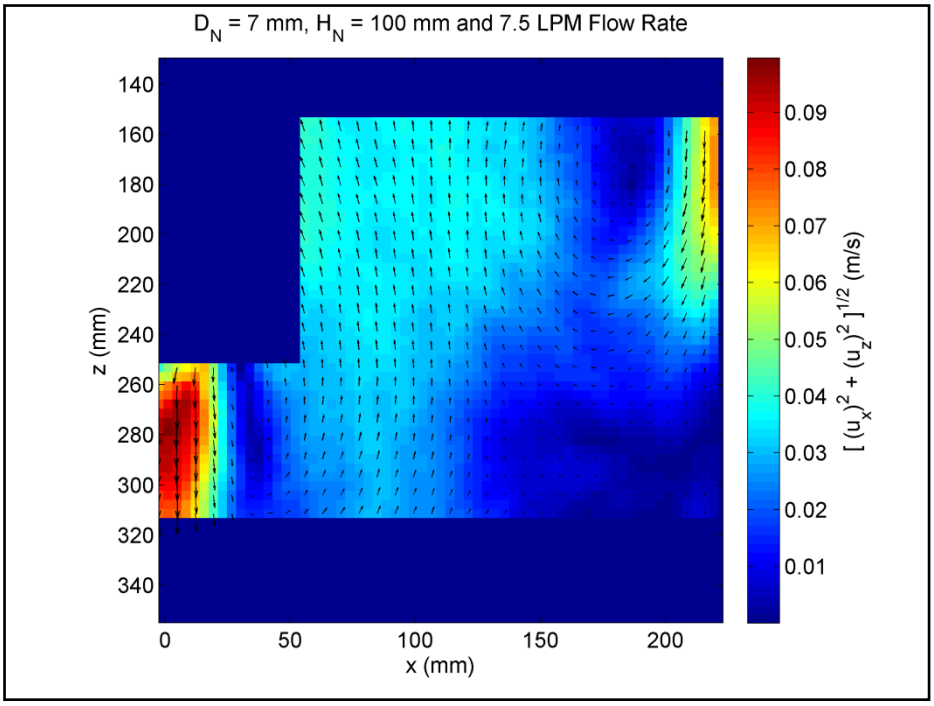

Figure 3-10 Ensemble averaged water velocity field for 7 mm D_N, 100 mm H_N and 7.5 LPM water flow rate

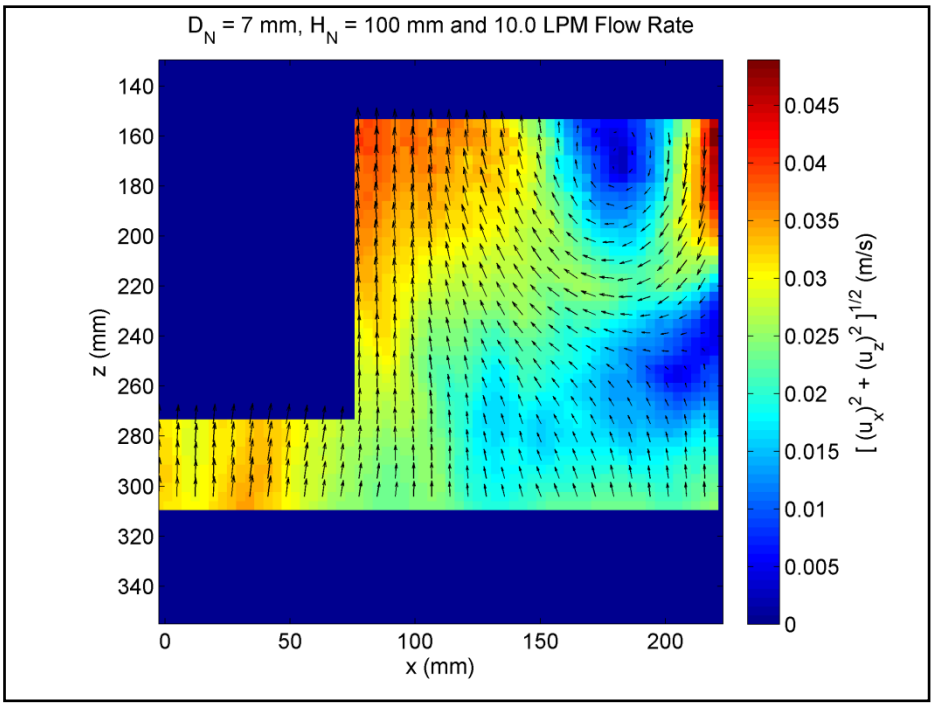

Figure 3-11 Ensemble averaged water velocity field for 7 mm D_N, 100 mm H_N and 10.0 LPM water flow rate

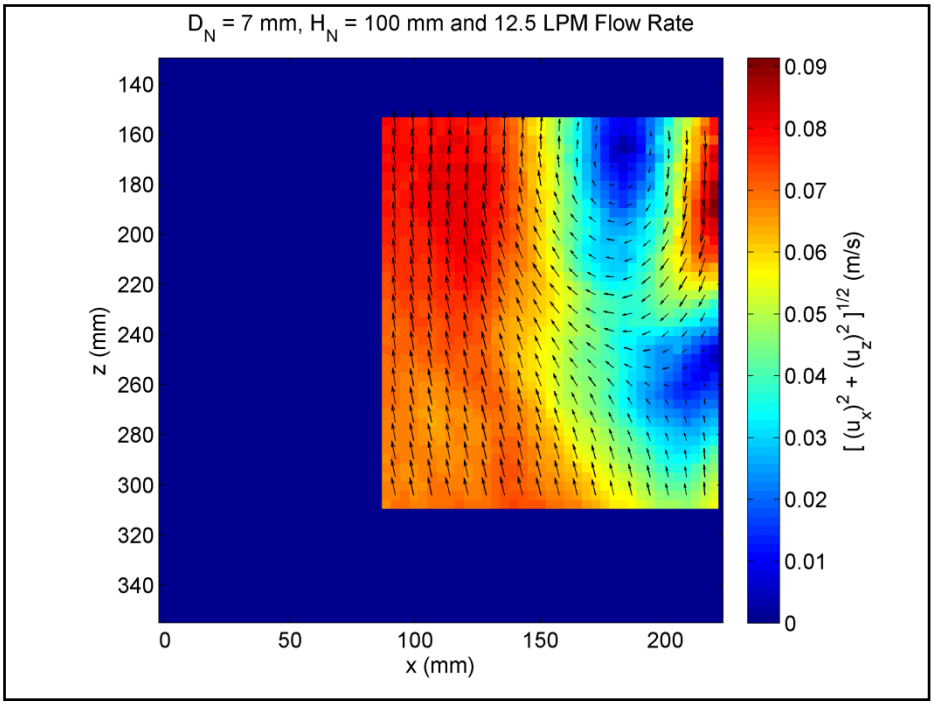

Figure 3-12 Ensemble averaged water velocity field for 7 mm D_N, 100 mm H_N and 12.5 LPM water flow rate

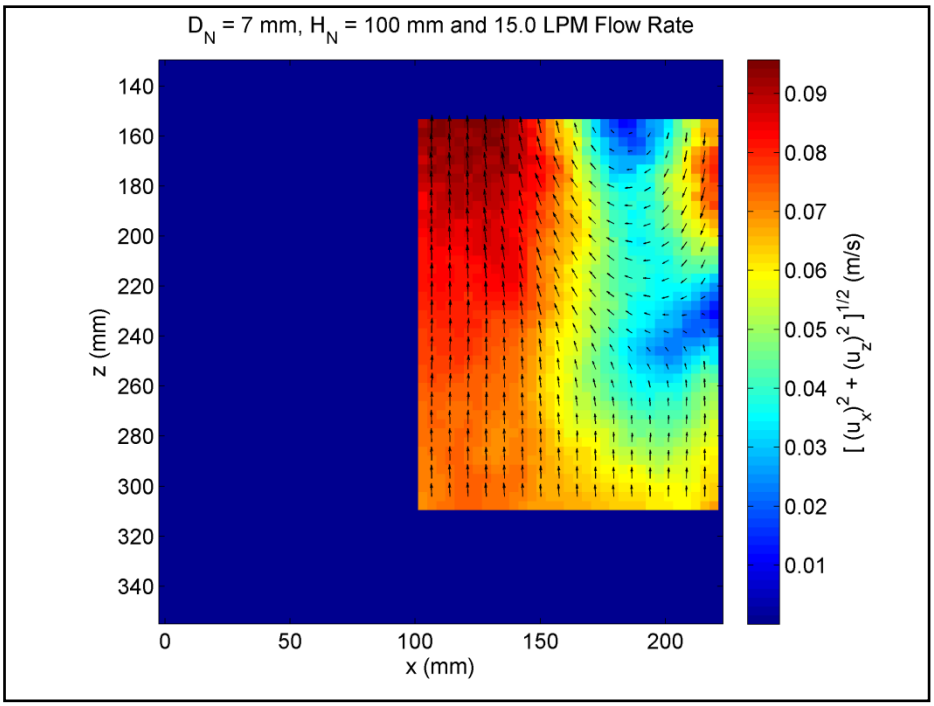

Figure 3-13 Ensemble averaged water velocity field for 7 mm D_N, 100 mm H_N and 15.0 LPM water flow rate

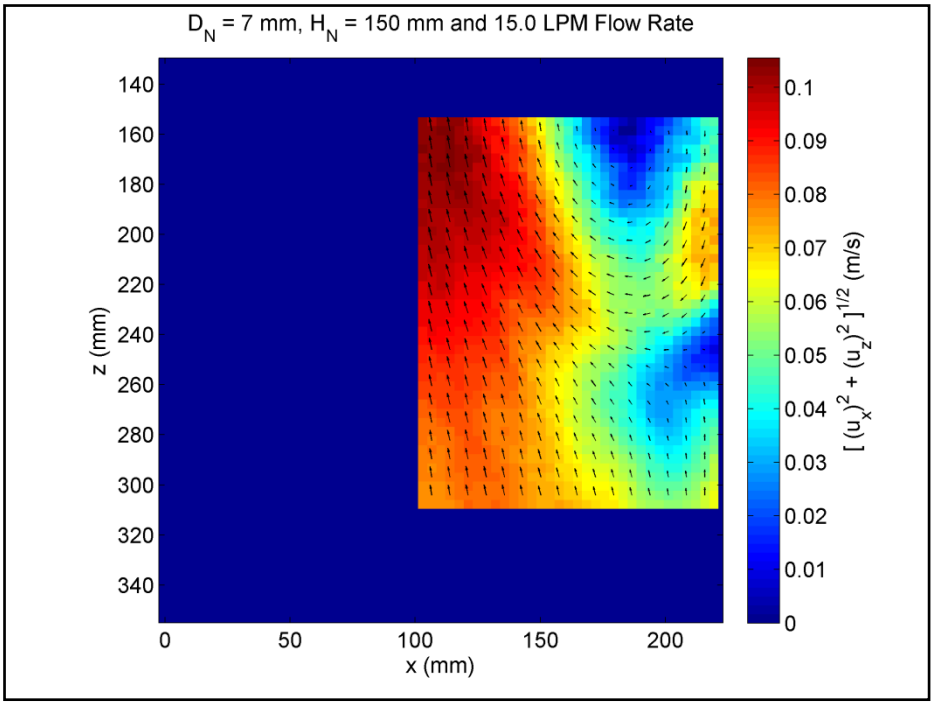

Figure 3-14 Ensemble averaged water velocity field for 7 mm D_N, 150 mm H_N and 15.0 LPM water flow rate

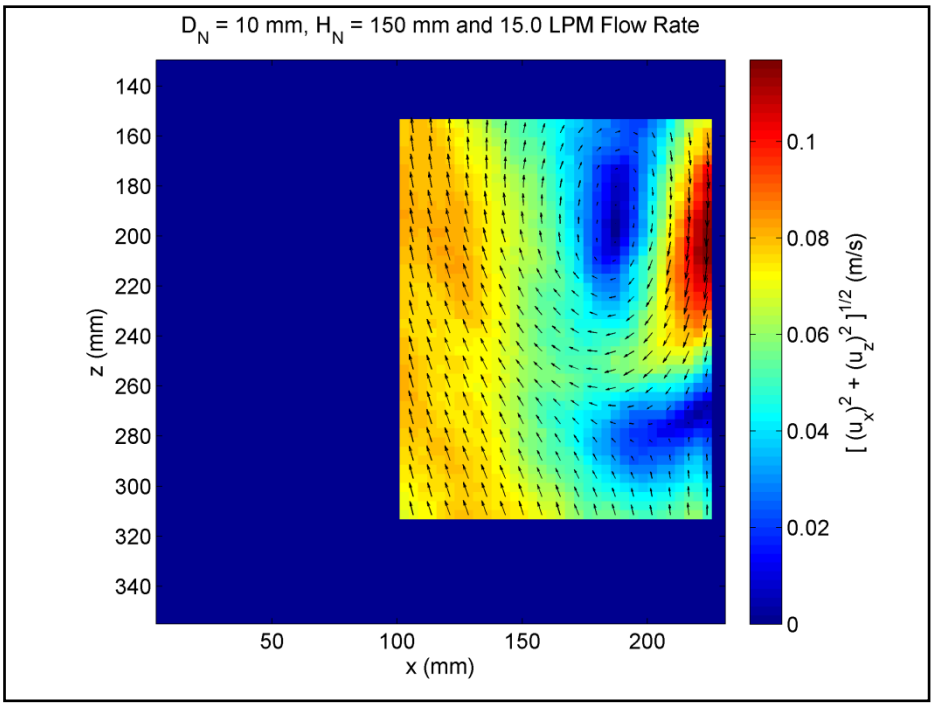

Figure 3-15 Ensemble averaged water velocity field for 10 mm D_N, 150 mm H_N and 15.0 LPM water flow rate

3.7.2 Effect of Change in Jet Length (H_N)

Change in H_N, while maintaining the same water flow rate and D_N was not found to appreciably affect the water flow field around the plume (see Appendix A). It can be explained by the fact that change in H_N does not appreciably affect the bubble plume extents. More discussion about independence of plume size with H_N can be found in section 4.4.2. Water velocity field around a downcomer tube is contributed by the bubble plume. So, if bubble plumes are not affected by H_N then so does the air lifted water flow field.

3.7.3 Effect of Change in Nozzle Diameter (D_N)

With increase in nozzle diameter from 7 mm to 10 mm, bubble plumes were found to significantly decrease in size. It has been discussed in detail in section 4.4.3. Due to the reduction in plume extents, water velocity field around plume is expected to significantly decrease with change in diameter from 7 mm to 10 mm. Figure 3-14 and 3-15 show the water velocity field for both the nozzles at 150 mm H_N and 15.0 LPM water flow rate. Water velocity vectors around bubble plume for 7 mm D_N case are in the range of 0.08 to 0.1 m/s; while for 10 mm D_N case, vectors are in the range of 0.07-0.08 m/s. Hence, as per expectation, water velocity field around the plume are indeed lower in 10 mm diameter jet. Similar trend was observed for other test cases too.

4 Visualization Experiments: Photographic Technique

4.1 Introduction

High Speed Camera observations were conducted to quantitatively analyze the impact of D_N, H_N and water flow rate on bubble plume boundaries in a CPLJ system. High speed camera photographs capturing full scale bubble plume were recorded and processed to obtain a time averaged plume profile for each test case. A Phantom v7.3 colour high speed camera from Vision Research Inc. was placed in front of the acrylic water tank (in a similar manner as that in PIV experiments). The water tank was illuminated from behind by a compatible halogen lamp. A diffuse paper was placed on back wall of the tank which is directly facing the lamp. It diffused incident light from the lamp and provided a uniform background. The Camera was equipped with a 50 mm (focal length) Nikon lens. It was focussed on the same plane of investigation as that in PIV experiments.

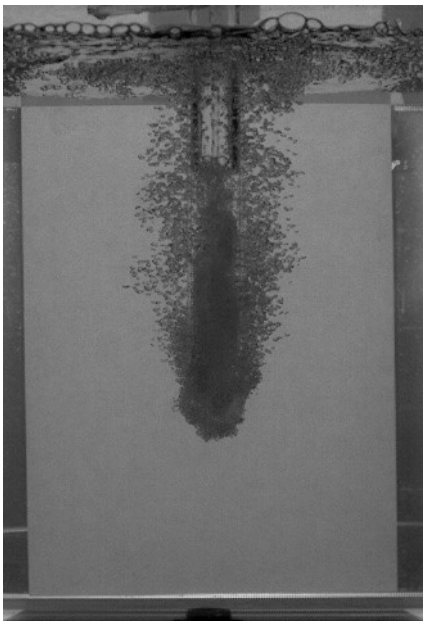

Figure 4-1 A typical bubble plume image

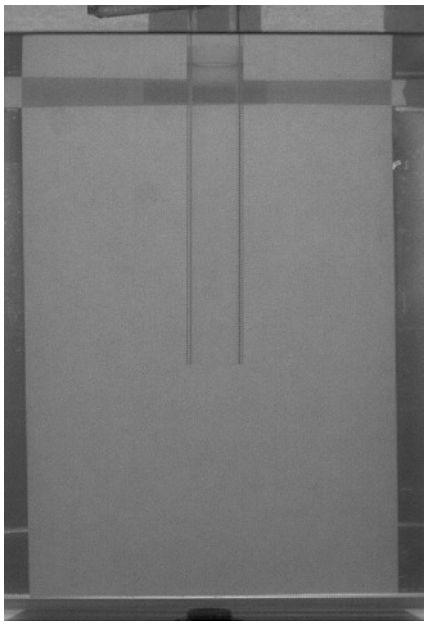

Figure 4-2 Background image

A typical photograph of a bubble plume is shown in figure 4-1. Light emitted from the lamp was refracted and reflected at bubbles surfaces. Therefore,

bubbles appear darker in recordings while background is brighter. It is this difference in intensity levels which helps to segment out bubbles in images.

4.2 Experimental Procedure

Before recording the bubble plume, at first a background image was recorded, as shown in figure 4-2. Then flow was adjusted to the desired flow rate by the globe control valve. Subsequently, two to three minutes were allowed before 6000 images were recorded at a frequency of 50 FPS in two batches of 3000 frames each. Exposure time was adjusted to 500 μs. Acquisition control was done through the Phantom Camera Control Software v675.2 from the Vision Research Inc. Experiments were conducted in a continuous manner without disturbing the camera. Image calibration was done by recording image of a ruler in the plane of investigation. Image resolution was found to be 1.1 pixel/mm. In this manner recordings were made for all the test cases (Tables 2-1 and 2-2).

4.3 Image Processing Algorithm for Bubble Plume Boundary Detection

The acquisition software saved recordings in a cine file format. For a test case two cine files were saved. Using Phantom Cine Viewer 675 software made available by the Vision Research Inc., these cine files were converted to four Multipage Tiff files, each consisting of 1500 images. A code (see Appendix B) was developed in MATLAB which decoupled the Multipage Tiff files in to individual images files. After splitting all 6000 image frames, plume boundary detection program was executed. MATLAB code for plume boundary detection has been provided in Appendix B. The algorithm for plume boundary detection is being explained below.

At first, first frame image (Figure 4-1) and the background frame image (Figure 4-2) were read in MATLAB through Image Processing Toolbox. Since, the plume images and the background image were in colour file format (RGB), so these images were converted to greyscale images. Subsequently,

complemented background image was subtracted from the complemented first frame image to achieve figure 4-3.

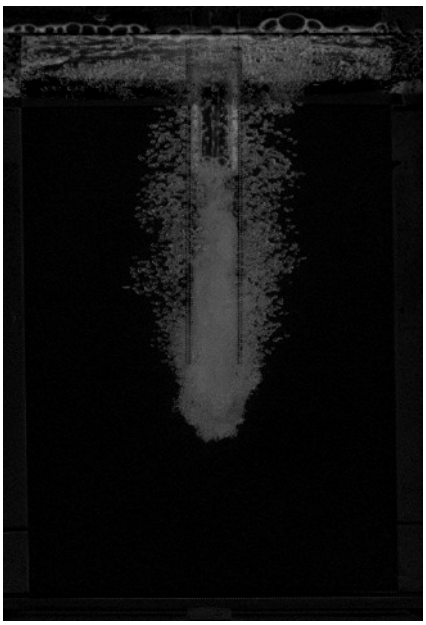

Figure 4-3 Subtracted image

The subtracted image was cropped out to remove unnecessary air space at top. In cropped image, figure 4-4, top pixel line corresponds to free water surface. Considerable amount of bubble present close to the free water surface add noise during plume boundary detection. Therefore a portion of the top region was masked out by setting intensity values of pixels to 0 in that region, as shown in figure 4-5. Figure 4-6 shows histogram of intensity values of the image in figure 4-5. It can be seen that intensity levels below 10 belong to the background, while above 15 belong to bubbles. This difference in intensity levels of background and bubbles is exploited for segmentation of the bubble plume. The image in figure 4-5 was converted in a black and white image with a threshold of 15/256. Figure 4-7 shows the segmented bubble plume. Implementation of boundary detection algorithm at this stage would have led to detection of many boundaries. Therefore, the thresholded bubble plume was further processed. It can be observed in figure 4-7 that some bubbles are present very close to the plume. As a first step of the processing, a criterion was established to count these bubbles in the plume.

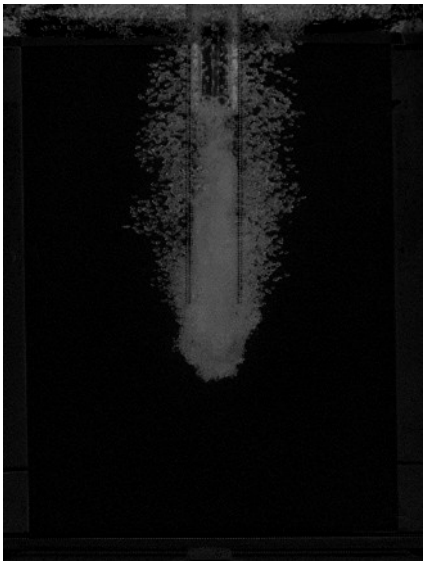

Figure 4-4 Subtracted image with air space cropped out

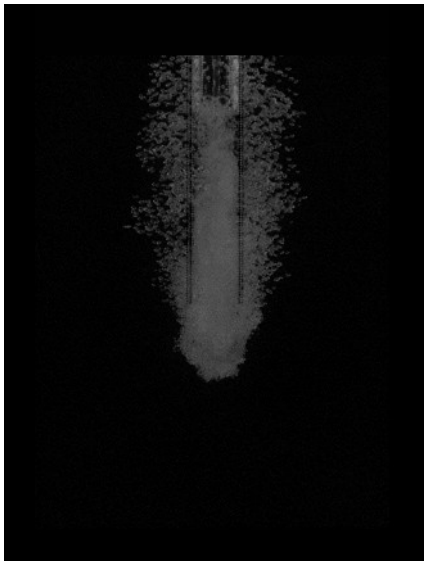

Figure 4-5 Image from figure 4-4 after masking out top region

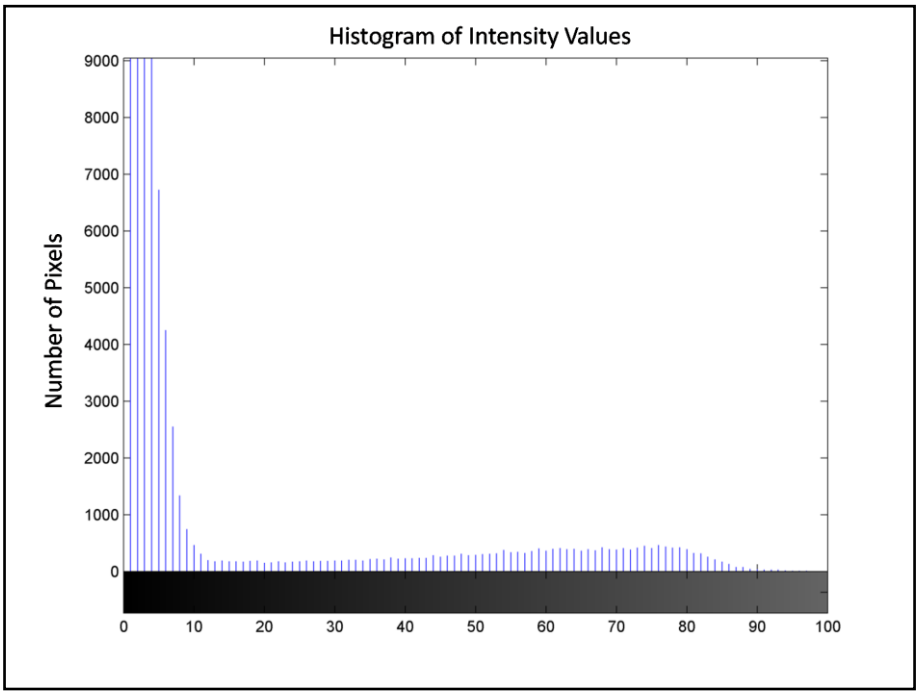

Figure 4-6 Histogram of intensity values of the image in figure 4-5

If bubbles were dispersed less than 18 pixels (~16 mm) from the plume or from the nearest bubble (which was already established a part of the plume) then they were counted in the plume. Frames containing bubbles which are dispersed more than 18 pixels were negligible (<1%) in any test case. This

criterion was important to establish as we are interested in bubble plume only. Highly strayed random bubbles would erroneously tend to affect the ensemble averaged bubble plume profile.

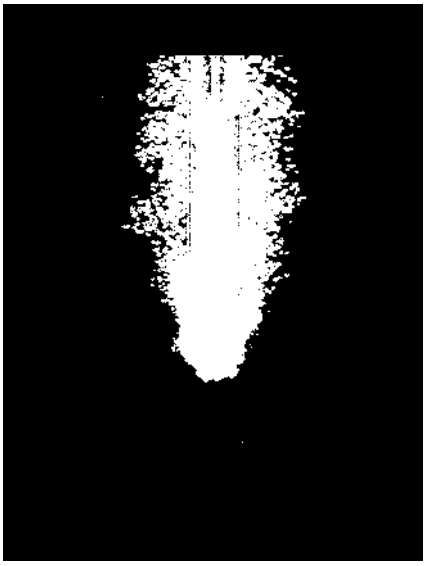

Figure 4-7 Segmented bubble plume

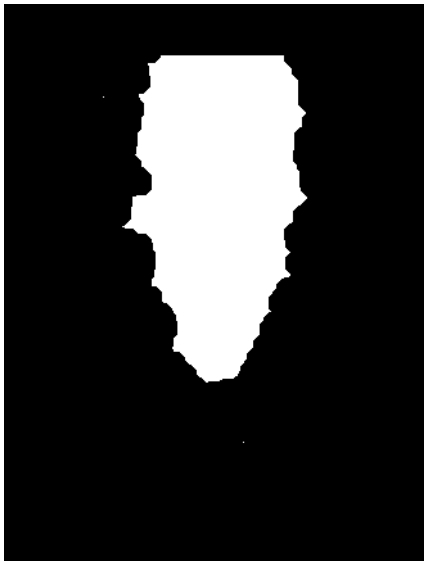

Figure 4-8 Bubble plume after dilation and erosion process

To realize this criterion the image in figure 4-7 was dilated and eroded with a disk shaped filter of 9 pixels radius. Figure 4-8 shows product of the dilation and erosion process. Then all the holes in the eroded image were filled. Subsequently, the image was further eroded with a disk filter of 8 pixels radius to remove any spurious white pixels present around the plume. This eroded image was reconstructed with the image available after filling of holes. Figure 4-9 shows the reconstructed image. In this image, white pixels correspond to bubble plume and boundaries for only one object is needed to be detected. Subsequently, boundary detection algorithm was implemented through 'bwboundaries' function in Image Processing Toolbox. The detected boundary of the plume has been plotted in figure 4-10 over original unprocessed image to show accuracy of the boundary detection process. It can be observed that plume boundary is being detected fairly sharply. During processing, program sequentially stored detected boundaries for all 6000 frames, which were later manually inspected for accuracy.

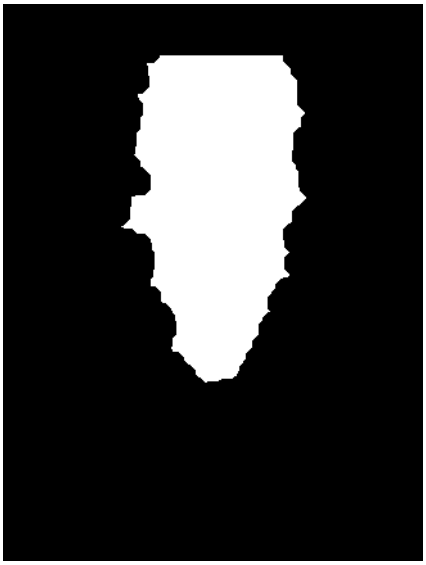

Figure 4-9 Reconstructed bubble plume

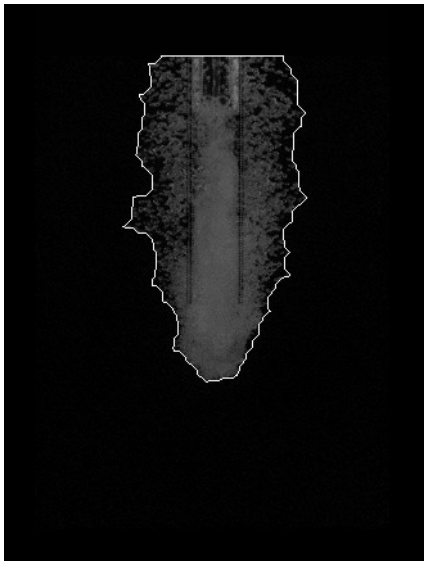

Figure 4-10 Detected boundary plotted over unprocessed image

The detected plume boundary was divided in two parts, left and right hand side contours. The boundary coordinates were saved only up to the end of the downcomer tube. This process was performed on all 6000 images. Left and right hand side coordinates were stored for all the images in two separate multidimensional arrays. Later, left and right hand side coordinates were processed for computation of ensemble average and rms (root means square) values. Pixel coordinates of average and average±rms coordinates were transformed from image space (pixel values) to coordinate space as shown in figure 4-11. MATLAB code for transformation to the coordinate space can be found in Appendix B. In coordinate space, downcomer centreline represent Z axis with origin at the bottom of the tank and positive Z direction towards the free water surface. X axis is in the horizontal right direction. Figure 4-11 shows the ensemble averaged bubble plume profile for the test case of 7 mm nozzle diameter (D_N), 100 mm jet length (H_N) and 12.5 LPM water flow rate. Two continuous black lines in figure 4-11 represent the downcomer. Such plots have been compiled for all the test cases in Appendix C, titled ‘Time Averaged Bubble Plume Profiles’. In the process of acquisition, detection of plume boundaries and transformation to the coordinate space, errors of 1-3 mm can be expected in ensemble averaged plume boundaries.

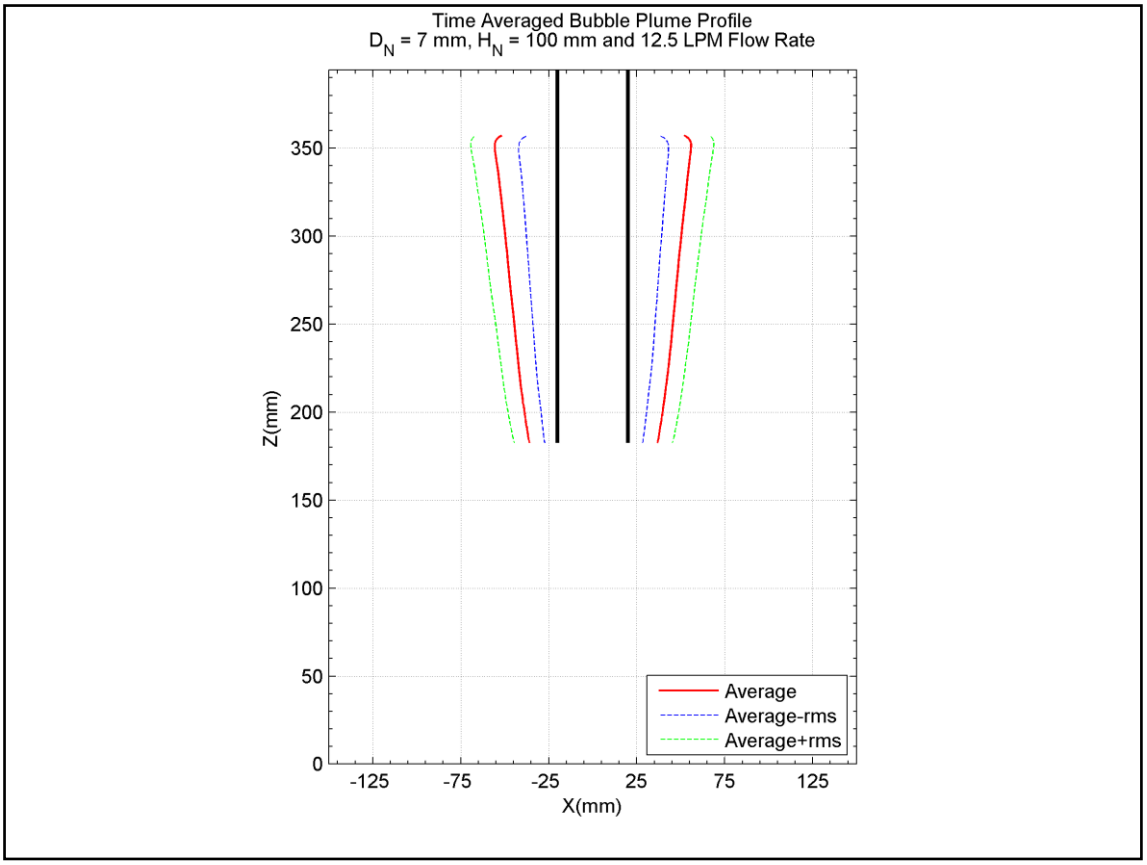

Figure 4-11 Ensemble averaged bubble plume profile for the test case of 7 mm nozzle diameter (D_N), 100 mm jet length (H_N) and 12.5 LPM water flow rate

4.4 Results and Discussion

4.4.1 Impact of Change in Water Flow Rate

In Test Matrix 1 and 2, water flow rate to the inlet nozzle was increased from 7.5 LPM to 15.0 LPM while maintaining same H_N and D_N. Starting from a zero water flow rate, initially no air entrainment was observed until a critical velocity is reached. As the water flow rate was increased further, continuous air entrainment was observed in the downcomer. However, air bubbles did not breakthrough the downcomer in to the outer water pool until flow rate became sufficient enough that, downward moving water in the downcomer tube was able to overcome buoyancy forces on bubbles. Figure 4-12 shows a photograph for the test condition of 7mm D_N, 25 cm H_N and 7.5 LPM water flow rate and

figure 4-13 shows the time averaged bubble plume profile for this test case. It can be observed that 7.5 LPM water flow rate is not sufficient enough to drag the bubbles out of the downcomer. Bubbles present inside the downcomer tube occupy space therefore water in downcomer tube was lifted and it was found to flow out of the square recess.

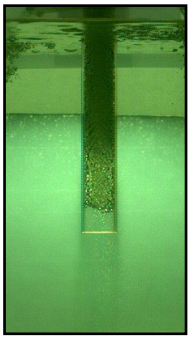

Figure 4-12 A snapshot for D_N = 7mm, H_N = 250 mm, Water Flow Rate = 7.5 LPM

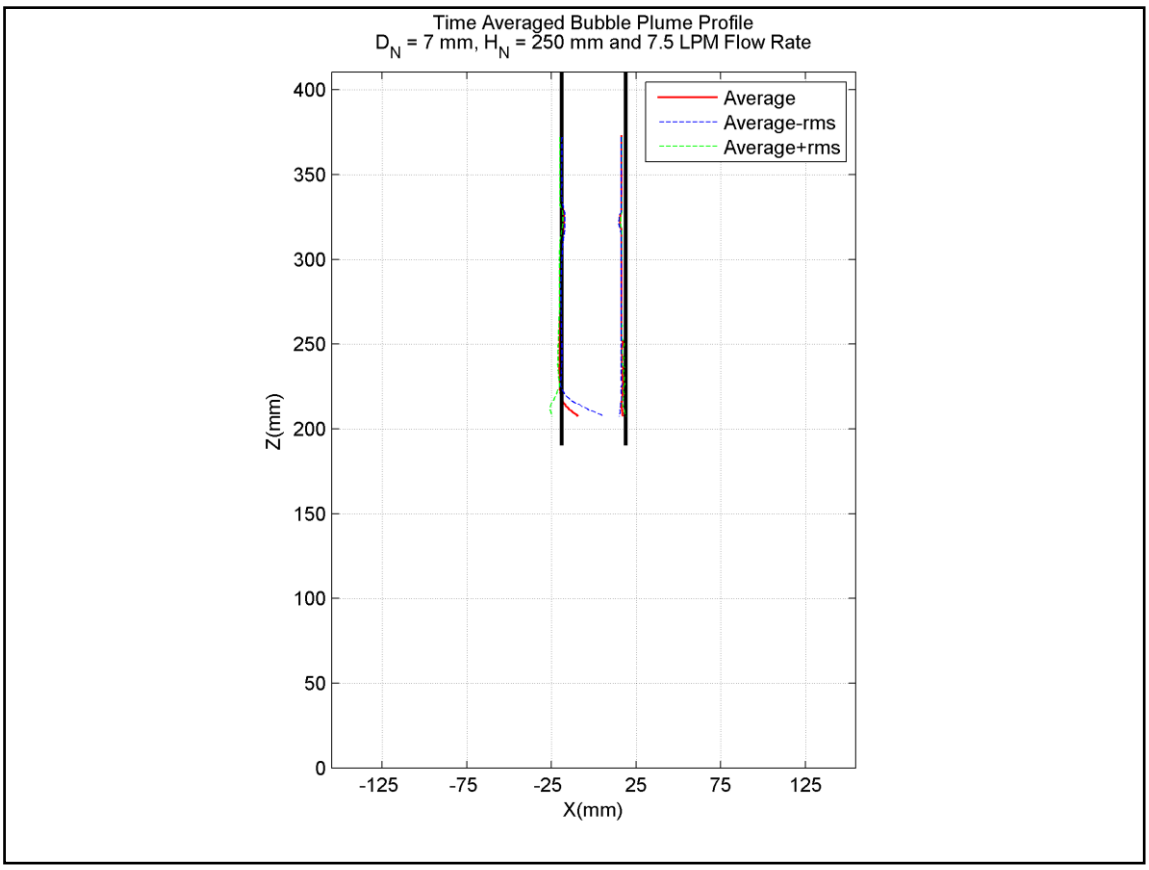

Figure 4-13 D_N = 7mm, H_N = 250 mm, Water Flow Rate = 7.5 LPM

In figure 4-13, time averaged bubble plume profile is slightly disturbed around Z = 210 mm. An explanation can be provided by the fact that, in considerable number of frames bubble plume inside the downcomer tube is not penetrating beyond this position. In the absence of plume, wrong contours were detected after Z = 210 mm, which resulted in an error in averaged and rms plume boundaries.

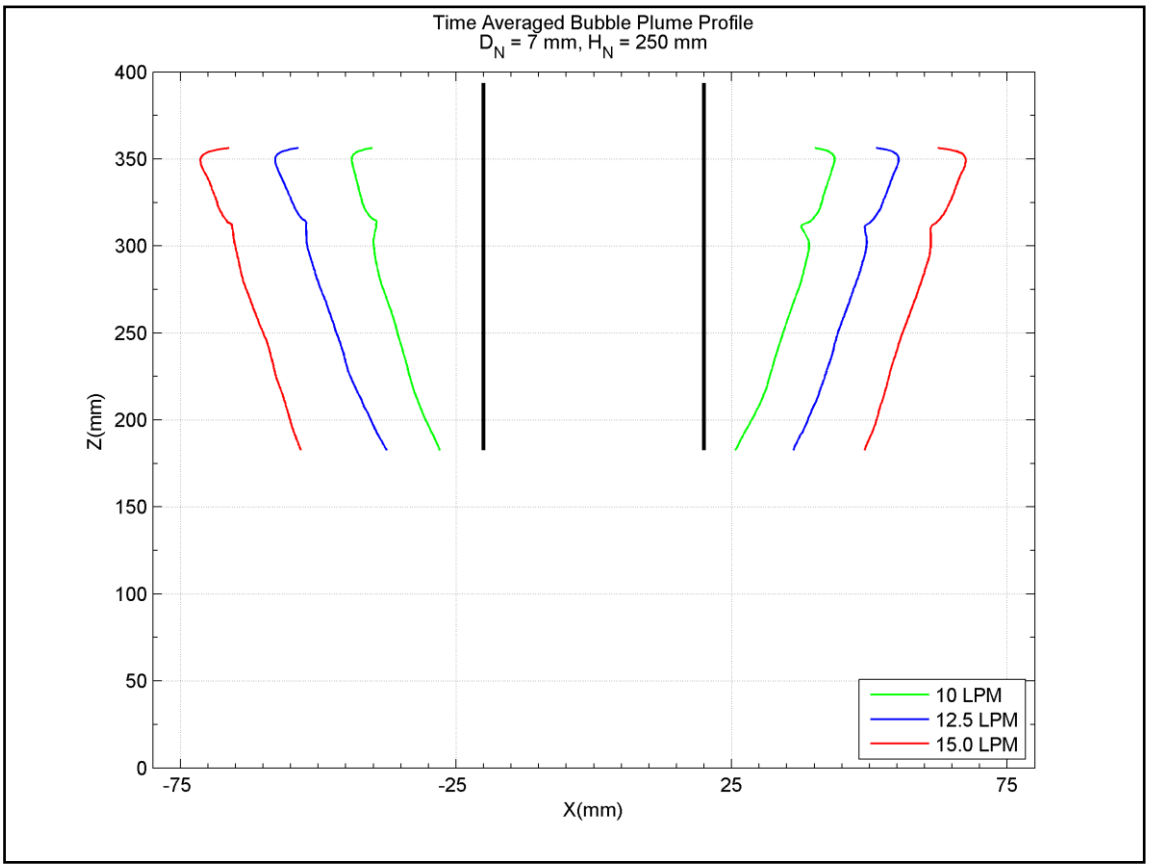

Figure 4-14 Plume profiles for 10.0, 12.5 and 15.0 LPM flow rate (at D_N = 7mm, H_N = 250 mm)

As the water flow rate was increased beyond 7.5 LPM, continuous flow of air was observed in the outer pool. Figure 4-14 shows plume profiles for 10.0, 12.5 and 15.0 LPM flow rate (at D_N = 7mm, H_N = 250 mm). It can be observed that with increase in water flow rate, plume boundaries increase in width. Ohkawa et al. (1986) showed that increase in water jet velocity leads to a higher air entrainment rate in a downcomer tube. Hence, in present case with increase in water flow rate, a greater amount of air is being entrained. At the same moment

water flow velocity in the downcomer tube is increasing to a level that it is able to drag more and more air bubbles in to the outer pool. Hence, at higher water flow rates a larger amount of area can be aerated outside the downcomer tube. Similar trend of increase in bubble plume width with rise in water flow rate has been observed in all the test cases. Figure 4-15 shows the plume profiles for D_N = 10mm, H_N = 150 mm.

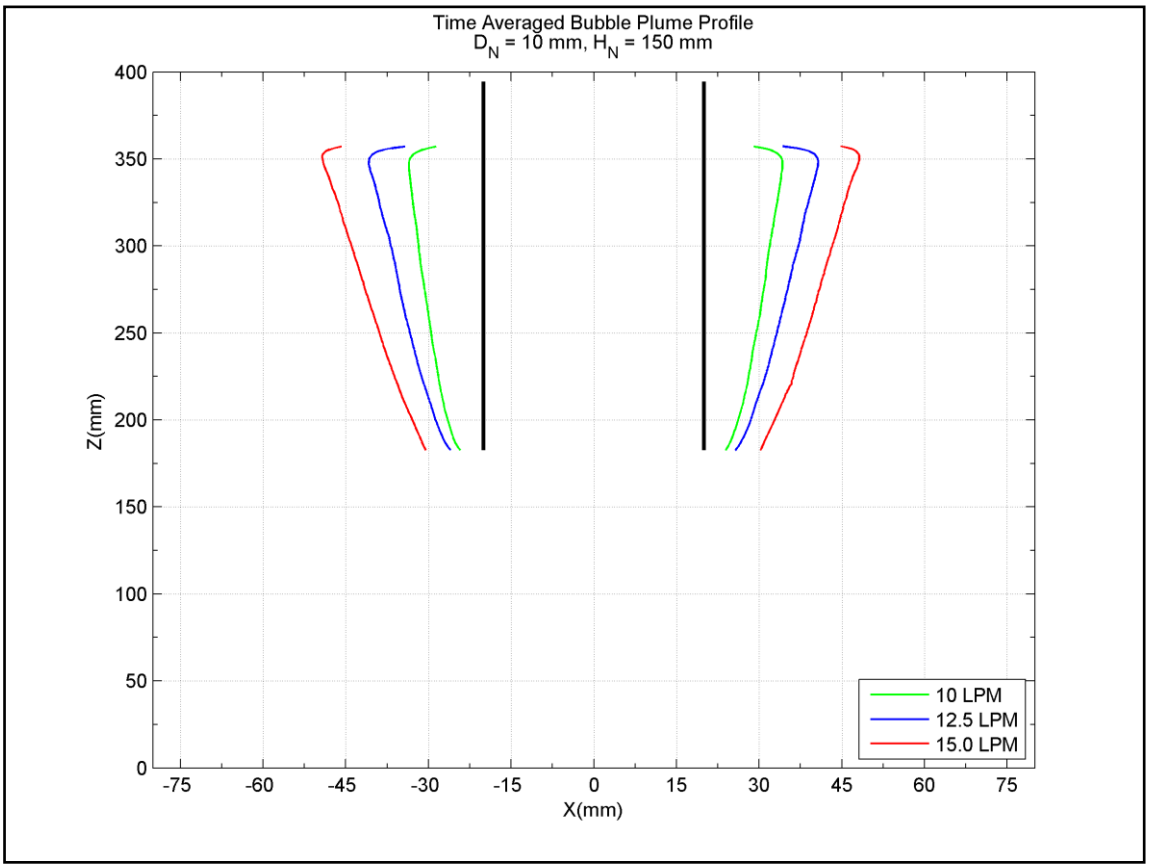

Figure 4-15 Plume profiles for 10.0, 12.5 and 15.0 LPM flow rate (at D_N = 10mm, H_N = 150 mm)

In bubble profiles (figure 4-14), a small kink can be observed close to Z = 310 mm. It was caused by an adhesive tape mark on the back wall of the acrylic tank, which resulted in noise during image processing and caused plume profiles to be slightly blurred in that region. In reality bubble plume profiles are rather smooth. It was removed later during experiments, so it will not appear in many test cases e.g., see figure 4-15. Similarly, boundary detection process becomes inaccurate close to the image borders, as a result of it, averaged

plume profile appear to be curved towards the downcomer tube at Z = 350 mm. It is a processing error. In reality plume profiles are smoothly diverging beyond Z = 350 mm to the free surface of the pool. Hence, averaged plume profiles beyond 350 mm should be neglected.

4.4.2 Impact of Change in Jet Length (H_N)

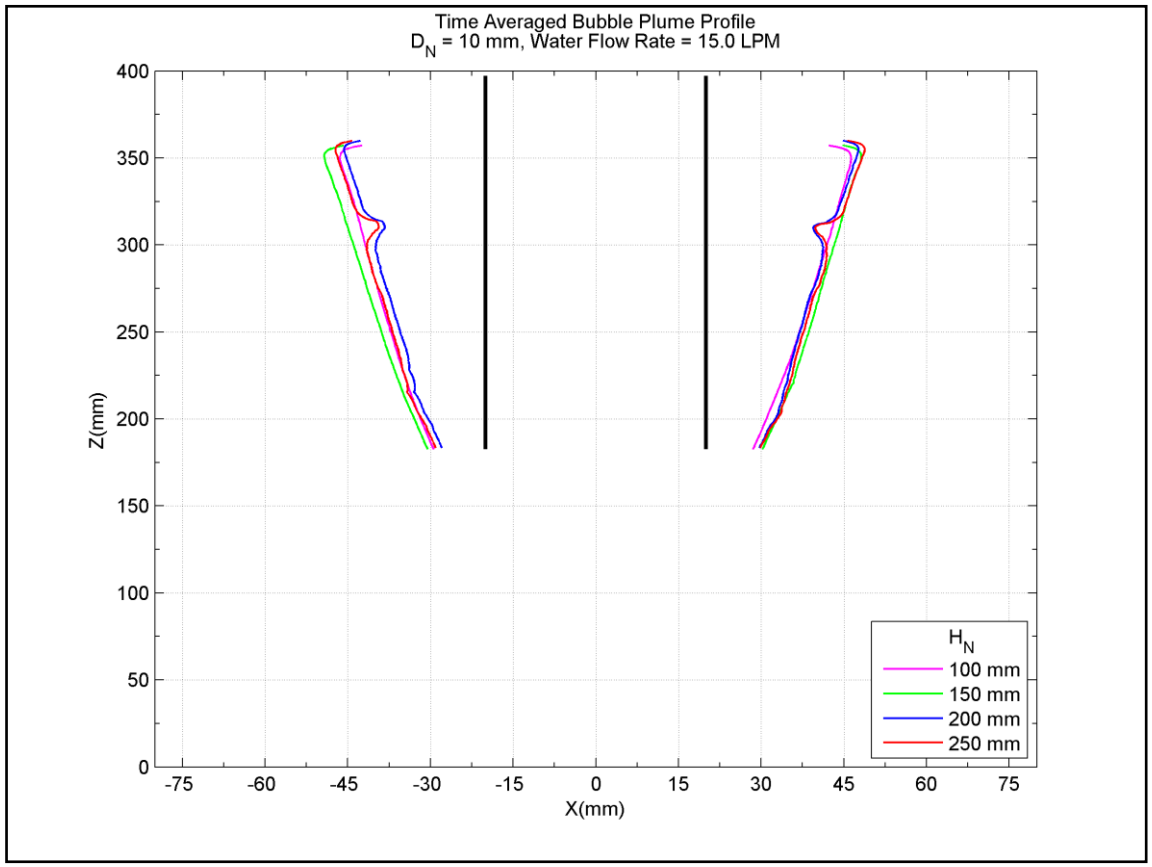

Figure 4-16 Plume profiles for 100, 150, 200 and 250 mm Jet Length (at D_N = 10mm, 15.0 LPM Water Flow Rate)

For the same water flow rate and D_N, jet gains greater momentum under gravity with increase in jet length. This gain in energy is expected to be utilized in moving more bubble out of the downcomer. So, bubble plume profiles were expected to be wider with increase in jet length. Figure 4-16 shows effect of change in jet height on plume profiles at D_N = 10mm and 15.0 LPM Water Flow Rate. Results show that contrary to our expectation there is no monotonic relationship with H_N. Figure 4-17 shows the results for D_N = 10mm and 12.5

LPM Water Flow Rate. In this case bubble plume profiles are almost overlapping with each other. Same effect was observed for other test cases too, where irrespective of H_N plume profiles were found to be approximately same. Similar results were reported by Danciu et al. (2009) for a plunging jet system where penetration depth of bubble plume was not found to be monotonically affected by H_N.

This phenomenon can be explained by the fact that with increase in H_N two opposite effects play the role,1) jet momentum increases, 2) jet surface instabilities become more pronounced and therefore rate of air entrainment increases. So, increased jet momentum is counteracted by increased buoyant forces due to the presence of more bubbles. Hence, plume profiles are not being affected.

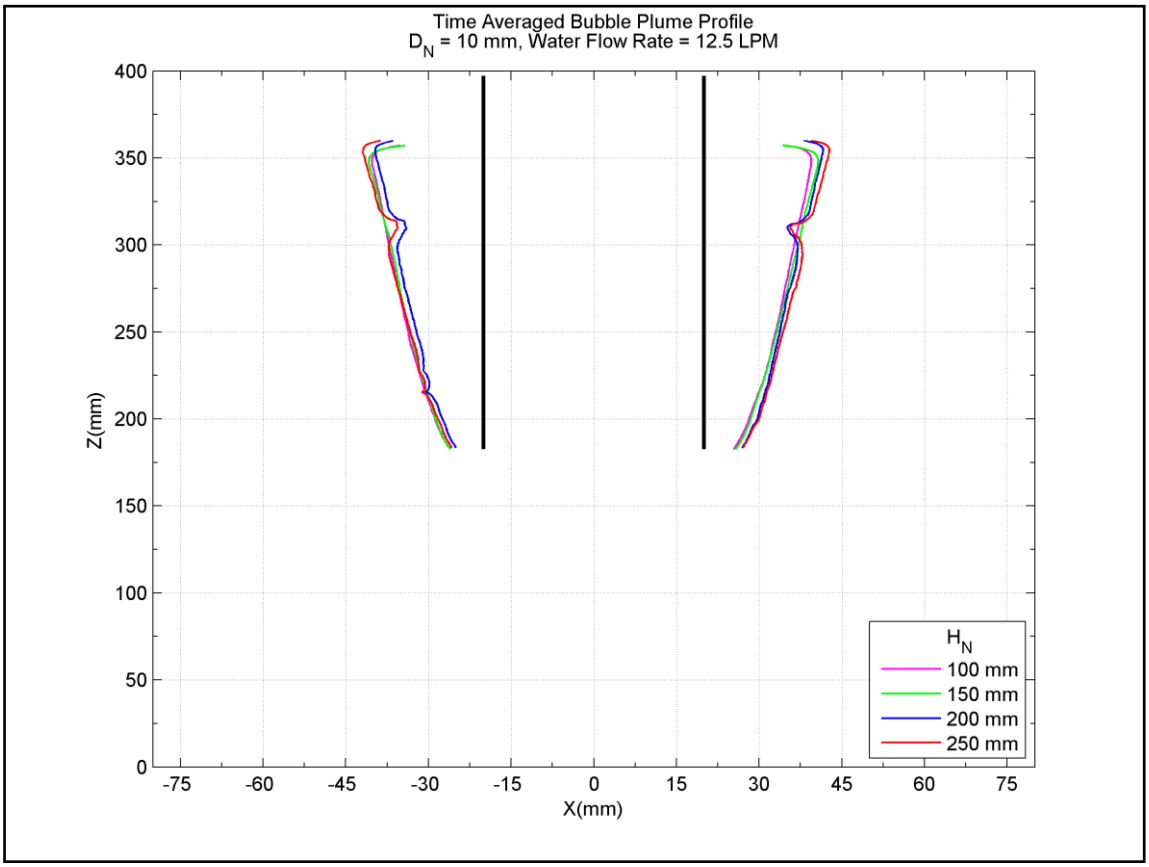

Figure 4-17 Plume profiles for 100, 150, 200 and 250 mm Jet Length (at D_N = 10mm, 12.5 LPM Water Flow Rate)

4.4.3 Impact of Change in Nozzle Diameter (D_N)

Increasing the nozzle diameter, while maintaining the same water flow rate and jet height (H_N) resulted in significant reduction in plume extents, as shown in figures 4-18 and 4-19. Difference in plume extents was found greater at higher water flow rates. For the water flow rate of 15 LPM plume extents with D_N = 7 mm were found to be approximately 2-3 times, in width of plume extents for 10 mm D_N. Using the air entrainment rate (Q_a) correlation developed by Ohkawa et al. (1986), for the same downcomer diameter and height it can be shown that

$$Q_a \propto \left(V_j^3 D_N^2\right)^{0.8} (D_N)^{1.3} \qquad \textbf{(4-1)}$$

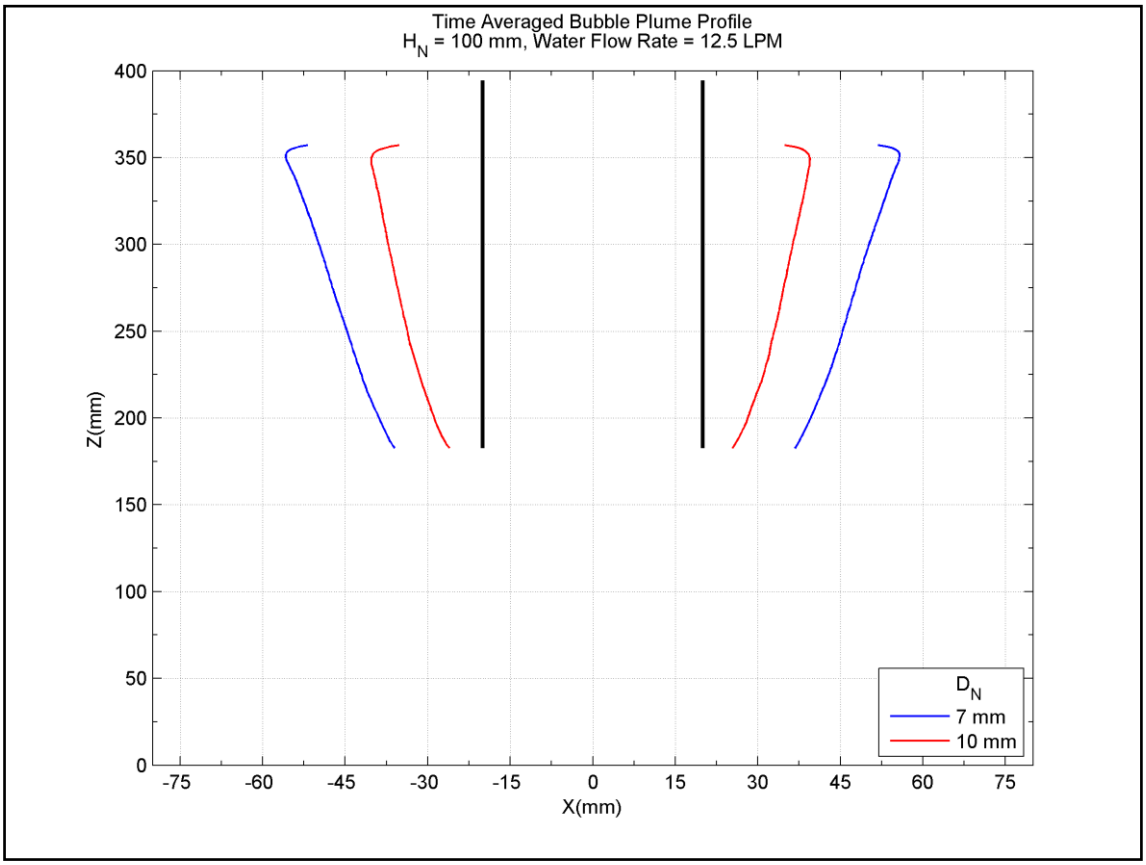

Figure 4-18 Plume profiles for D_N = 7 mm and 10 mm (at H_N = 100 mm, 12.5 LPM Water Flow Rate)

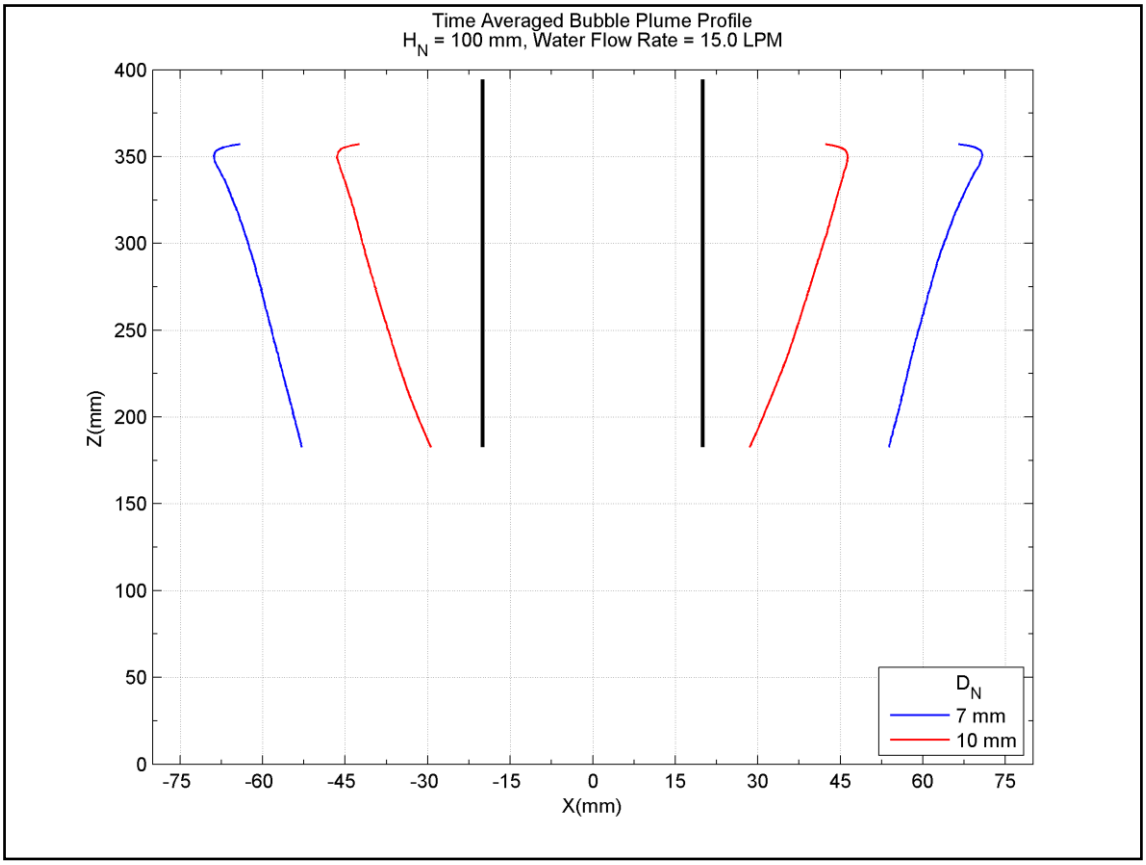

Figure 4-19 Plume profiles for D_N = 7 mm and 10 mm (at H_N = 100 mm, 15.0 LPM Water Flow Rate)

Neglecting the effect of jet length on jet velocity, V_J can be approximated to be V_N. Since, water flow rate is same, therefore $V_N D_N^2$ is constant for both the nozzles. With this relation equation 4-1 can be reduced to

$$Q_a \propto (D_N)^{-1.9} \qquad \textbf{(4-2)}$$

Hence increasing the D_N from 7 mm to 10 mm will reduce the air entrainment rate by approximately 50%. It is expected that this reduced air entrainment rate results in lesser amount of air flow from the downcomer in to the outer pool, which is expected to reduce the plume extents. Moreover, 7 mm nozzle diameter jet has higher impingement velocity than 10 mm diameter jet. Hence, comparatively more intense mixing zone is formed in the case of 7mm jet. This stronger shear flow leads to generation of finer bubbles in the mixing zone. These finer bubbles experience lesser drag force and hence pulled down the

downcomer tube in to the outer pool more effectively. It results in greater air flow rate to the outer pool and greater plume extents for the 7 mm D_N jet. However, this thesis is needed to be corroborated by bubble measurements in the mixing zone. Due to lack of instrumentation and time, it was not attempted in present work. In the end, an important conclusion is drawn that for the same H_N and water flow rate plume boundaries increase in width with decrease in D_N. It means that greater area outside the downcomer can be aerated with smaller diameter jet.

4.4.4 Impact of Change in Water Flow Rate, Jet Length and Nozzle Diameter on Bubble Plume Depth

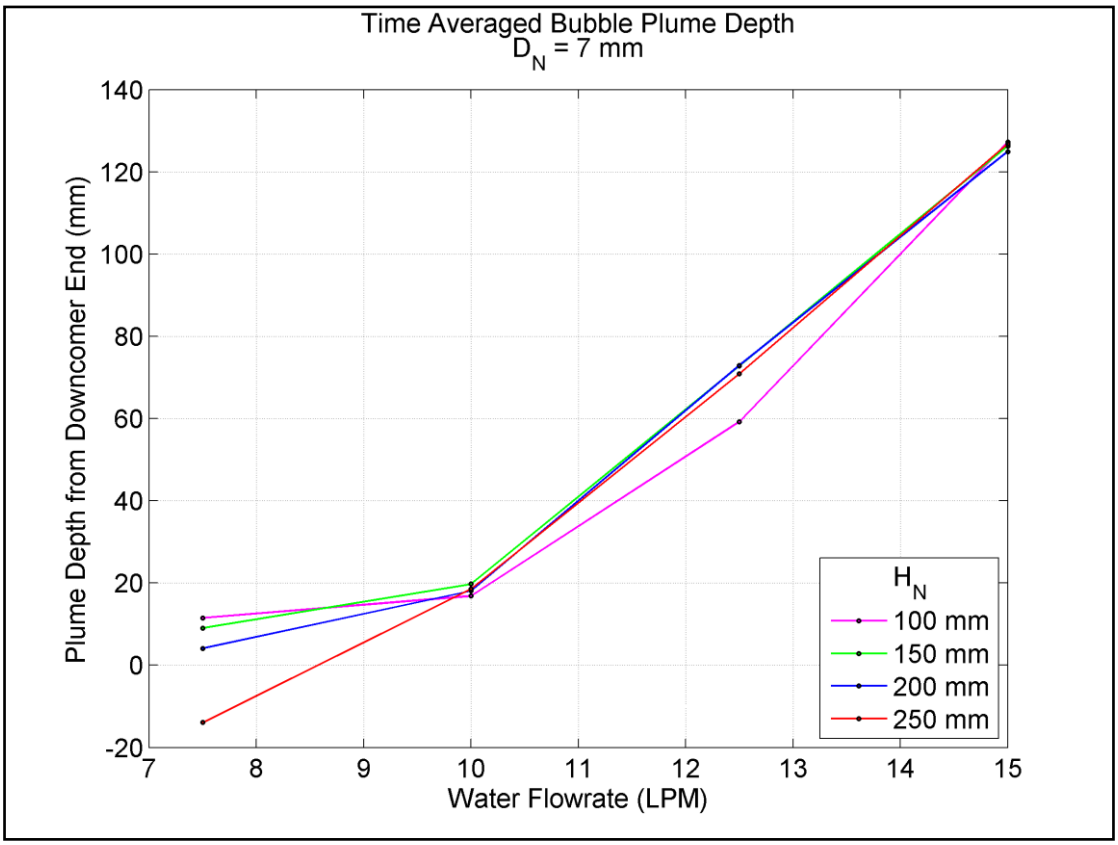

Figure 4-20 Variation of bubble plume depth with water flow rate and H_N for 7 mm D_N

Figure 4-20 shows variation of plume depth with water flow rate and H_N for the 7 mm (D_N) jet. It can be seen that with increase in water flow rate the plume depth increases monotonically.

Results also show that at 250 mm H_N and 7.5 LPM, bubble plume does not penetrate beyond the downcomer tube. It ratifies the time averaged bubble plume profile shown in figure 4-13, in section 4.4.1. With decrease in jet height, plume breaks through the downcomer tube at 7.5 LPM. Similar trend was observed with 10 mm (D_N) jet, where plume is confined inside the tube at 250 mm H_N, as shown in figure 4-21. In these experiments water flow rate of 7.5 LPM is close to the critical flow rate for bubbles to breakthrough the downcomer tube. Moving beyond the critical flow rate, for those test conditions where plume is distinctly present in the outer pool, plume depth is rather found to be unsystematically affected by the change in H_N. In fact in many cases results were found to be overlapping, as shown in figure 4-20 and 4-21.

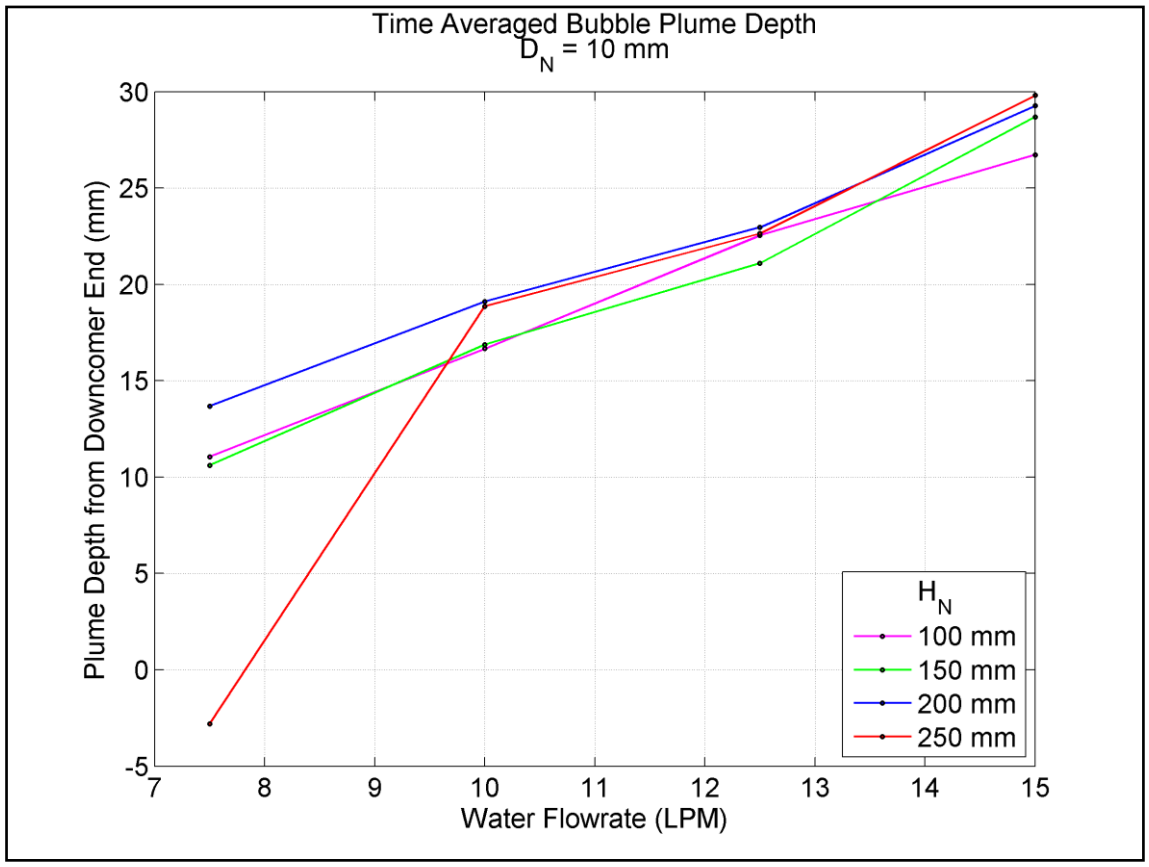

Figure 4-21 Variation of bubble plume depth with water flow rate and H_N for 10 mm D_N

Figure 4-22 shows the effect of change in nozzle diameter on plume depth. From results it is clear that with increase in D_N, plume depth decreases

considerably. Differences in plume depths were found to be higher at greater flow rates. Increase in plume depth for smaller nozzle diameter jet is expected to be caused by formation of finer bubbles, which are more effectively pulled deeper in to the pool.

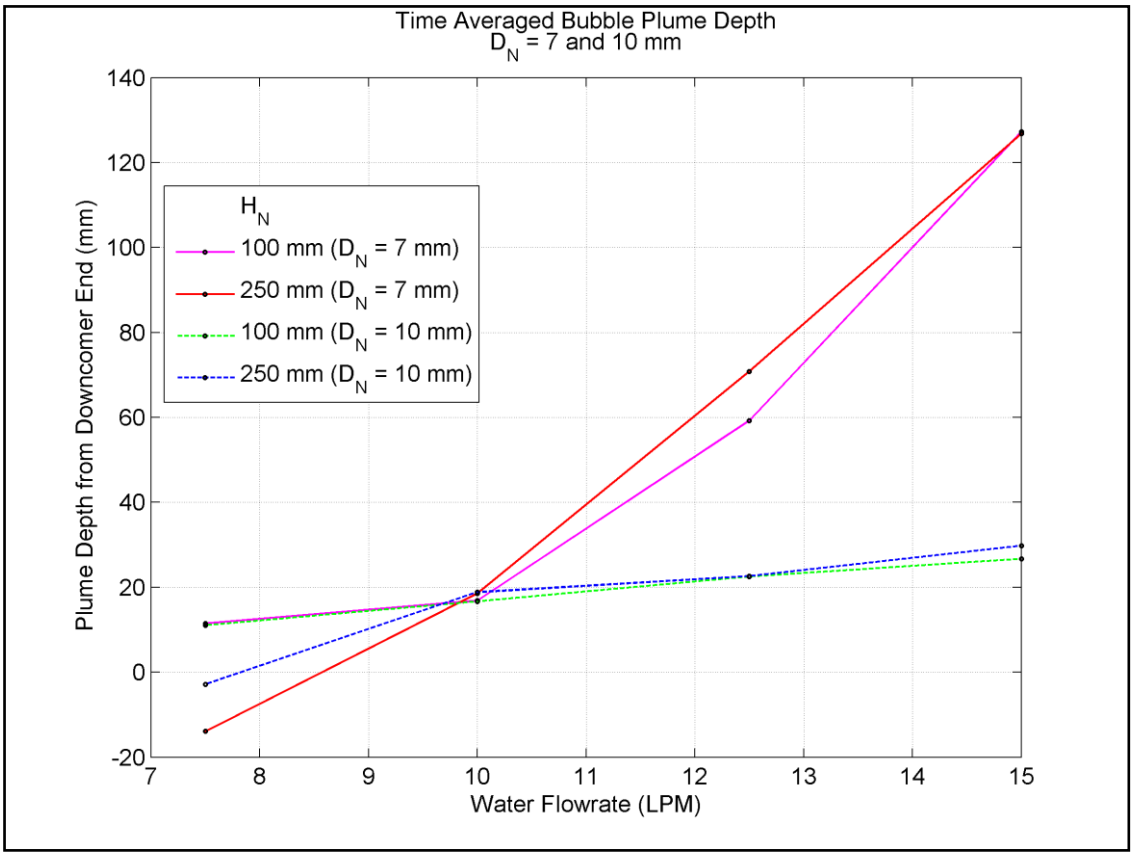

Figure 4-22 Variation of bubble plume depth with, water flow rate, H_N and D_N

4.4.5 Global Bubble Plume Dynamics

In experiments plume was found to dynamically sway in transverse direction, as shown in figure 4-23. Similar dynamic bubble plumes have been observed by previous researchers in rectangular bubble columns. A detailed dynamic analysis of plume is out of the scope of the present work. However, rms of the geometric centre of the plume was evaluated. It serves as a measure of the plume fluctuations. Figure 4-24 shows its variation with height (Z) for one test case. It can be observed that with increase in Z, side by side or transverse

fluctuations of plume also increase. This similar trend can be observed in rms values of the left and right plume boundaries (Appendix C), where in all the test cases Average+rms values tend to grow with Z.

Figure 4-23 Transverse fluctuations of bubble plume

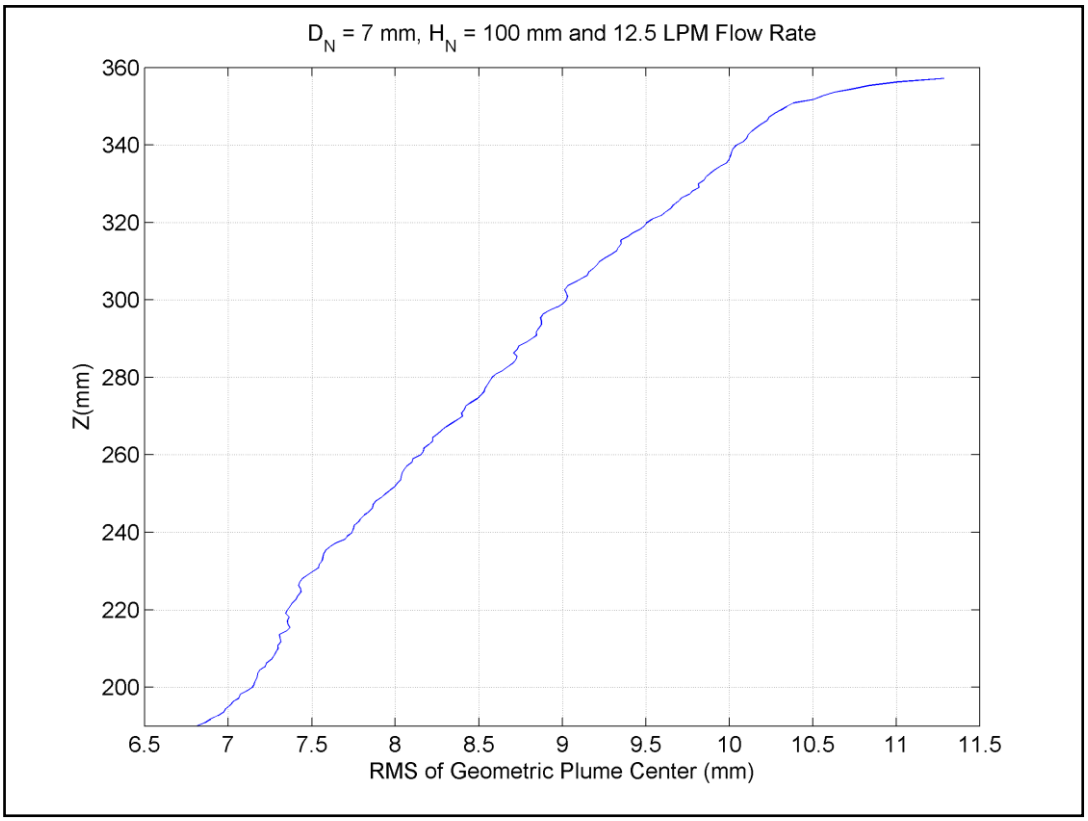

Figure 4-24 Variation of root mean square of the geometric plume centre for the test case of 7mm D_N, 100 mm H_N and 12.5 LPM water flow rate

5 CFD SIMULATION OF BUBBLE PLUME DISPERSION

5.1 Introduction

Bubble plume dispersion in a CPLJ unit is a two-phase flow marked by presence of many interfaces. Mathematically such a flow can be defined as single phase areas separated by dynamic boundaries. Single phase differential balance equations can be applied to each of the single phase regions with appropriate jump and boundary conditions at the interfaces. Hence, theoretically a mathematical set of equations defining local behaviour of flow can be developed. Such a formulation is known as a local instant formulation. Mathematical and computational efforts required for achieving solution from a local instant formulation are prohibitively great. Hence, it is used as a base for developing simpler macroscopic field equations by appropriate averaging schemes.

Mathematical difficulty in local instant formulation lies in high frequency motion of numerous dynamic interfaces. In this sense, averaging procedure removes interfaces and limits two phases occurring at a location sequentially by a co-existing smooth continuum with probability of finding any phase at that location given by α_k. α_k is commonly known as local void fraction of the k^{th} phase. CFD simulations in this work utilize two-fluid Euler-Euler model which is obtained by ensemble averaging of local instant field equations. Interested readers are referred to Ishii's (2011) seminal work for more discussion on derivation of the field equations for the two-fluid model.

5.2 Governing Equations

The field equations for two-fluid model are given below:

5.2.1 Mass Balance

Conservation of mass for a phase k can be represented by:

$$\frac{\partial}{\partial t}(\alpha_k \rho_k) + \nabla \cdot \left(\alpha_k \rho_k \vec{U}_k\right) = I_k \tag{5-1}$$

For air-water flow it leads to two mass balance equations, one for air phase and other for water phase. Both these equations are connected by interfacial mass transfer condition of

$$\sum_{k=1}^{2} I_k = 0 \tag{5-2}$$

where I_k is an interfacial mass transfer term. In present case, air-water mass transfer was neglected therefore equation 5-2 was reduced to equation 5-3.

$$I_k = 0 \tag{5-3}$$

5.2.2 Momentum Balance

Field equations for conservation of momentum are as follows:

$$\begin{aligned}\frac{\partial}{\partial t}\left(\alpha_k \rho_k \vec{U}_k\right) + \nabla \cdot \left(\alpha_k \rho_k \vec{U}_k \otimes \vec{U}_k\right) \\ = -\alpha_k \nabla p - \nabla \cdot (\alpha_k \tau_k) + \alpha_k \rho_k \vec{g} + \vec{M}_{ik}\end{aligned} \tag{5-4}$$

In equation 5-4, right hand side terms denote the effect of pressure gradient, laminar and turbulent shear stresses, gravity force and interfacial momentum transfer term, respectively. It is important to note the underlying assumption that at any point same pressure is shared by all phases. Using Boussinesq approach τ_k is provided by equation 5-5.

$$\tau_k = -\mu_{eff,k}\left(\overrightarrow{\nabla U_k} + \left(\overrightarrow{\nabla U_k}\right)^T - \frac{2}{3} I\left(\nabla . \overrightarrow{U_k}\right)\right) \tag{5-5}$$

where $\mu_{eff,k}$ is the effective viscosity of the phase k and I is the identity tensor.

Two momentum balance equations for air and water phase are connected by the interfacial momentum transfer condition of equation 5-6.

$$\sum \vec{M}_{ik} = 0 \quad \textbf{(5-6)}$$

$\vec{M}_{ik}$ is also known as generalized drag force. It specifies the interfacial surface forces. It is a linear combination of interfacial drag force, lift force, wall lubrication force, virtual mass force and turbulent dispersion force, as given in equation 5-7.

$$\vec{M}_{iL} = -\vec{M}_{iG} = \vec{M}_L^D + \vec{M}_L^L + \vec{M}_L^{WL} + \vec{M}_L^{VM} + \vec{M}_L^{TD} \quad \textbf{(5-7)}$$

5.3 Generalized Drag Force Modelling

Components of generalized drag force are provided by empirical correlations developed by many researchers over the years. In order to derive the correlations air phase is modelled as bubbles. Discussion of the models used in this work is provided below.

5.3.1 The Drag Force

Momentum exchange by drag force per unit volume can be written as equation 5-8.

$$\vec{M}_L^D = \frac{3}{4} C_D \frac{\alpha_G \rho_L}{d_B} \left|\vec{U}_G - \vec{U}_L\right| (\vec{U}_G - \vec{U}_L) \quad \textbf{(5-8)}$$

where C_D is the drag coefficient, α_G, gas void fraction, ρ_L, density of the liquid phase, and d_B, mean bubble diameter of the gas phase. $\vec{U}_G$ and $\vec{U}_L$ are velocity vectors for gas and liquid phase. Given the volume of a bubble (V_B), mean bubble diameter is determined by equation 5-9.

$$d_B = \sqrt[3]{\frac{6V_B}{\pi}} \quad \textbf{(5-9)}$$

Drag coefficient is dependent on particle Reynolds Number ($Re_B = \frac{\rho_L |\vec{U}_G - \vec{U}_L| d_B}{\mu_L}$). For Reynolds Number in viscous regime ($Re_B << 1$), dispersed fluid particles

(bubbles) are spherical in shape. In this regime, the drag coefficient is provided by correlation proposed by Schiller and Naumann (1935, cited in Ali et al., 2008), equation 5-10.

$$C_D(Sphere) = \frac{24}{Re_B}(1 + 0.15 \times Re_B^{0.687}) \quad \textbf{(5-10)}$$

At larger Reynolds number particle shape distorts to an ellipsoid (distorted particle regime) and ultimately to a spherical cap shape. In spherical cap regime, drag coefficient is given by equation 5-11.

$$C_D(cap) = \frac{8}{3} \quad \textbf{(5-11)}$$

In a CPLJ system bubbles were approximately spherical up to 1-2D_C below the point of jet impingement. However, bubbles outside the downcomer tube were found to be larger and distorted in shape, as shown in figure 5-1. For distorted particle regime drag coefficient correlation developed by Grace (Clift et al., 1978) was utilized. In this regime drag coefficient is strongly related to particle shape which is incorporated through Eötvös Number (equation 5-12) and Morton Number (equation 5-13). The drag coefficient is provided by equation 5-14.

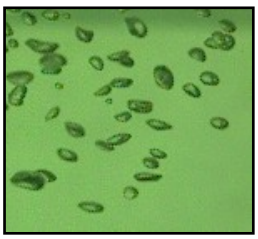

Figure 5-1 A snapshot of bubbles outside the downcomer in water tank

$$E_O = \frac{g(\rho_L - \rho_G)d_B^2}{\sigma} \quad \textbf{(5-12)}$$

$$M_O = \frac{g\mu_L^4(\rho_L - \rho_g)}{\rho_L^2\sigma^3} \quad \textbf{(5-13)}$$

$$C_D(ellipse) = \frac{4}{3}\frac{g d_B}{U_T^2}\frac{(\rho_L - \rho_G)}{\rho_L} \quad \textbf{(5-14)}$$

where σ is the surface tension coefficient and U_T is the bubble terminal velocity determined by equations 5-15 to 5-17.

$$U_T = \frac{\mu_L}{\rho_L d_B} M_O^{-0.149}(J - 0.857) \quad \textbf{(5-15)}$$

$$J = \begin{cases} 0.94H^{0.757}, & 2 < H \leq 59.3 \\ 3.42H^{0.441}, & H > 59.3 \end{cases} \quad \textbf{(5-16)}$$

$$H = \frac{4}{3} E_O M_O^{-0.149} \left(\frac{\mu_L}{\mu_{ref}}\right)^{-0.14} \quad \textbf{(5-17)}$$

where μ_{ref} (0.0009 kgm^{-1}s^{-1}) is the reference viscosity. It is taken to be equal to the dynamic viscosity of water at standard conditions.

ANSYS CFX fuses the above mentioned relations to determine the drag coefficient by equation 5-18

$$C_D(distorted) = minimum\big(C_D(ellipse), C_D(cap)\big)$$
$$C_{D,1} = maximum(C_D(Sphere), C_D(distorted)) \quad \textbf{(5-18)}$$

$C_{D,1}$ is the drag coefficient for flow past a single bubble. For high void fraction dispersed flow regime, it is modified by a volume fraction correction exponent, n, given by equation 5-19. In this work n was set to 2, as per ANSYS CFX solver modelling guidelines.

$$C_D = \alpha_L^n C_{D,1} \quad \textbf{(5-19)}$$

5.3.2 The Lift Force

A fluid particle moving in a shear liquid field experiences a lift force perpendicular to relative velocity of the flow due to asymmetrical flow field

around itself. This shear and wake induced transverse lift force per unit volume is described by Zun (1980), equation 5-20.

$$\vec{M}_L^L = C_L \alpha_G \rho_L \left(\vec{U}_L - \vec{U}_G\right) \times (\nabla \times \vec{U}_L) \quad \textbf{(5-20)}$$

where C_L is the lift force coefficient. Tomiyama et al. (2002) conducted experiments on single air bubbles in a Glycerol-Water solution flowing in a cylindrical tube. They showed that for small air bubbles lift coefficient is positive and depends on Bubble Reynolds Number. However, for large bubbles lift coefficient becomes negative in sign and depends on shape through a modified Eötvös Number (E_{O_d}). The lift coefficient sign reversal was found to occur at around 5.8 mm for an air-water system. Even though, correlations of C_L were based on experiments on a highly viscous Glycerol-Water solution, Tomiyama et al. (2002) demonstrated that they are equally applicable to low viscosity air-water flow. ANSYS CFX utilizes slightly modified form of the correlations developed in Tomiyama et al. (2002). The lift coefficient has been limited to -0.27 for $E_{O_d} > 10$ in CFX, as reported in Prasser et al. (2008) and Lucas et al. (2007). Correlation is given by equations 5-21 and 5-22. Long axis of deformable bubble is used as a characteristic length scale (d_H) in calculation of E_{O_d}, equation 5-23. Assuming a bubble to be a spheroid, d_H is given by equation 5-24.

$$C_L = \begin{cases} minimum\left[0.288\tanh(0.121Re_B), f\left(E_{O_d}\right)\right], & E_{O_d} < 4 \\ f\left(E_{O_d}\right), & 4 \le E_{O_d} \le 10 \\ -0.27, & E_{O_d} > 10 \end{cases} \quad \textbf{(5-21)}$$

$$f\left(E_{O_d}\right) = 0.00105E_{O_d}^3 - 0.0159E_{O_d}^2 - 0.0204E_{O_d} + 0.474 \quad \textbf{(5-22)}$$

$$E_{O_d} = \frac{g(\rho_L - \rho_G)d_H^2}{\sigma} \quad \textbf{(5-23)}$$

$$d_H = d_B(1 + 0.163E_O^{0.757})^{\frac{1}{3}} \quad \textbf{(5-24)}$$

5.3.3 The Wall Lubrication Force

Experiments conducted by various researchers on air-water flow in a pipe revealed absence of air phase near a wall. It has been also observed in present work. Antal (1991) resolved this by deriving a wall lubrication force which prevents bubbles from coming very close to the wall. As a bubble moves closer to the wall, due to no slip flow condition, drainage rate between the wall and bubble becomes smaller than the drainage rate on the other side. This non symmetric flow distribution results in a wall lubrication force which pushes the bubble away from the wall leading to zero void fraction profile at the wall. Antal (1991) derived following formulation for the wall lubrication force:

$$\vec{M}_L^{WL} = -C_{WL}\alpha_G\rho_L\left|(\vec{U}_G - \vec{U}_L) - [\vec{n}_w \cdot (\vec{U}_G - \vec{U}_L)]\vec{n}_w\right|^2\vec{n}_w \quad \textbf{(5-25)}$$

$$C_{WL} = \frac{2C_{w1}}{d_B} + \frac{C_{w2}}{Y_w} \quad \textbf{(5-26)}$$

$$C_{w1} = -0.104 - 0.06(\vec{U}_G - \vec{U}_L),\ C_{w2} = 0.147 \quad \textbf{(5-27)}$$

where C_{WL} is the wall lubrication force coefficient and $\vec{n}_w$ is the unit normal vector away from the wall. Y_w is the distance of bubble centre from the wall. C_{w1} and C_{w2} are coefficients, computed by equation 5-27. Tomiyama (1998) improved Antal's (1991) model for pipe flow and gave following formulation, equation 5-28.

$$C_{WL} = C_{W3}\frac{d_B}{2}\left(\frac{1}{Y_w^2} - \frac{1}{(D - Y_w)^2}\right) \quad \textbf{(5-28)}$$

where D is the pipe diameter and C_{W3} is a function of Eötvös Number. ANSYS CFX utilizes a slightly different version of the correlation proposed by Tomiyama (1998), as given in equation 5-29.

$$C_{W3} = \begin{cases} e^{(-0.933E_O + 0.179)}, & 1 \le E_O \le 5 \\ 0.00599E_O - 0.0187, & 5 < E_O \le 33 \\ 0.179, & E_O > 33 \end{cases} \quad \textbf{(5-29)}$$

Tomiyama's (1998) formulation leads to better prediction of gas void fraction profiles than Antal's (1991) model. However, its biggest disadvantage is that it can only be used in pipe flow because of the use of pipe diameter as a characteristic length scale. Frank (2005) extended the Tomiyama's correlation to any geometry by developing a geometry independent version of the wall lubrication force coefficient, as given in equation 5-30.

$$C_{WL} = C_{W3}(E_O)\ maximum\left(0, \frac{1}{C_{WD}}\left(\frac{1-\frac{Y_w}{C_{WC}d_B}}{Y_w\left(\frac{Y_w}{C_{WC}d_B}\right)^{p_w-1}}\right)\right) \quad \textbf{(5-30)}$$

where C_{W3} is determined from equation 5-29. C_{WC} is the cut-off coefficient which when multiplied by bubble diameter gives the distance from the wall over which wall lubrication force is active. C_{WD} is the damping coefficient which controls magnitude of the wall forces and p_w is a power law constant. During simulations, as per the suggestion of Frank (2005), C_{WC}, C_{WD} and p_w were set to 10.0, 6.8 and 1.7, respectively.

5.3.4 Virtual Mass Force

An accelerating fluid particle tends to accelerate surrounding fluid. Hence, a part of kinetic energy of the accelerating fluid particle will be used to accelerate the surrounding fluid, which will be experienced as a drag force on the fluid particle. This resistive force on the fluid particle is known as the virtual mass force and given by equation 5-31 (Drew et al., 1979 and Drew and Lahey, 1987).

$$\vec{M}_L^{VM} = C_{VM}\alpha_G\rho_L\left(\frac{D_G\vec{U}_G}{Dt} - \frac{D_L\vec{U}_L}{Dt}\right) \quad \textbf{(5-31)}$$

where C_{VM} is the virtual mass coefficient, currently taken to be 0.5. $\frac{D_G}{Dt}$ and $\frac{D_L}{Dt}$ represent material derivatives with respect to gas and liquid phase, respectively.

5.3.5 Turbulent Dispersion Force

Turbulent dispersion force is used to account for dispersion of gas phase by turbulent eddies. In this work Favre Averaged Drag Model proposed by Burns et al. (2004) was used. Burns et al. (2004) obtained turbulent dispersion force by time averaging of the fluctuating component of the interphase drag force.

$$\vec{M}_L^{TD} = C_D C_{TD} \frac{\nu_{tL}}{\sigma_{\alpha L}} \left(\frac{\nabla \alpha_G}{\alpha_G} - \frac{\nabla \alpha_L}{\alpha_L} \right) \quad \textbf{(5-32)}$$

where C_D is the drag force coefficient and C_{TD} is the turbulent dispersion force coefficient which is taken to be 1. ν_{tL} is the kinematic eddy viscosity of liquid phase and $\sigma_{\alpha L}$ is the Turbulent Schmidt Number for liquid phase volume fraction, taken to be 0.9 in the present work. Since, $\alpha_G + \alpha_L = 1$, therefore equation 5-32 can also be written as

$$\vec{M}_L^{TD} = C_D C_{TD} \frac{\nu_{tL}}{\sigma_{\alpha L}} \left(\frac{1}{\alpha_G} + \frac{1}{\alpha_L} \right) \nabla \alpha_G \quad \textbf{(5-33)}$$

5.4 Turbulence Modelling

Liquid turbulence was modelled by the Shear Stress Transport model while a zero equation turbulence model was used for air phase.

5.4.1 Liquid Phase Turbulence Modelling

Liquid turbulence was modelled by the Shear Stress Transport model which has been extended to multiphase flow. Shear Stress Transport model was developed by Menter (1994). It has two key improvements over conventional two equation turbulence models. First, it fuses the $k - \varepsilon$ and $k - \omega$ models in such a way that $k - \omega$ turbulence model is used in the near wall region while $k - \varepsilon$ model is used in the free shear layers. Second, it utilizes a better definition of eddy viscosity by accounting the transport of the principal turbulent shear stresses.

Main idea behind fusing the two models is that the $k-\omega$ model performs superior in the logarithmic region of the boundary layer for flows involving adverse pressure gradients. However, it suffers from free stream dependency in the free shear layers or wake region. Menter (1994) showed that reducing the free stream values of ω_f by four orders of magnitude than earlier value (while maintaining same value of free stream eddy viscosity) resulted in 100% change in eddy viscosity for flat plate zero pressure gradient boundary layer computation. Therefore, in free shear layer region the $k-\varepsilon$ model which does not suffer from free stream dependency is favoured over the $k-\omega$ model. To achieve this improvement the conventional $k-\varepsilon$ model is first transformed to a $k-\omega$ model. It is then multiplied by $1-F_1$ and added to the original $k-\omega$ model multiplied by F_1, where F_1 is the blending function. F_1 is formulated in such a way that it is 1 in the boundary sub layer, logarithmic layer and gradually achieves a zero value in the free shear layer region.

5.4.2 Gas Phase Turbulence Modelling

Turbulence modelling of gas phase was accomplished through a zero equation turbulence model. In this model, gas phase eddy viscosity is related to liquid phase dynamic viscosity by following relation (Yeoh, 2010, p.75):

$$\mu_{tG} = \frac{\rho_G}{\rho_L}\frac{\mu_{tL}}{Pr_t} \tag{5-34}$$

where μ_{tL} is the liquid phase dynamic eddy viscosity and μ_{tG} is the gas phase dynamic eddy viscosity. Pr_t is the turbulent Prandtl Number relating the gas phase eddy viscosity with the liquid phase eddy viscosity.

5.4.3 Bubble Induced Turbulence Modelling

Using eddy viscosity hypothesis, eddy viscosity for liquid phase can be written as:

$$\mu_{tL} = C_{\mu}\rho_L \frac{(k_L)^2}{\varepsilon_L} + \mu_{tL}^B \quad \textbf{(5-35)}$$

where C_{μ} is an empirical constant and μ_{tL}^B is the extra bubble induced turbulence term. Sato and Sekoguchi (1975) proposed

$$\mu_{tL}^B = C_{\mu B}\rho_L \alpha_G d_B \left|\vec{U}_G - \vec{U}_L\right| \quad \textbf{(5-36)}$$

where $C_{\mu B}$ is an empirical constant, given a value of 0.6. Hence the effective viscosity for liquid phase can be written as

$$\mu_{eff,L} = \mu_{Lam,L} + C_{\mu}\rho_L \frac{(k_L)^2}{\varepsilon_L} + \mu_{tL}^B \quad \textbf{(5-37)}$$

where $\mu_{Lam,L}$ is the dynamic viscosity of the liquid phase.

5.5 Boundary Conditions

Transient two-fluid Euler-Euler CFD simulation was carried out for the test case of 7 mm nozzle diameter (D_N), 100 mm jet length (H_N) and 12.5 LPM water flow rate (also referred as the Test Case). Since, water tank used during experiments is square in shape, therefore only a quarter of water tank was modeled, and symmetry condition was provided on appropriate faces (shown in yellow color in figure 5-2). On free water surface degassing boundary condition was applied, which allowed air to escape to atmosphere (shown in light blue color in figure 5-2). Air entrainment modeling at the plunging point by a turbulent liquid jet requires prohibitively expensive computational resources. Hence, an empirical correlation of gas entrainment rate developed by Ohkawa et al. (1986) has been utilized as a boundary condition at the plunging point.

Figure 5.3 shows air entrainment phenomenon at the impact point. Evans et al. (1996) showed that gas entrainment by a plunging liquid jet consists of two components, 1) entrainment by an annular film of gas present around the jet which is pulled in to the liquid by the downward moving liquid jet, 2) gas entrainment in to the rough liquid jet itself, before it plunges in to the liquid pool.

This leads to an enlargement of jet diameter. However, in our experiments flow was fully developed at the nozzle exit and jet diameter was rather found to decrease from the nozzle exit to the impact point. Reduction in jet diameter means that air entrainment by second mechanism (trapped air component) can be neglected. Hence, only filmwise air entrainment occurs.

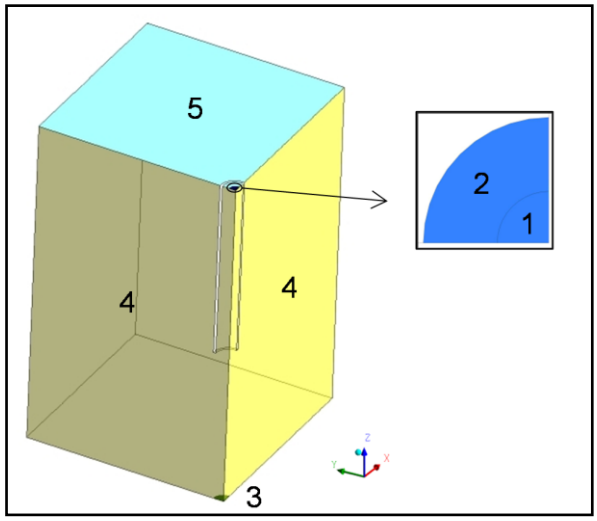

Figure 5-2 The Developed Model

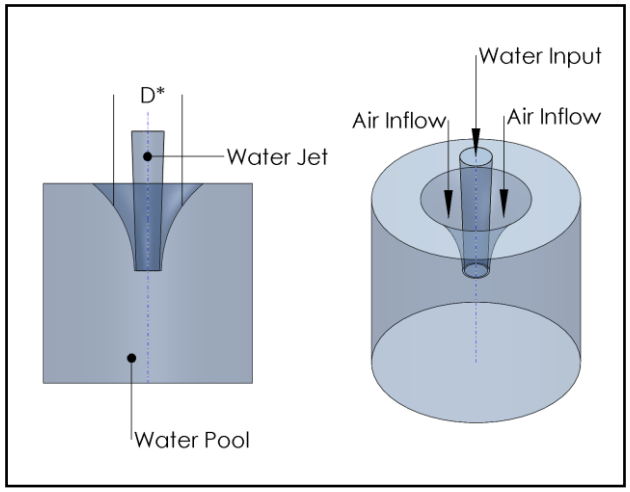

Figure 5-3 Schematics of Air Entrainment

Water jet gained velocity under gravity, as given by equation 5-38.

$$V_J = \sqrt{V_N^2 + 2gH_N} \qquad \textbf{(5-38)}$$

For the water flow rate of 12.5 LPM and the nozzle diameter of 7 mm, V_N is 5.41343 m/s and V_J is found to be 5.59171 m/s. From flow continuity, jet diameter at the impingement point (D_J) is calculated to be 0.0069 m, by equation 5-39.

$$D_J = \sqrt{\frac{4}{\pi}\frac{12.5 \times 10^{-3}}{60}\frac{1}{V_J}} \quad \textbf{(5-39)}$$

Evans et al. (1996) defined D^* as the effective diameter of the film gas entrainment and developed a correlation of $D^* = 2.4D_N$. Hence, for 7 mm nozzle diameter, D^* is 0.0168 m. Using the correlation of air entrainment in a CPLJ system, given by equation 5-40 (Ohkawa et al., 1986 and Bin,1993), air entrainment rate Q_a is calculated to be 4.25501×10^{-4} m^3/s.

$$Q_a = 0.968\left(V_J^3 D_N^2\right)^{0.8}\left(\frac{D_N}{D_C}\right)^{1.3}\left(\frac{H_C}{D_C}\right)^{-1.0} \quad \textbf{(5-40)}$$

Hence, air velocity in air inflow region (V_a) is calculated to be 2.309 m/s, equation 5-41. Input water flow rate of 12.5 LPM to the tank is same as the exit water flow rate from the nozzle of 25.4 mm provide at the bottom of the tank. Hence, water velocity at the outlet nozzle was calculated to be 0.41264 m/s. Boundary conditions have been summarized in Table 5-1.

$$V_a = \frac{Q_a}{\frac{\pi}{4}\left(D^{*2} - D_J^2\right)} \quad \textbf{(5-41)}$$

Table 5-1 Summary of Boundary Conditions

Boundary Condition	**Region**	**Comments**		
		V_{Water} (m/s)	V_{air} (m/s)	α_G
Inlet	1	-5.59171	0.00000	0
Inlet	2	0.00000	-2.30900	1
Outlet	3	-0.41264	0.00000	0
Symmetry	4			
Outlet	5	Degassing Condition		

5.6 Numerical Details

Multiphase CFD simulations were carried out using commercial CFD software ANSYS CFX 12.1. A hexahedral grid of 84630 elements was developed in GAMBIT (grid generation software). The developed grid is shown in figure 5-4. A time step of 0.0005 s was used for transient simulation with a minimum coefficient loop iteration of 1 and a maximum coefficient loop iteration of 10. Convergence criteria were implemented with RMS residual target of 1×10^{-5}. Second Order Backward Euler scheme was used for discretization of transient terms, and the High Resolution scheme was used for discretization of advection terms. Mass transfer between air and water phase was neglected. Air phase was modeled as a polydispersed fluid under the framework of Multiple Size Group (MUSIG) Model. Eight size groups of equal diameters with a minimum and a maximum bubble diameter of 0.0005 m and 0.007 m were used. Selection of minimum and maximum bubble diameters was based on the recommendation of Podila et al. (2007). Bubble coalescence and breakage were incorporated by Prince and Blanch Model (Prince and Blanch, 1990) and Luo and Svendsen Model (Luo and Svendsen, 1996), respectively. Simulations were initialized using two-phase steady state results.

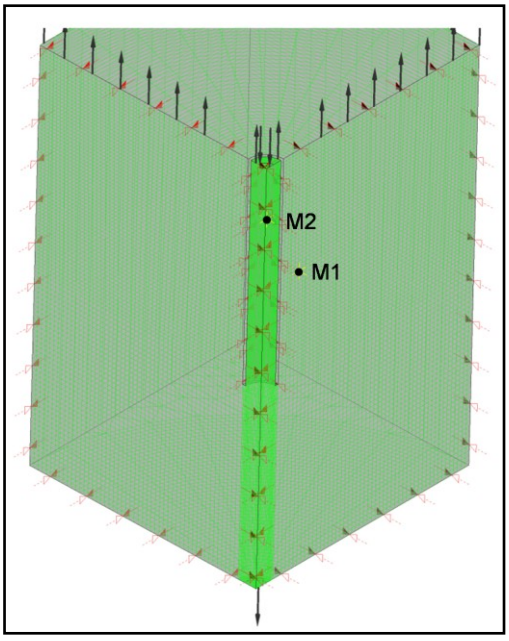

Figure 5-4 Developed Grid

5.6.1 Numerical Uncertainty

It is important to estimate discretization errors present in the simulations. In present work, discretization errors were estimated by the method proposed by Celik (2003) as a part of the ASME Journal of Fluids Engineering editorial policy for estimation of the discretization errors. Three grids of 10,300, 38,500 and 84,630 elements were generated. Grid refinement was done systematically using geometrically similar cells of hexahedral elements. Transient simulations were performed with a time step of 0.0005 s for these three grids.

Representative global grid size for the grids is calculated to be 0.02151 m (h_3) for 10,300 elements, 0.01386 m (h_2) for 38,500 elements, 0.01066 m (h_1) for 84,630 elements by using following formulae:

$$h = \left[\frac{1}{N}\sum_{i=1}^{N}\Delta V_i^E\right]^{\frac{1}{3}} \tag{5-42}$$

where $\sum_{i=1}^{N}\Delta V_i^E$ is the volume occupied by all the elements, and N is the total number of elements. From equation 5-43, it is clear that $h_{coarse}\,/h_{fine} > 1.3$.

$$\frac{h_3}{h_2} = r_{32} = 1.552$$
$$\frac{h_2}{h_1} = r_{21} = 1.300 \tag{5-43}$$

Apparent order, p_u, of the solver method is calculated by the equation 5-44.

$$p_u = \frac{1}{\ln(\mathrm{r}_{21})}\left|\ln\left|\frac{\epsilon_{32}}{\epsilon_{21}}\right| + \mathrm{m}(p_u)\right|$$
$$\mathrm{m}(p_u) = \ln\left(\frac{r_{21}^{p_u} - s_u}{r_{32}^{p_u} - s_u}\right) \tag{5-44}$$
$$s_u = 1.\,\mathrm{sign}\left(\frac{\epsilon_{32}}{\epsilon_{21}}\right)$$

$$\epsilon_{32} = \emptyset_3 - \emptyset_2$$

$$\epsilon_{21} = \emptyset_2 - \emptyset_1$$

where ∅ is the variable to be monitored. We are observing time averaged air velocity at point M1 (0.042, 0, 0.29) and water velocity at the point M2 (0.002, 0.002, 0.36). For calculation of p_u, equation 5-44 is solved using MATLAB. After calculation of p_u extrapolated values of variables are computed by equation 5-45.

$$\emptyset_{\text{ext}}^{21} = \frac{r_{21}^{p_u}\emptyset_1 - \emptyset_2}{r_{21}^{p_u} - 1} \quad \textbf{(5-45)}$$

Finally the following error estimates are calculated

$$\text{e}_{\text{a}}^{21} = \left|\frac{\emptyset_1 - \emptyset_2}{\emptyset_1}\right| \quad \textbf{(5-46)}$$

$$\text{e}_{\text{ext}}^{21} = \left|\frac{\emptyset_{\text{ext}}^{21} - \emptyset_1}{\emptyset_{\text{ext}}^{21}}\right| \quad \textbf{(5-47)}$$

$$\text{GCI}_{\text{fine}}^{21} = \frac{1.25\text{e}_{\text{a}}^{21}}{r_{21}^{p_u} - 1} \quad \textbf{(5-48)}$$

where e_{a}^{21} is approximate relative error and $\text{e}_{\text{ext}}^{21}$ is extrapolated relative error. $\text{GCI}_{\text{fine}}^{21}$ is the fine grid convergence index. Results for above calculations are presented in Table 5-2.

Table 5-2 Results for Discretization Error

	Water Velocity at Point M2	**Air Velocity at Point M1**
N_1,N_2,N_3	10,300, 38,500, 84,630	10,300, 38,500, 84,630
r_{21}	1.300	1.300
r_{32}	1.552	1.552
$\emptyset_1$	5.21978 m/s	0.48344 m/s
$\emptyset_2$	5.34032 m/s	0.45965 m/s
$\emptyset_3$	5.13500 m/s	0.46940 m/s
p_u	1.429	9.7462
$\emptyset_{\text{ext}}^{21}$	4.95478 m/s	0.48544 m/s
e_{a}^{21}	2.30%	4.92%

e_{ext}^{21}	5.35%	0.41%
GCI_{fine}^{21}	6.32%	0.52%

Both the above cases are examples of oscillatory convergence as $\frac{\epsilon_{32}}{\epsilon_{21}} < 0$. On an average, discretization errors were found in the range of 0-8%. Results can be improved with an even finer grid. Given the fact that four to five weeks of time was required in obtaining results with 84,630 elements, simulation with finer grid was not attempted due to lack of time and computational resources.

Effect of time step size was analyzed by performing simulations with a time step of 0.0005 s and 0.001 s for the grid of 84,630 elements. Result of the time averaged air volume fraction is being presented below for both the cases, figure 5-5.

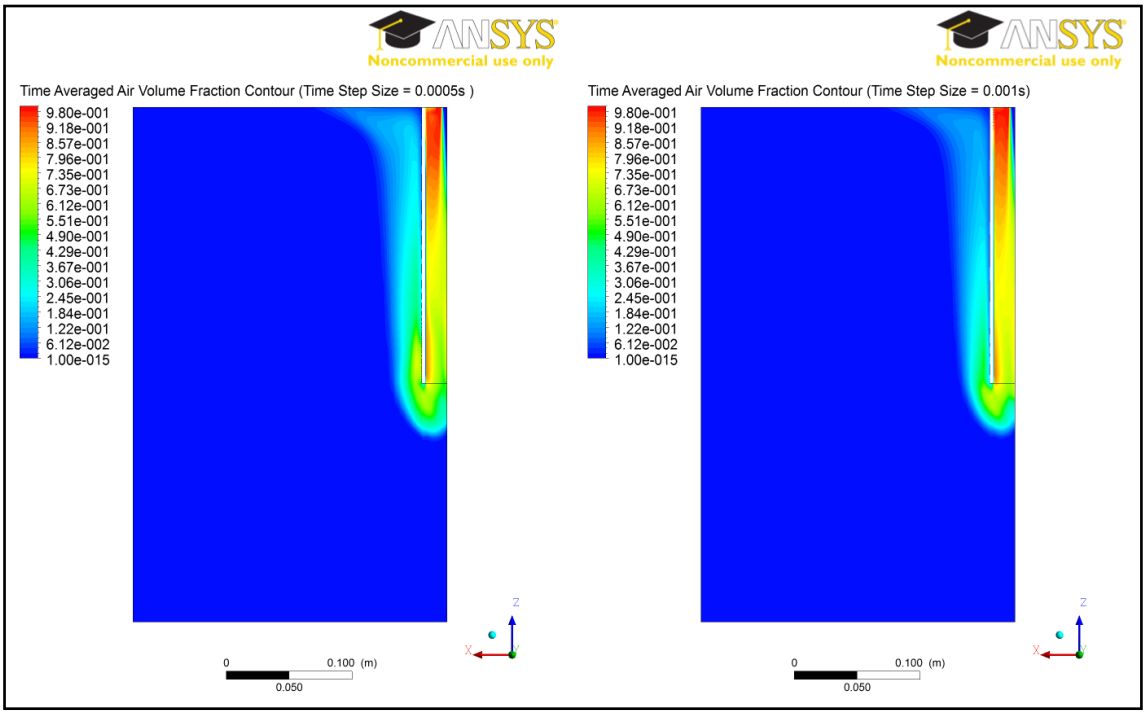

Figure 5-5 Time averaged air volume fraction for the time step of 0.0005 s and 0.001 s.

It can be observed that void fraction profiles are very close to each other for both the cases. However, to maintain accuracy time step of 0.0005 s was adopted in the present study.

5.7 Results and Discussion

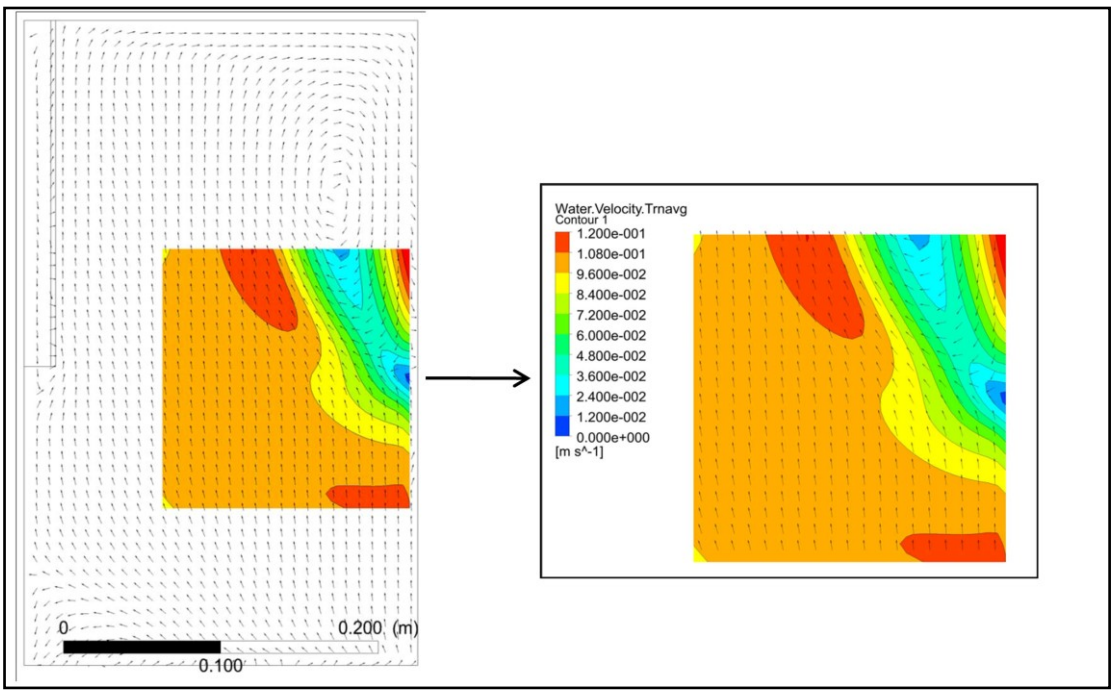

Figure 5-6 CFD result of time averaged water velocity map in PIV area of investigation

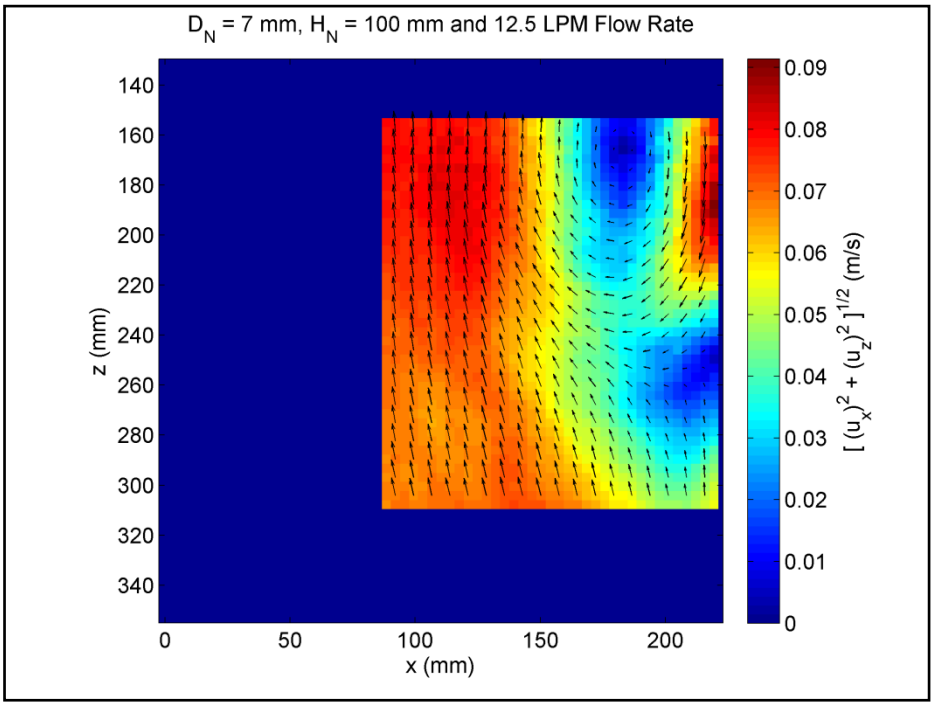

Figure 5-7 Ensemble averaged water velocity field for 7 mm D_N, 100 mm H_N and 12.5 LPM water flow rate

Starting from steady state results, transient results stabilized to a quasi steady state. Figure 5-6 shows time averaged water velocity flow map from CFD computation corresponding to the PIV area of investigation. It can be observed that close to the bubble plume, water is entrained in the plume and lifted upwards. At the free water surface, lifted water turns towards the tank wall and returns in downward direction close to the wall, resulting in a large scale circulatory feature. Figure 5-7 shows water velocity field from PIV Experiments. Flow structures in CFD and PIV results are similar. However CFD velocity values are slightly higher than PIV results.

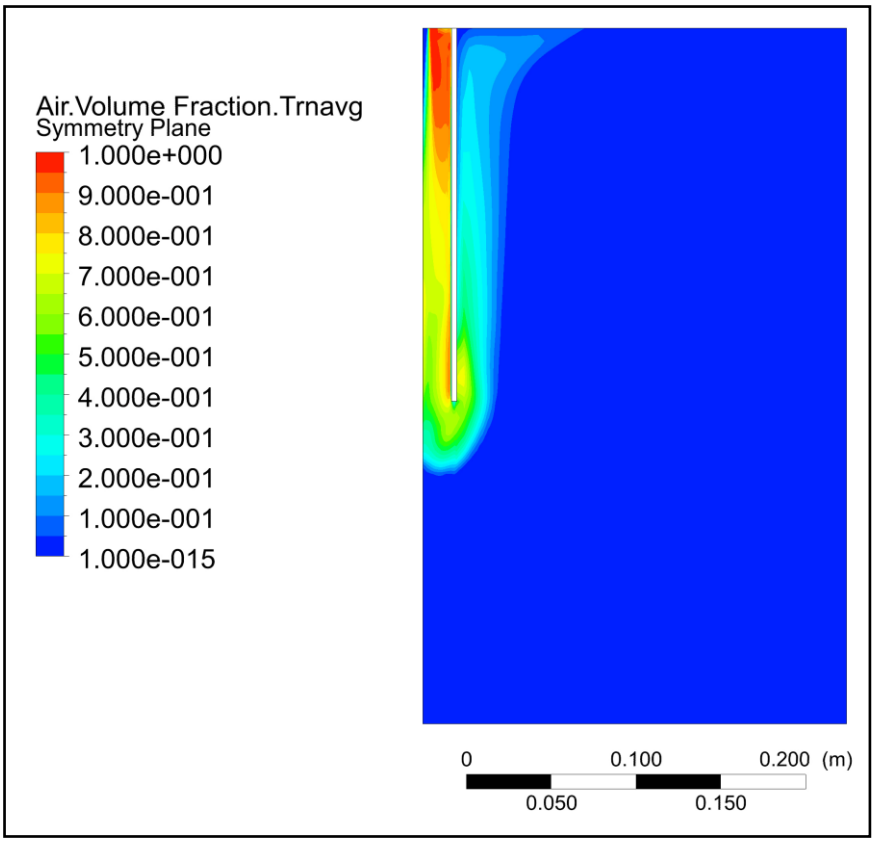

Figure 5-8 Time Averaged Air Volume Fraction

Figure 5-8 shows contours of time averaged air volume fraction in the plane of symmetry which is also the plane of investigation for PIV experiments. Figure 5-8 clearly shows dispersion of entrained air in the water tank. Outer contour of air volume fraction can be used to define outer boundary of bubble plume for comparison with experiments. Hence, an isoline of 1% air volume fraction is

generated and compared with ensemble averaged bubble plume profile from high speed camera experiments, as shown in figure 5-9. CFD results are in agreement with experimentally determined plume boundary with a maximum to minimum error of 10 mm to less than 5 mm, respectively. At x = 0, time averaged depth of plume was experimentally determined to be 59.2 mm from the end of the downcomer tube, while from CFD results it was found to be 42 mm.

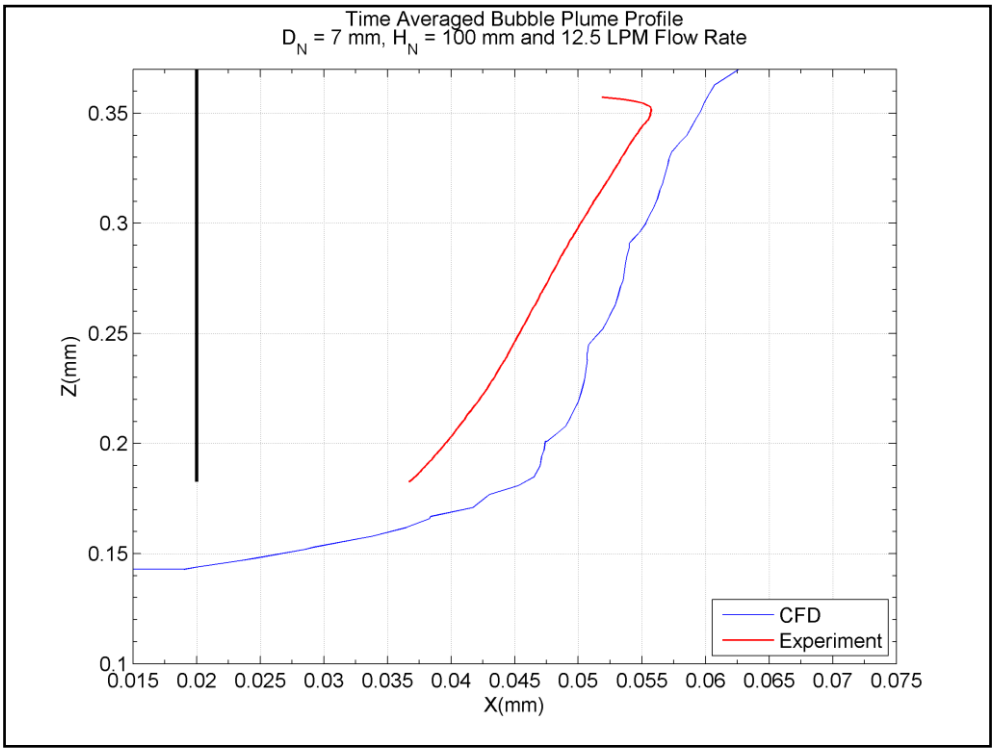

Figure 5-9 Experimental and numerical results of bubble plume boundary

In figure 5-8, close to the point of impingement air volume fraction is very high (greater than 0.9). Its value decreases as air is dispersed down the downcomer tube into the water tank. It can be deduced that water jet plunges some distance in the downcomer in air space before it encounters water. It means that free water surface in the downcomer tube is located below the free water surface in the water tank. During experiments, bubble flow around impingement point at the test condition of 7 mm D_N, 100 mm H_N and 12.5 LPM water flow rate was recorded by the high speed camera. Around 2000 image frames were recorded. Figure 5-10 shows one such high speed photograph. It clearly shows that water

level inside the downcomer is lower than the water tank. In order to quantitatively analyze depth of the air space in the downcomer tube, intensity values in these 2000 frames were averaged. Figure 5-11 shows cropped averaged image of the downcomer tube. In this image less bright region (low intensity values) belongs to air space, while bottom bright region is water. Even though an exact estimate of the height of the air space cannot be drawn based on the intensity averaging process, yet it can be estimated that air space varies between $8.6D_N$ to $10.7D_N$ from the top of the downcomer.

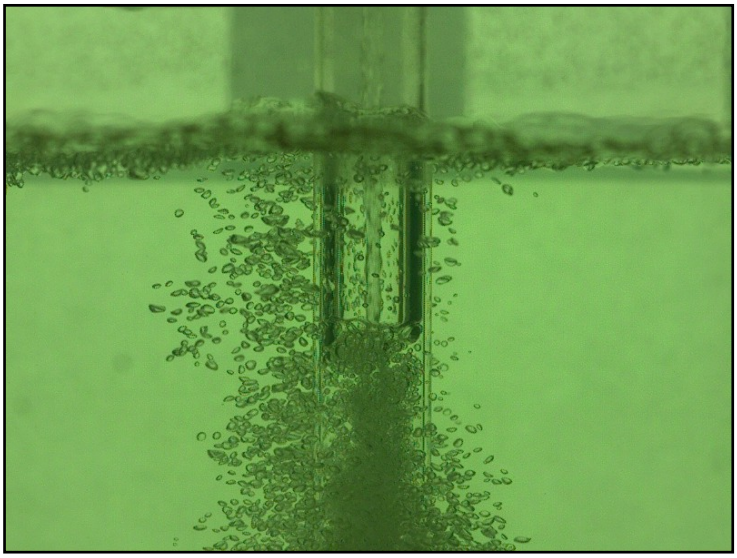

Figure 5-10 A high speed camera photograph at the impingement point

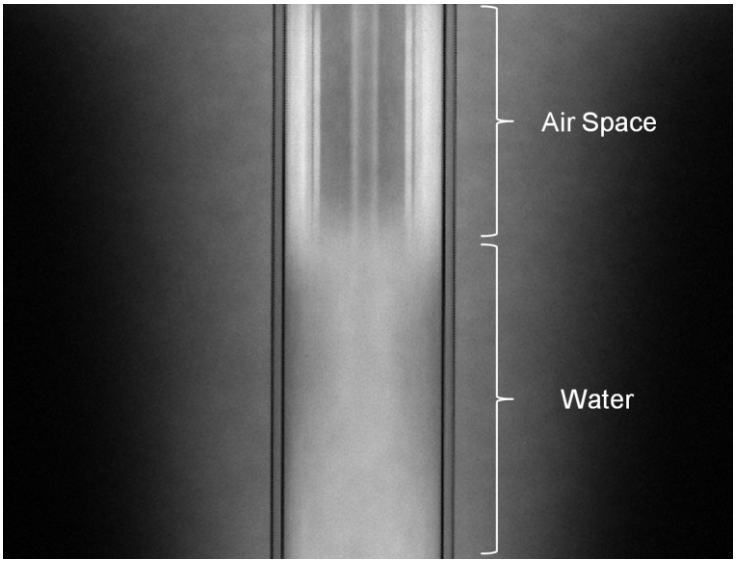

Figure 5-11 Intensity averaged image of the downcomer tube

From the intensity averaged image, air-water flow is estimated to achieve uniform flow condition between $15.7D_N$ to $18.6D_N$ from the top of the downcomer. Assuming that flow space greater than 90% air volume fraction can be termed air space. From the CFD result of time averaged air volume fraction profile, depth of air space in downcomer tube is estimated to be $8.6D_N$. Air volume fraction profile was found to be uniformly developed over more than 90% downcomer cross section after 120 mm from the top of the downcomer. Hence, air-water flow is expected to achieve a uniform flow condition at the depth of $17.1D_N$. Both the above results are in the range of experimental observations, which validates the CFD model.

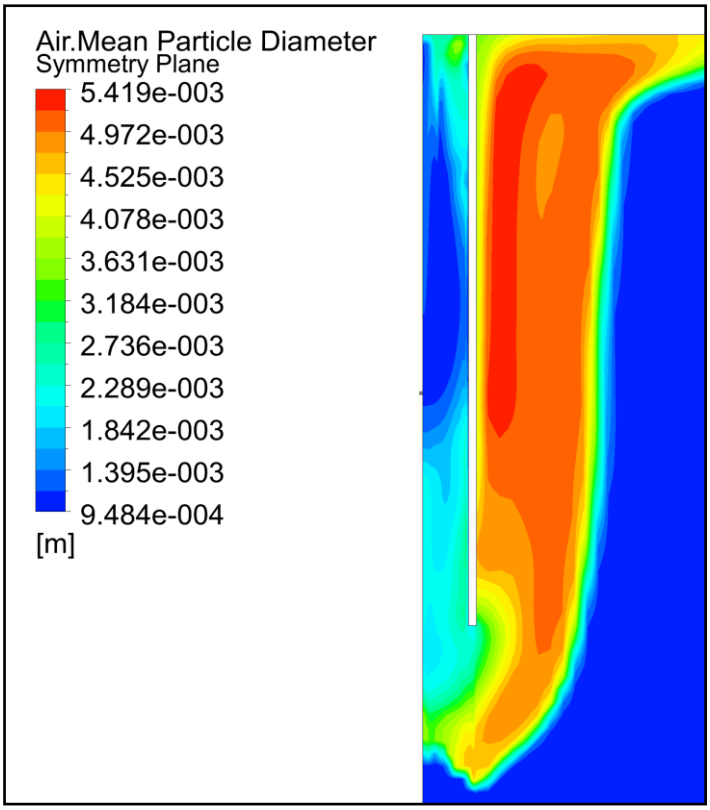

Figure 5-12 Contours of air mean bubble diameter

Figure 5-12 shows contours of air mean particle diameter. Core of the plume around the downcomer is marked by presence of large diameter bubbles (5.4 mm to 4.5 mm), while in outer region of the plume, bubbles of smaller diameter are present (1.4 mm to 4 mm). Minimum bubble diameter was found to be 0.9484 mm. In order to validate this observation, above mentioned recording of

2000 frames was image processed for computation of equivalent bubble diameter. Most of the bubbles are part of the plume and overlapping each other. However, in every frame some bubbles are dispersed enough around the plume that they can be detected individually. Hence, 2000 frames were image processed using MATLAB by a method developed by Danciu et al. (2009). In this method, at first projection areas of the bubbles were measured. Subsequently, bubbles were approximated by circles having same area as that of the measured projection. Diameter of the circle is known as the equivalent bubble diameter. Figure 5-13 shows detected bubbles in one frame. Here, a circle of equivalent bubble diameter was drawn at the geometric centroid of each detected bubble. In this manner diameter of bubbles were measured for all 2000 frames. Figure 5-14 shows the histogram of the bubble diameters. It can be observed that most of the bubbles around the plume are in the range of 1 mm to 4.2 mm with the highest peak of histogram at 2.3 mm and second highest at 2.6 mm. It validates the CFD results, where also smaller diameter bubbles (1.4 mm to 4 mm) were found to exist in the outer regions of the plume.

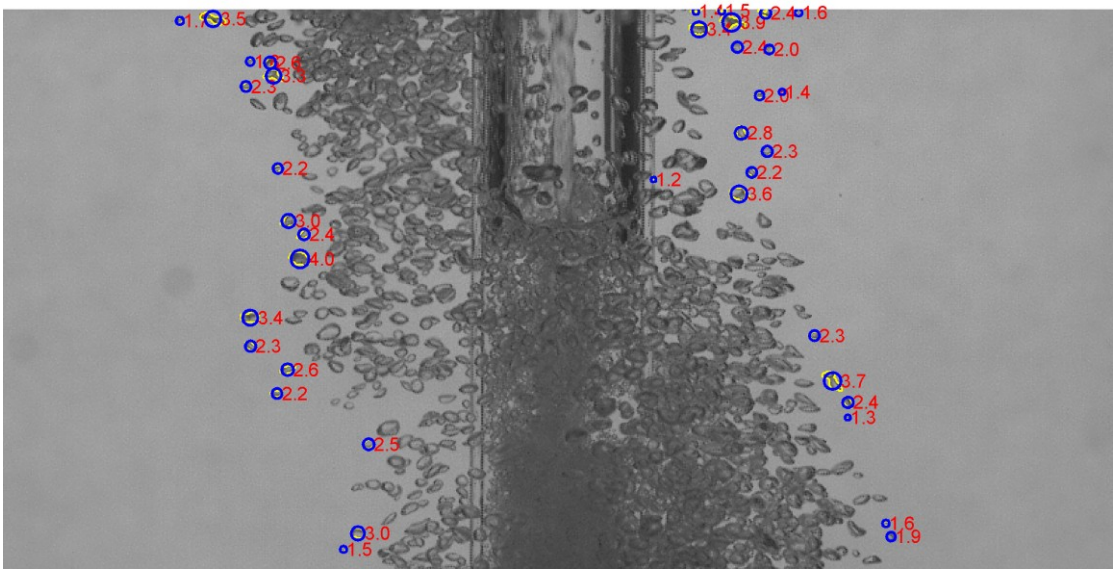

Figure 5-13 Bubbles approximated by circles of equivalent diameter

In conclusion, it can be said that even though CFD results are not exactly same as experimental observations, they are still in agreement with each other. Given the complexity of the flow and various assumptions involved in multiphase flow

modeling, such errors are expected (Krepper et al., 2011). Following improvements are expected to yield more accurate CFD results:

- In present work, a homogeneous MUSIG algorithm was used, which assumes that air bubbles of different diameters at any point share same velocity field. An inhomogeneous MUSIG approach obviates this assumption and produces significantly improved results for air volume fraction profile. Krepper et al. (2008) have already demonstrated that non drag forces which control the air volume fraction profiles are calculated more accurately with the inhomogeneous MUSIG model. However, being computationally expensive it was not tried in this work.

- In MUSIG model, bubble coalescence and breakage were incorporated by Prince and Blanch Model, and Luo and Svendsen Model, respectively. The coalescence and breakage kernels affect bubble size distribution, which in turn affects flow hydrodynamics. Podila et al. (2007) analyzed various breakage and coalescence models. He showed that Prince and Blanch Model, and Luo and Svendsen Model are needed to be improved case by case through user adjustable terms for improved prediction of void fraction distribution. In present study, it would have required transient simulations for many cases, which was beyond the time duration of the present work. So default value of coefficients suggested by Prince and Blanch, and Luo and Svendsen were used in the present study. In future, better results can be obtained by tuning the user adjustable parameters. For more information, readers are directed to the work of Podila et al. (2007).

- In this work, air entrainment rate correlations proposed by Ohkawa et al. (1986) were utilized. These empirical correlations may contain an error of ±30%. Recently there have been considerable developments in two phase flow instrumentation. Therefore, today more accurate air entrainment rate correlations can be obtained. Improved air entrainment rate correlations would result in better CFD results.

- Surface tension plays an important role in an air-water flow. In current work, tap water was used during experiments, and a standard value of surface tension coefficient (air-water) of 0.072 Nm^{-1} was used during simulations. Given the dependence of the surface tension coefficient on contamination, it will be better to measure the surface tension coefficient of used tap water and then utilize the measured value in CFD analysis.

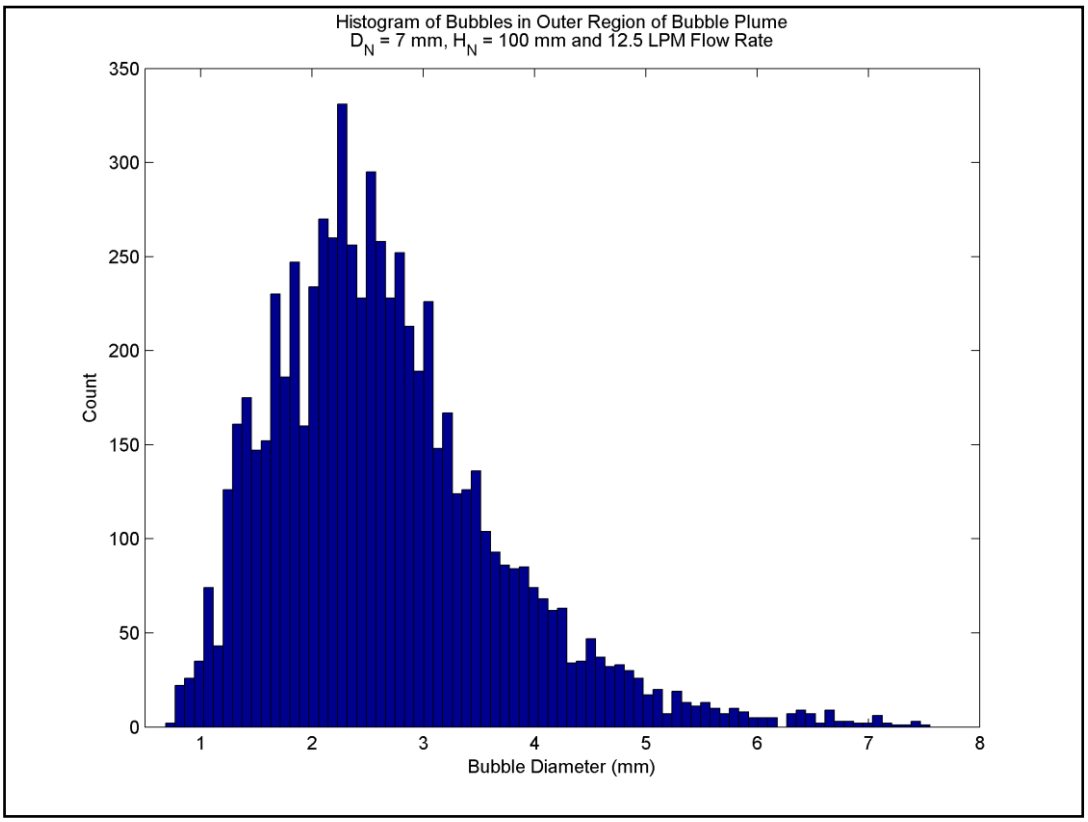

Figure 5-14 Histogram of bubbles in outer region of bubble plume

Figure 5-15 shows a close up view of the streamlines of time averaged air velocity. Figure 5-16 shows water velocity vectors in downcomer tube. It shows that in the mixing zone a strong re-circulatory flow pattern is developed. Air bubbles close to the wall experience lesser drag force than bubbles in core of the flow. Hence these bubbles tend to rise to the surface due to buoyancy forces and pull water in the upwards direction. Some bubbles leave the downcomer tube while some of them are dragged by the water velocity field in the shearing flow close to the impingement point, leading to a re-circulatory air-water flow. Air mass flow rate to atmosphere from the free water surface outside

the downcomer tube was found to be 85% of inlet air mass flow rate. It means that at least 85 % of the inlet air breaks thorough the downcomer tube in to the outer water tank.

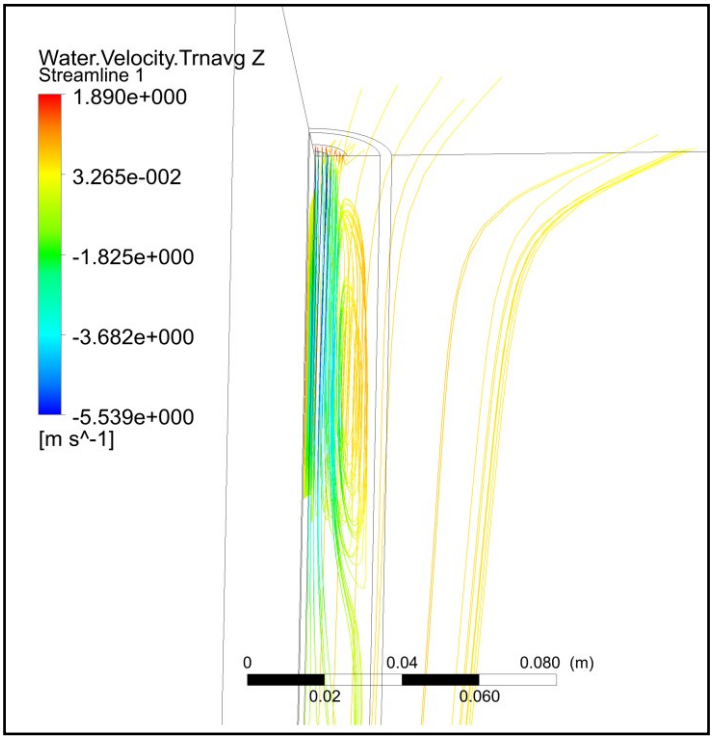

Figure 5-15 Time averaged air velocity streamlines in the downcomer

Present work shows that a CPLJ system can be successfully simulated through CFD. It paves way for more complex CFD simulations, where air-water mass transfer will be switched on, and CPLJ systems will be simulated in their field application format. For example in a stratified lake scenario, effect of more than one CPLJ system will be analyzed on destratification efficiency, or a CPLJ system for waste water treatment will be optimized by maximizing the ratio of air hold up (or air-water mass transfer) with the inlet jet power. Current work serves as a first step towards these goals.

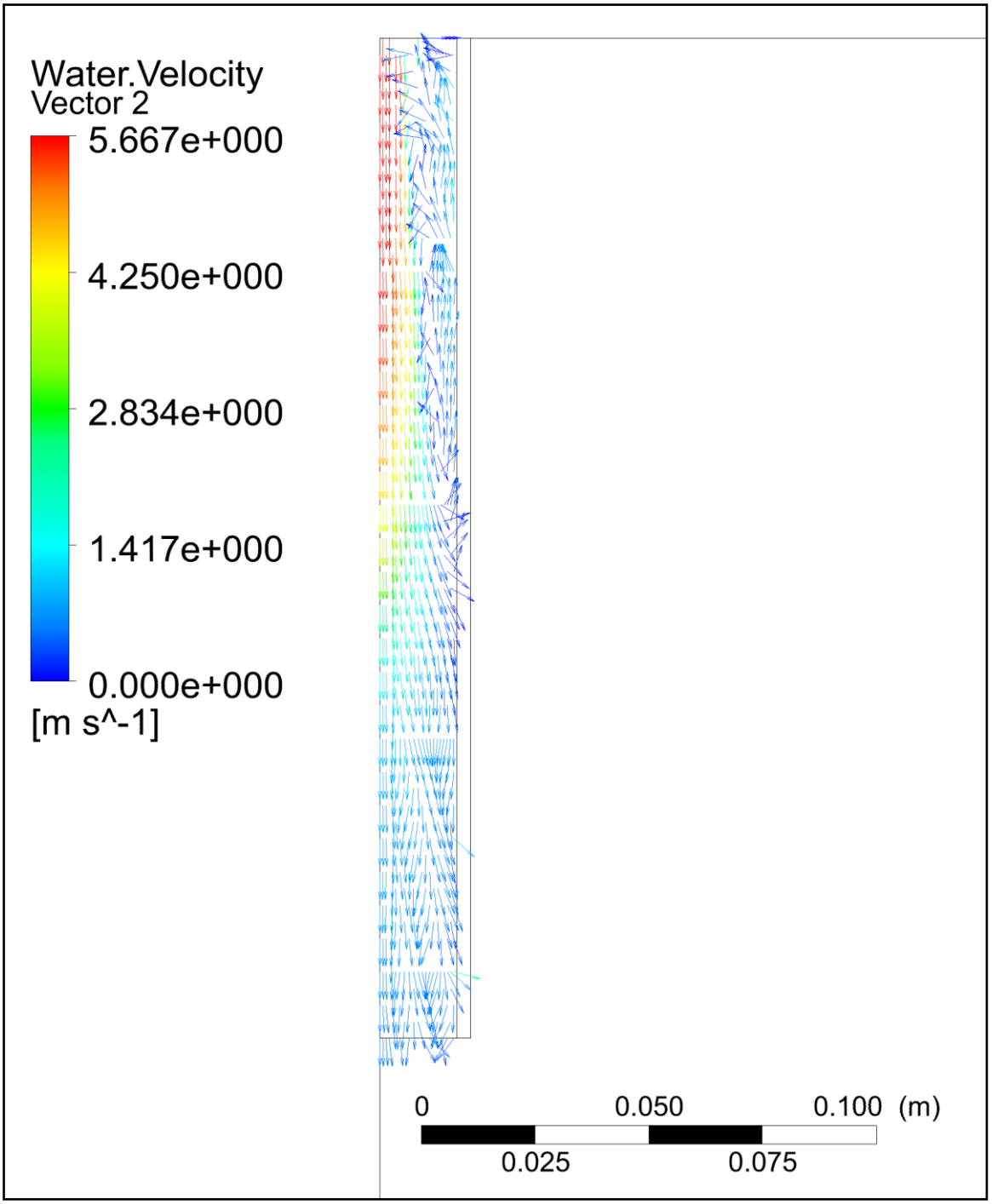

Figure 5-16 Water velocity vector field in the downcomer

6 Conclusion and Recommendations for Future Work

6.1 Conclusions

In present work, a confined plunging liquid jet system was experimentally and numerically analyzed. Impact of change in jet height (H_N), water flow rate and nozzle diameter (D_N) on bubble plume and surrounding flow field was investigated through high speed camera photography and Particle Image Velocimetry (PIV). Image processing programs were developed in MATLAB for segmentation of bubble plume boundaries in high speed camera images. Results from high speed camera experiments showed that:

- Bubble plume extents are only weakly dependent on jet height. A comparison of plume profiles for different jet heights at D_N = 10 mm and 12.5 LPM Water Flow Rate revealed that bubble plume profiles are almost overlapping each other. Same effect was observed for other test cases too.

  Moving beyond the critical flow rate of 7.5 LPM, for those test conditions where plume is distinctly present in the outer pool, plume depth is also found to be unsystematically affected by change in H_N. In fact in many cases results were found to be overlapping.

- Increase in water flow rate leads to wider and deeper bubble plumes. As the inlet water flow rate was increased from 7.5 LPM to 15 LPM, plume boundaries were found to monotonically increase in depth and width for all the test cases.

- Increase in nozzle diameter for same flow rate and jet height reduces bubble plume width. For the water flow rate of 15 LPM, plume extents with 7 mm D_N were found to be approximately 2-3 times, in width of plume extents for 10 mm D_N. Similar trend was observed for other test cases too. A comparison of results of plume depth for 7 mm and 10 mm

D_N showed that beyond 10 LPM, plume depth is significantly higher for 7 mm nozzle.

Due to abrupt changes in optical properties of flow, PIV experiments based on Mie-scattering of laser light were found to be full of noise. Hence, PIV-LIF method was used for water flow field measurement. In this method, fluorescent coated tracer particles and a tuned optical filter ensured that only tracer particles were recorded and noise from bubbles was filtered out. PIV results showed that with increase in water flow rate, water velocity around bubble plume increases in the upward direction. Change in H_N, while maintaining the same flow rate and D_N does not appreciably affect the water flow field.

With increase in nozzle diameter from 7 mm to 10 mm, water velocity field around plume was found to decrease. A comparison of water velocity field for both the nozzles at 150 mm H_N and 15.0 LPM water flow rate revealed that water velocity vectors around bubble plume for 7 mm D_N case are in the range of 0.08 to 0.1 m/s, while for 10 mm D_N case vectors are in the range of 0.07-0.08 m/s.

Based, on the above results smaller nozzle diameter with higher flow rate would lead to faster destratification or aeration.

On numerical front, CFD simulation of CPLJ system was performed for the test case of 7 mm D_N, 100 mm H_N and 12.5 LPM water flow rate, using ANSYS CFX 12.1. Numerical and experimental results were found to be in agreement with each other. CFD results showed that close to the bubble plume, water is entrained in the plume and lifted upwards. At the free water surface, lifted water turns towards the tank wall and returns in downward direction close to the wall, resulting in a large scale circulatory feature. At least 85% of the entrained air was found to breakthrough the downcomer in to the outer water pool. CFD result of plume boundary was found to be in agreement with experimentally determined plume boundary, with a maximum to minimum error of 10 mm to less than 5 mm, respectively. CFD results in conjunction with experimental observations helped to understand the mixing phenomenon at the impingement

point. Air-water flow in downcomer tube was found to attain a uniform flow condition after $17.1D_N$. In author's knowledge, this work is first CFD simulation of bubble plume dispersion in a confined plunging liquid jet system. Moreover, no other study has quantified a CPLJ system using high speed camera photography and PIV technique.

6.2 Recommendations for Future Work

Following recommendations are being given for future work:

- In present work, effect of downcomer diameter and downcomer depth could not be investigated due to lack of time. Hence, their effect on bubble plume extents should be investigated using PIV and high speed camera photography to gain a complete understanding of parameters affecting plume profiles.

- Effect of nozzle diameter, jet height, downcomer diameter, downcomer depth, jet velocity and nozzle geometry on air entrainment rate should be investigated using Wire Mesh Sensors or Optical Tomography Technique. Later, air entrainment rate correlations should be developed from this data. Wire Mesh Sensors, developed at Helmholtz-Zentrum Dresden-Rossendorf (Germany) allow investigation of air-water flow at high spatial and temporal resolution (Prasser et al., 2001, Prasser et al., 2005 and Pietruske and Prasser, 2007). Optical tomography also facilitates high temporal resolution and it is completely non invasive (Schleicher et al., 2008). Air entrainment rate in downcomer tube can be measured relatively non-intrusively and more accurately by the above mentioned techniques than the method used by Ohkawa et al. (1986). Hence, air entrainment rate correlations developed from the experimental data obtained through the wire mesh sensors or optical tomography technique would be more accurate and robust than the work of Ohkawa et al. (1986).

- Moving ahead from present work, CFD simulation of bubble plume dispersion should be performed with improved air entrainment rate correlations developed in the above step. In simulations air-water mass transfer should also be activated, and the inhomogeneous MUSIG model should be utilized for polydispersed air phase modelling. CFD results should be validated against experimental measurements of oxygen mass transfer.

- After validation, CFD model should be extended to analyze destratification and aeration performance in a field application format, where a rectangular grid of uniformly spaced downcomers is used for destratification. CFD results from this study will provide definitive guidance to design engineers of aeration systems. Later, downcomer grid spacing and other CPLJ parameters can be optimized to achieve higher destratification efficiency through CFD analysis.

REFERENCES

Akhtar, M. A., Tadé, M. O. and Pareek, V. K. (2006), "Two-fluid Eulerian simulation of bubble column reactors with distributors", *Journal of Chemical Engineering of Japan,* vol. 39, no. 8, pp. 831-841.

Ali, B. A., Kumar, C. S. and Pushpavanam, S. (2008), "Analysis of liquid circulation in a rectangular tank with a gas source at a corner", *Chemical Engineering Journal,* vol. 144, no. 3, pp. 442-452.

Ansari, S. A., Phillips, N., Stabler, G., Wilkins, P. C., Zbikowski, R. and Knowles, K. (2009), "Experimental investigation of some aspects of insect-like flapping flight aerodynamics for application to micro air vehicles", *Experiments in Fluids,* vol. 46, no. 5, pp. 777-798.

Antal, S. P., Lahey Jr., R. T. and Flaherty, J. E. (1991), "Analysis of phase distribution in fully developed laminar bubbly two-phase flow", *International Journal of Multiphase Flow,* vol. 17, no. 5, pp. 635-652.

Atkinson, B. W., Jameson, G. J., Nguyen, A. V. and Evans, G. M. (2003), "Increasing gas-liquid contacting using a confined plunging liquid jet", *Journal of Chemical Technology and Biotechnology,* vol. 78, no. 2-3, pp. 269-275.

Becker, S., De Bie, H. and Sweeney, J. (1999), "Dynamic flow behaviour in bubble columns", *Chemical Engineering Science,* vol. 54, no. 21, pp. 4929-4935.

Becker, S., Sokolichin, A. and Eigenberger, G. (1994), "Gas-liquid flow in bubble columns and loop reactors: Part II. Comparison of detailed experiments and flow simulations", *Chemical Engineering Science,* vol. 49, no. 24, pp. 5747-5762.

Biń, A. K. (1993), "Gas entrainment by plunging liquid jets", *Chemical Engineering Science,* vol. 48, no. 21, pp. 3585-3630.

Botton, R., Cosserat, D., Poncin, S. and Wild, G. (2009), "A simple gas-liquid mass transfer jet system", *8th World Congress of Chemical Engineering*, Montréal, Canada.

Bravo, H. R., Gulliver, J. S. and Hondzo, M. (2007), "Development of a commercial code-based two-fluid model for bubble plumes", *Environmental Modelling and Software,* vol. 22, no. 4, pp. 536-547.

Bröder, D. and Sommerfeld, M. (2002), "An advanced LIF-PLV system for analysing the hydrodynamics in a laboratory bubble column at higher void fractions", *Experiments in Fluids,* vol. 33, no. 6, pp. 826-837.

Burns, A. D., Frank, T., Hamill, I. and Shi, J. (2004), "The favre averaged drag model for turbulent dispersion in eulerian multi-phase flows", *5th International Conference on Multiphase Flow*, Yokohama, Japan.

Celik, I. B. (2003), "Journal of fluids engineering editorial policy: Procedure for estimation and reporting of discretization error in CFD applications", *Asme Journal of Fluids Engineering*, New York.

Chanson, H., Aoki, S. and Hoque, A. (2006), "Bubble entrainment and dispersion in plunging jet flows: Freshwater vs. seawater", *Journal of Coastal Research,* vol. 22, no. 3, pp. 664-677.

Chanson, H., Aoki, S. and Hoque, A. (2004), "Physical modelling and similitude of air bubble entrainment at vertical circular plunging jets", *Chemical Engineering Science,* vol. 59, no. 4, pp. 747-758.

Chanson, H., Aoki, S. -. and Hoque, A. (2002), "Similitude of air entrainment at vertical circular plunging jets", *American Society of Mechanical Engineers, Fluids Engineering Division (Publication) FED,* Vol. 257, pp. 467.

Chen, P., Duduković, M. P. and Sanyal, J. (2005), "Three-dimensional simulation of bubble column flows with bubble coalescence and breakup", *AICHE Journal,* vol. 51, no. 3, pp. 696-712.

Clift, R., Grace, J.R. and Weber, E.M. (1978), *Bubbles, drops, and particles,* Academic Press, New York ; London.

Cummings, P. D. and Chanson, H. (1999), "An experimental study of individual air bubble entrainment at a planar plunging jet", *Chemical Engineering Research and Design,* vol. 77, no. 2, pp. 159-164.

Danciu, D. V., Da Silva, M. J., Schmidtke, M., Lucas, D. and Hampel, U. (2009), "Experimental investigation on air entrainment below impinging jets by means of video observations and image processing", *WIT Transactions on Engineering Sciences,* Vol. 63, pp. 481.

Deswal, S. and Verma, D. V. S. (2007), "Air-water oxygen transfer with multiple plunging jets", *Water Quality Research Journal of Canada,* vol. 42, no. 4, pp. 295-302.

Drew, D., Cheng, L. and Lahey Jr., R. T. (1979), "The analysis of virtual mass effects in two-phase flow", *International Journal of Multiphase Flow,* vol. 5, no. 4, pp. 233-242.

Drew, D. A. and Lahey Jr., R. T. (1987), "The virtual mass and lift force on a sphere in rotating and straining inviscid flow", *International Journal of Multiphase Flow,* vol. 13, no. 1, pp. 113-121.

Ervine, D. A. and Elsawy, E. M. (1975), "Effect silt a falling nappe on river aeration", *Int Assoc for Hydraul Res, 16th Congr, Proc, Prepr, Fundam Tools To Be Used in Environ Prob,* vol. 3 -Subj, pp. 390-397.

Evans, G. M., Jameson, G. J. and Rielly, C. D. (1996), "Free jet expansion and gas entrainment characteristics of a plunging liquid jet", *Experimental Thermal and Fluid Science,* vol. 12, no. 2, pp. 142-149.

Evans, G. M. and Machniewski, P. M. (1999), "Mass transfer in a confined plunging liquid jet bubble column", *Chemical Engineering Science,* vol. 54, no. 21, pp. 4981-4990.

Frank, T. (2005), "Advances in computational fluid dynamics (CFD) of 3-dimensional gas-liquid multiphase flows", *NAFEMS Seminar: Simulation of Complex Flows (CFD)-Applications and Trends*, Niedernhausen/Wiesbaden, Germany.

Ishii, M. (2006), *Thermo-fluid dynamics of two-phase flow,* Springer, New York ; London.

Krepper, E., Lucas, D., Frank, T., Prasser, H. -. and Zwart, P. J. (2008), "The inhomogeneous MUSIG model for the simulation of polydispersed flows", *Nuclear Engineering and Design,* vol. 238, no. 7, pp. 1690-1702.

Krepper, E., Weiss, F. -., Alt, S., Kratzsch, A., Renger, S. and Kästner, W. (2011), "Influence of air entrainment on the liquid flow field caused by a plunging jet and consequences for fibre deposition", *Nuclear Engineering and Design,* vol. 241, no. 4, pp. 1047-1054.

LaVision GmbH (2006), "Fluorescent Seeding Particles Specification Sheet", *LaVision GmbH*, Germany.

LaVision GmbH (2009), "Fluorescence Edge Filter Specification Sheet", *LaVision GmbH*, Germany.

LaVision GmbH (2002), "DaVis FlowMaster Software Manual for DaVis 6.2", *LaVision GmbH*, Germany, p. 54.

Lin, T. J. and Donnelly, H. G. (1966), "Gas bubble entrainment by plunging laminar liquid jets", *AICHE Journal,* vol. 12, no. 3, pp. 563-571.

Lindken, R. and Merzkirch, W. (2002), "A novel PIV technique for measurements in multiphase flows and its application to two-phase bubbly flows", *Experiments in Fluids,* vol. 33, no. 6, pp. 814-825.

Lucas, D., Krepper, E. and Prasser, H. -. (2007), "Use of models for lift, wall and turbulent dispersion forces acting on bubbles for poly-disperse flows", *Chemical Engineering Science,* vol. 62, no. 15, pp. 4146-4157.

Luo, H. and Svendsen, H. F. (1996), "Theoretical Model for Drop and Bubble Breakup in Turbulent Dispersions", *AICHE Journal,* vol. 42, no. 5, pp. 1225-1233.

Ma, J., Oberai, A. A., Drew, D. A., Lahey Jr., R. T. and Moraga, F. J. (2010), "A quantitative sub-grid air entrainment model for bubbly flows - plunging jets", *Computers and Fluids,* vol. 39, no. 1, pp. 77-86.

Majumder, S. K., Kundu, G. and Mukherjee, D. (2005), "Mixing mechanism in a modified co-current downflow bubble column", *Chemical Engineering Journal,* vol. 112, no. 1-3, pp. 45-55.

Menter, F. R. (1994), "Two-equation eddy-viscosity turbulence models for engineering applications", *AIAA Journal,* vol. 32, no. 8, pp. 1598-1605.

Michele, J. and Michele, V. (2002), "The free jet as a means to improve water quality: Destratification and oxygen enrichment", *Limnologica,* vol. 32, no. 4, pp. 329-337.

Moraga, F. J., Carrica, P. M., Drew, D. A. and Lahey Jr., R. T. (2008), "A sub-grid air entrainment model for breaking bow waves and naval surface ships", *Computers and Fluids,* vol. 37, no. 3, pp. 281-298.

Oğuz, H. N. (1998), "The role of surface disturbances in the entrainment of bubbles by a liquid jet", *Journal of Fluid Mechanics,* vol. 372, pp. 189-212.

Ohkawa, A., Kusabiraki, D., Kawai, Y., Sakai, N. and Endoh, K. (1986), "Some flow characteristics of a vertical liquid jet system having downcomers", *Chemical Engineering Science,* vol. 41, no. 9, pp. 2347-2361.

Pietruske, H. and Prasser, H. -. (2007), "Wire-mesh sensors for high-resolving two-phase flow studies at high pressures and temperatures", *Flow Measurement and Instrumentation,* vol. 18, no. 2, pp. 87-94.

Podila, K., Al Taweel, A. M., Koksal, M., Troshko, A. and Gupta, Y. P. (2007), "CFD simulation of gas-liquid contacting in tubular reactors", *Chemical Engineering Science,* vol. 62, no. 24, pp. 7151-7162.

Prasser, H. -., Beyer, M., Frank, T., Al Issa, S., Carl, H., Pietruske, H. and Schütz, P. (2008), "Gas-liquid flow around an obstacle in a vertical pipe", *Nuclear Engineering and Design,* vol. 238, no. 7, pp. 1802-1819.

Prasser, H. -., Misawa, M. and Tiseanu, I. (2005), "Comparison between wire-mesh sensor and ultra-fast X-ray tomograph for an air-water flow in a vertical pipe", *Flow Measurement and Instrumentation,* vol. 16, no. 2-3, pp. 73-83.

Prasser, H. -., Scholz, D. and Zippe, C. (2001), "Bubble size measurement using wire-mesh sensors", *Flow Measurement and Instrumentation,* vol. 12, no. 4, pp. 299-312.

Prince, M. J. and Blanch, H. W. (1990), "Bubble coalescence and break-up in air-sparged bubble columns", *AICHE Journal,* vol. 36, no. 10, pp. 1485-1499.

Raffel, M. and SpringerLink, (2007), *Particle image velocimetry*, 2nd ed., Springer, Heidelberg ; New York.

Rampure, M. R., Kulkarni, A. A. and Ranade, V. V. (2007), "Hydrodynamics of bubble column reactors at high gas velocity: Experiments and computational fluid dynamics CFD simulations", *Industrial and Engineering Chemistry Research,* vol. 46, no. 25, pp. 8431-8447.

Ranade, V. V. and Tayalia, Y. (2001), "Modelling of fluid dynamics and mixing in shallow bubble column reactors: Influence of sparger design", *Chemical Engineering Science,* vol. 56, no. 4, pp. 1667-1675.

Sanyal, J., Vásquez, S., Roy, S. and Dudukovic, M. P. (1999), "Numerical simulation of gas-liquid dynamics in cylindrical bubble column reactors", *Chemical Engineering Science,* vol. 54, no. 21, pp. 5071-5083.

Sato, Y. and Sekoguchi, K. (1975), "Liquid velocity distribution in two-phase bubble flow", *International Journal of Multiphase Flow,* vol. 2, no. 1, pp. 79-95.

Schiller, L. and Naumann, Z. (1935), "A drag coefficient correlation", *Ver. Deutsch. Ing.*, pp. 77–318, Cited in: Ali, B. A., Kumar, C. S. and Pushpavanam, S. (2008), "Analysis of liquid circulation in a rectangular tank with a gas source at a corner", *Chemical Engineering Journal,* vol. 144, no. 3, pp. 442-452.

Schleicher, E., Da Silva, M. J., Thiele, S., Li, A., Wollrab, E. and Hampel, U. (2008), "Design of an optical tomograph for the investigation of single- and two-phase pipe flows", *Measurement Science and Technology,* vol. 19, no. 9.

Schmidtke, M., Danciu, D. and Lucas, D. (2009), "Air entrainment by impinging jets: Experimental identification of the key phenomena and approaches for their simulation in CFD", *International Conference on Nuclear Engineering, Proceedings, ICONE,* Vol. 3, pp. 297.

Sokolichin, A. and Eigenberger, G. (1994), "Gas-liquid flow in bubble columns and loop reactors: Part I. Detailed modelling and numerical simulation", *Chemical Engineering Science,* vol. 49, no. 24, pp. 5735-5746.

Sridhar, G., Ran, B. and Katz, J. (1991), "Implementation of particle image velocimetry to multi-phase flow", .

Taşdemir, T., Öteyaka, B. and Taşdemir, A. (2007), "Air entrainment rate and holdup in the Jameson cell", *Minerals Engineering,* vol. 20, no. 8, pp. 761-765.

Tomiyama, A. (1998), "Struggle with computational bubble dynamics", *Multiphase Science and Technology,* vol. 10, no. 4, pp. 369-405.

Tomiyama, A., Tamai, H., Zun, I. and Hosokawa, S. (2002), "Transverse migration of single bubbles in simple shear flows", *Chemical Engineering Science,* vol. 57, no. 11, pp. 1849-1858.

Van De Sande, E. and Smith, J. M. (1976), "Jet break-up and air entrainment by low velocity turbulent water jets", *Chemical Engineering Science,* vol. 31, no. 3, pp. 219-224.

Willert, C. E. and Gharib, M. (1991), "Digital particle image velocimetry", *Experiments in Fluids,* vol. 10, no. 4, pp. 181-193.

Yeoh, G. H. (2010), *Computational techniques for multi-phase flows: basics and applications,* Butterworth-Heinemann, Oxford.

Ẑun, I. (1980), "The transverse migration of bubbles influenced by walls in vertical bubbly flow", *International Journal of Multiphase Flow,* vol. 6, no. 6, pp. 583-588.

APPENDICES

Appendix A Ensemble Averaged Water Velocity Field

Ensemble averaged water velocity field for different test cases in Test Matrix 1 and 2 (Table 2-1 and 2-2) is being presented below:

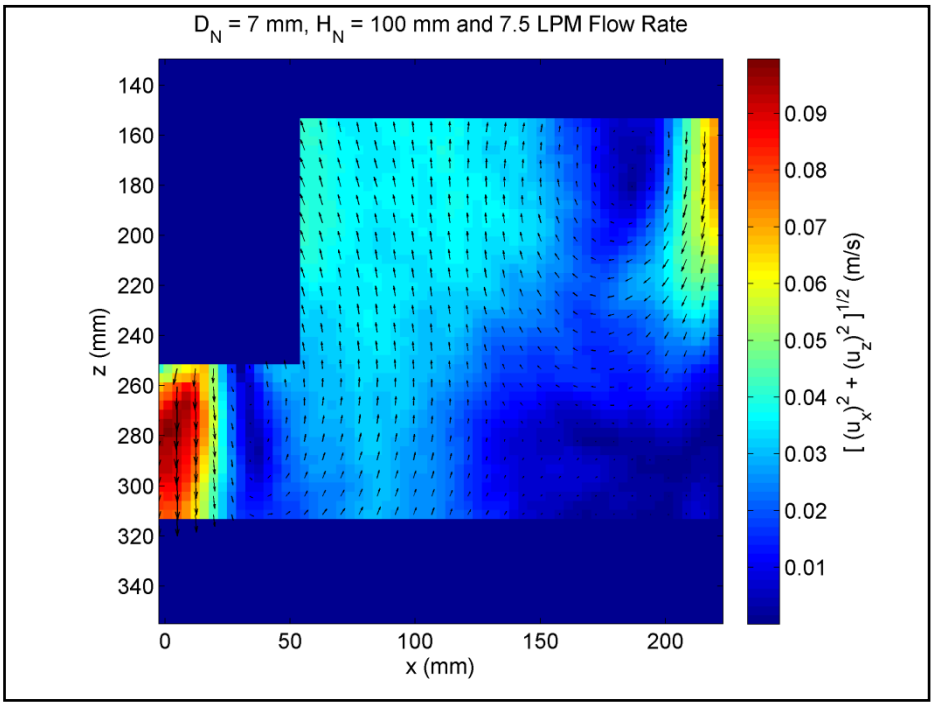

Figure A-1 Water velocity field for 7 mm D_N, 100 mm H_N and 7.5 LPM water flow rate

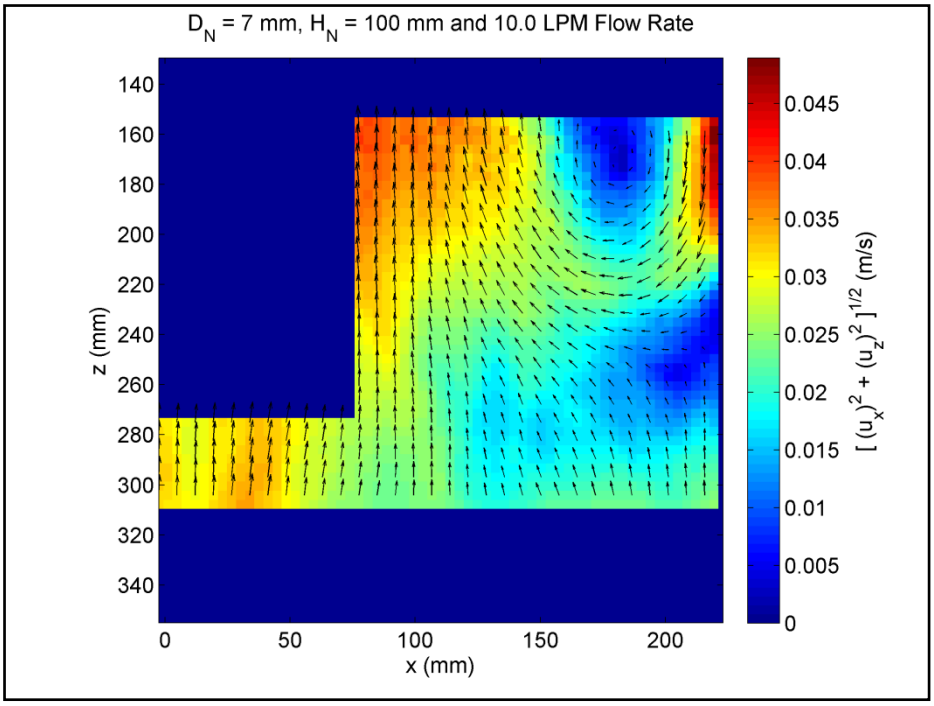

Figure A-2 Water velocity field for 7 mm D_N, 100 mm H_N and 10.0 LPM water flow rate

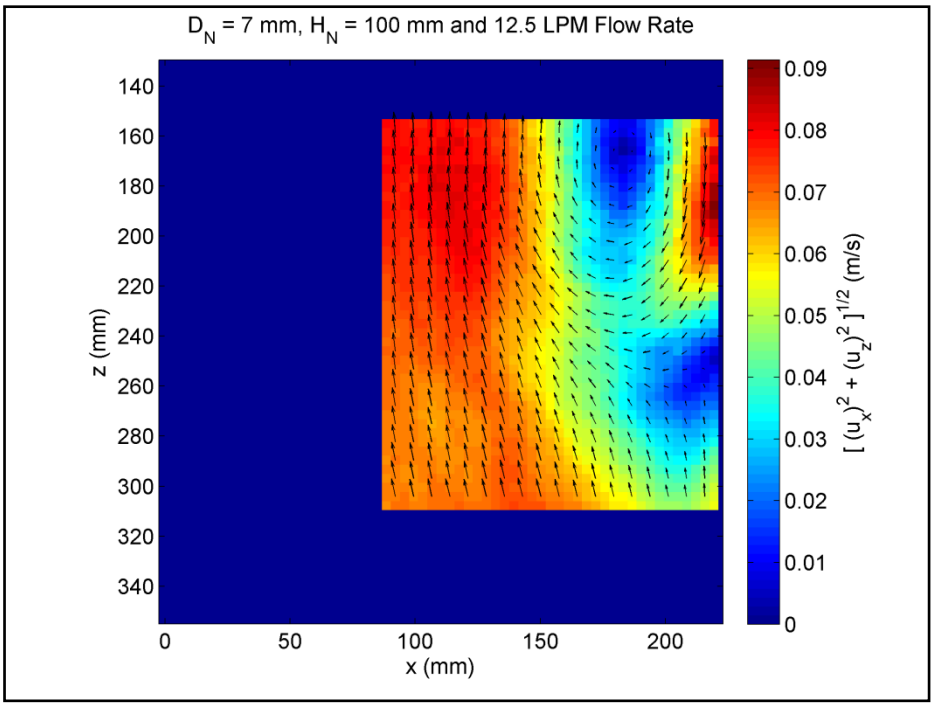

Figure A-3 Water velocity field for 7 mm D_N, 100 mm H_N and 12.5 LPM water flow rate

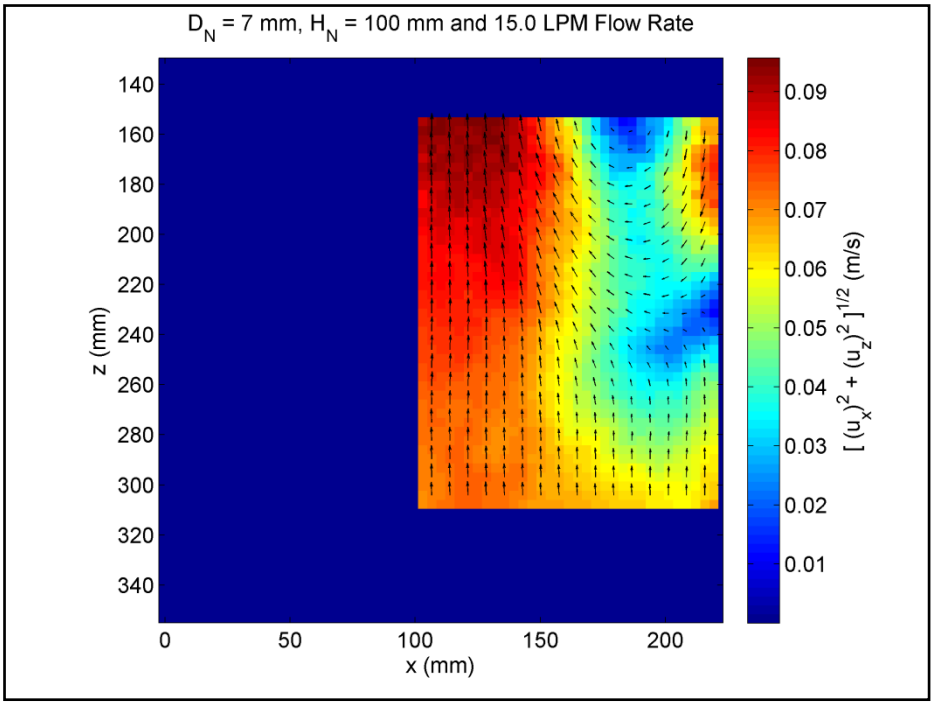

Figure A-4 Water velocity field for 7 mm D_N, 100 mm H_N and 15.0 LPM water flow rate

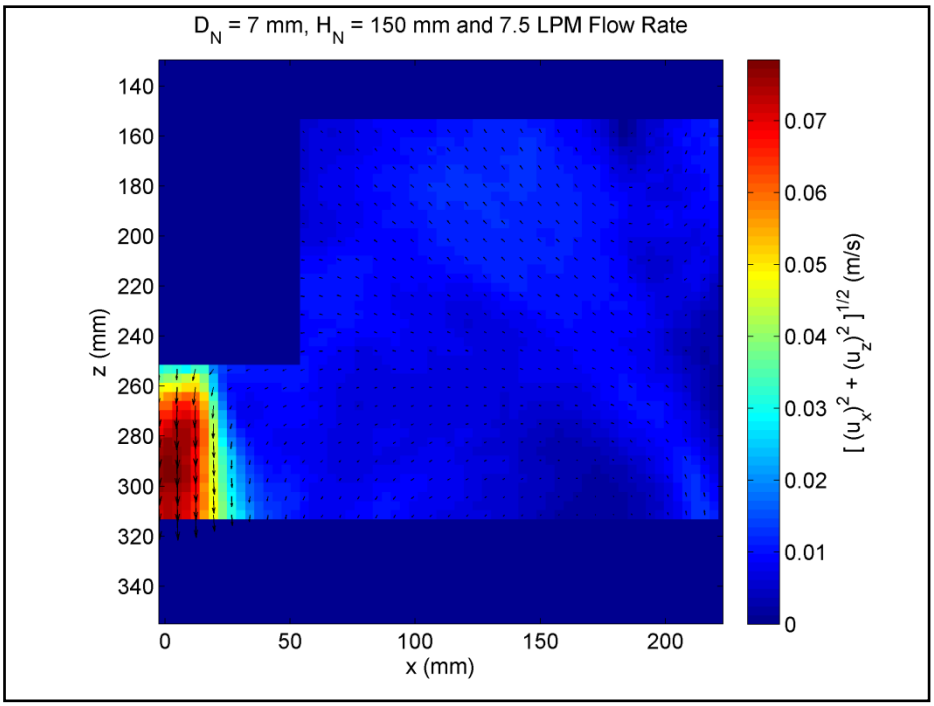

Figure A-5 Water velocity field for 7 mm D_N, 150 mm H_N and 7.5 LPM water flow rate

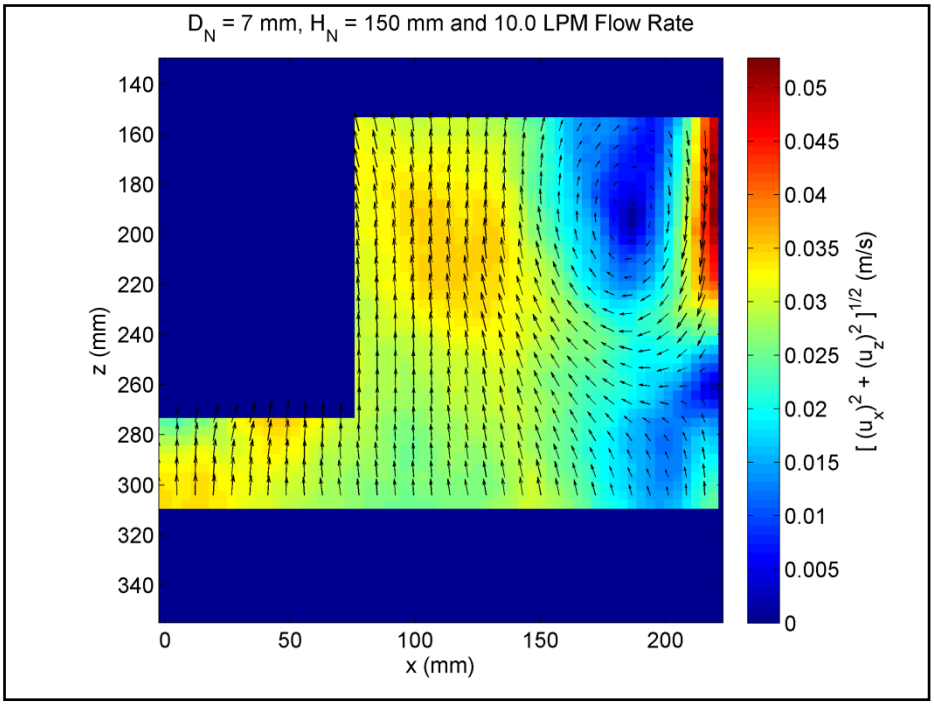

Figure A-6 Water velocity field for 7 mm D_N, 150 mm H_N and 10.0 LPM water flow rate

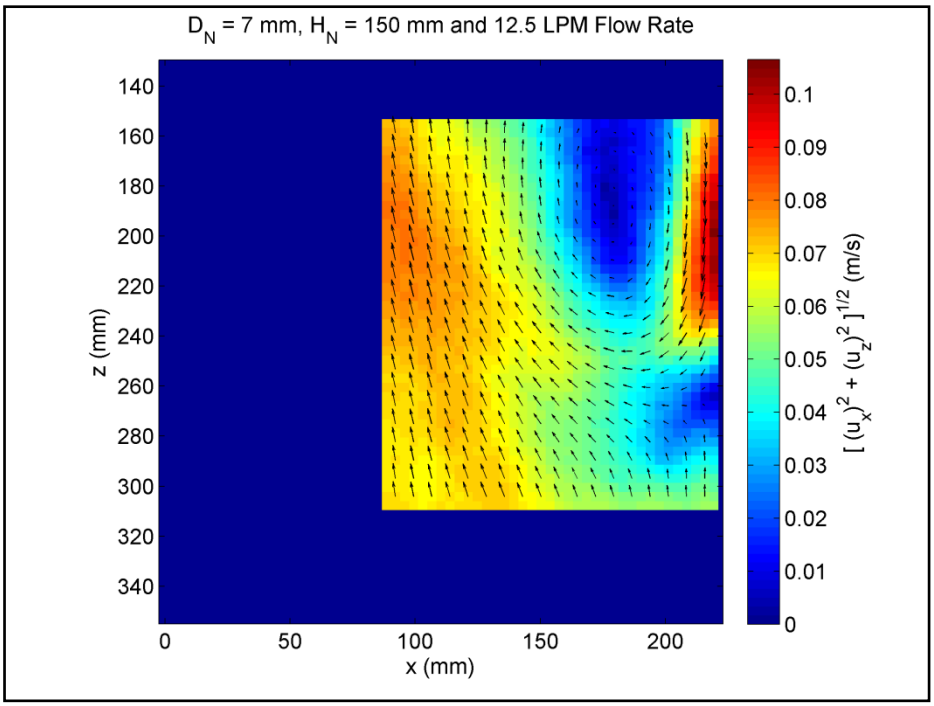

Figure A-7 Water velocity field for 7 mm D_N, 150 mm H_N and 12.5 LPM water flow rate

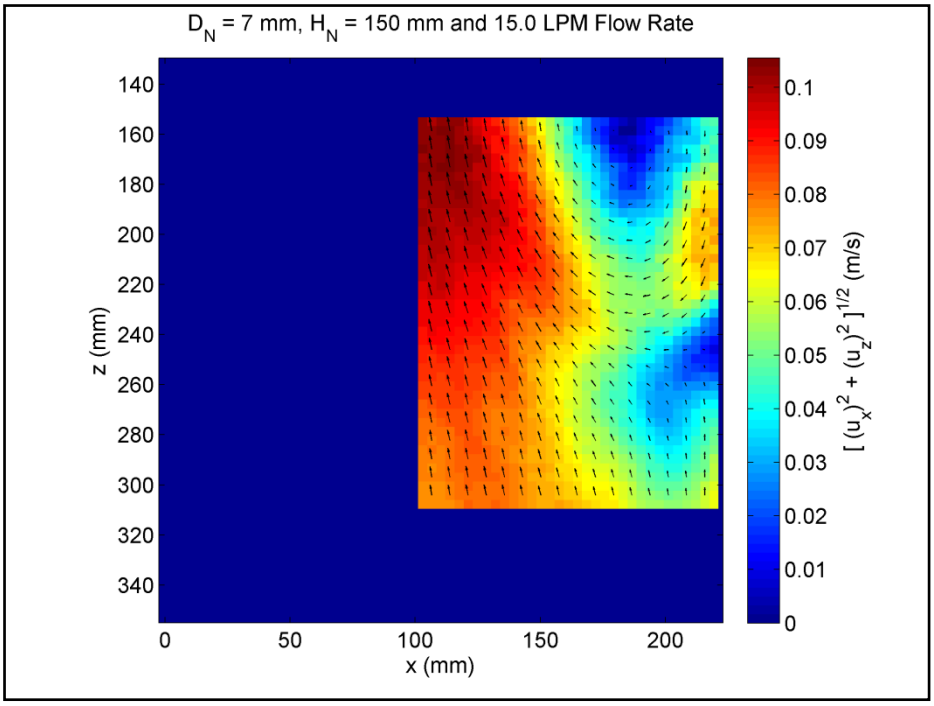

Figure A-8 Water velocity field for 7 mm D_N, 150 mm H_N and 15.0 LPM water flow rate

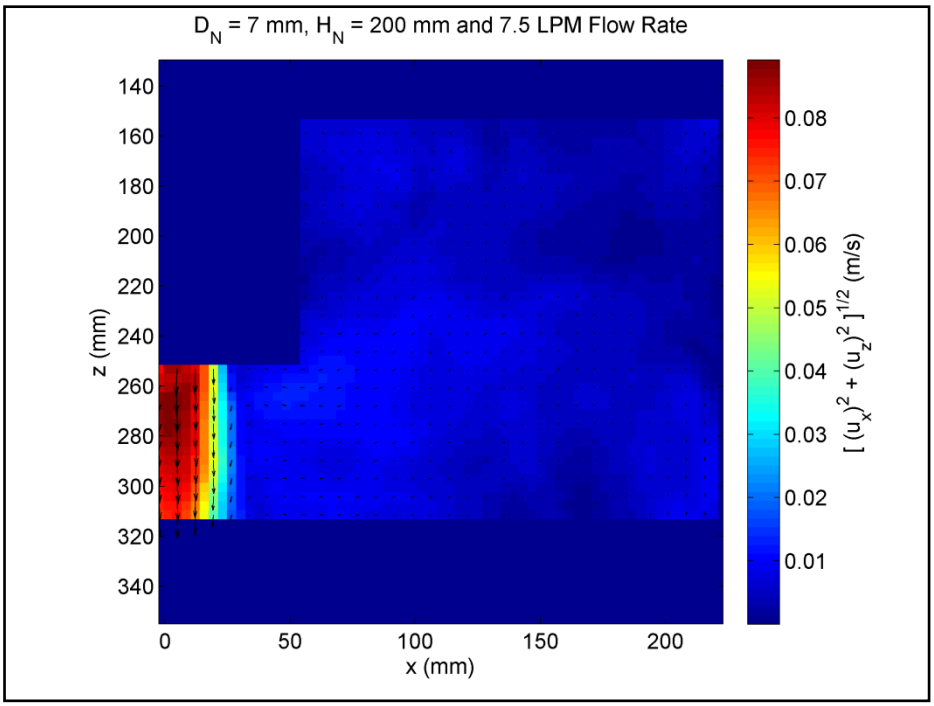

Figure A-9 Water velocity field for 7 mm D_N, 200 mm H_N and 7.5 LPM water flow rate

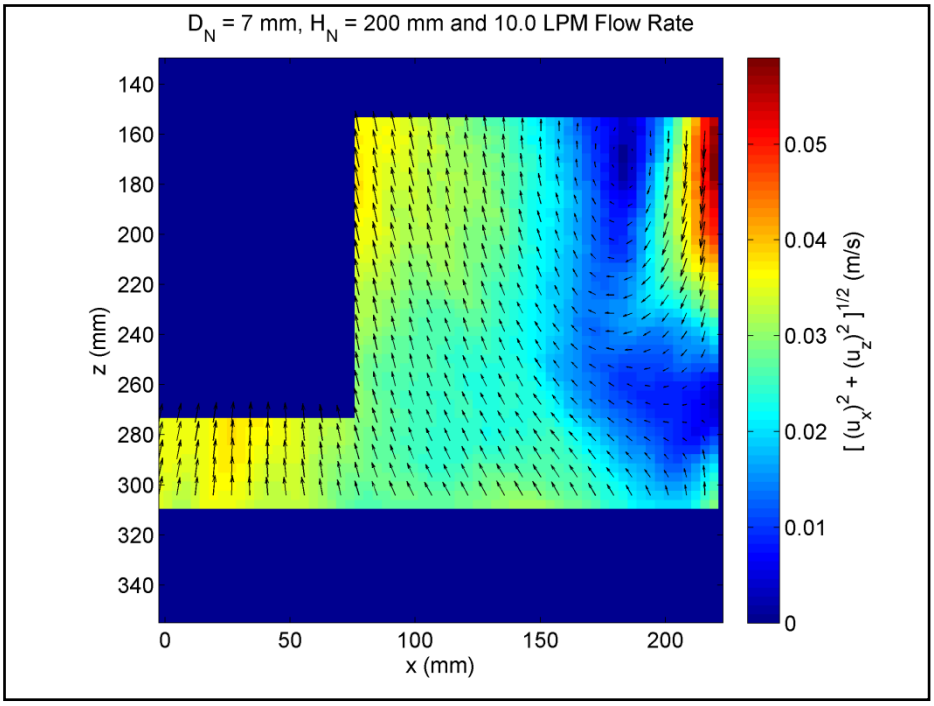

Figure A-10 Water velocity field for 7 mm D_N, 200 mm H_N and 10.0 LPM water flow rate

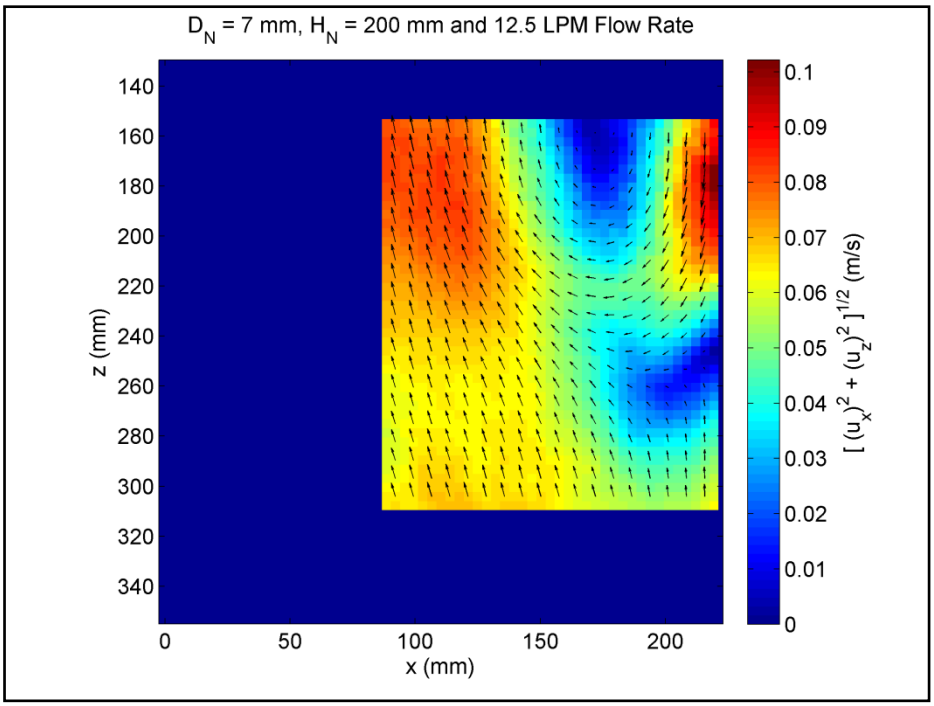

Figure A-11 Water velocity field for 7 mm D_N, 200 mm H_N and 12.5 LPM water flow rate

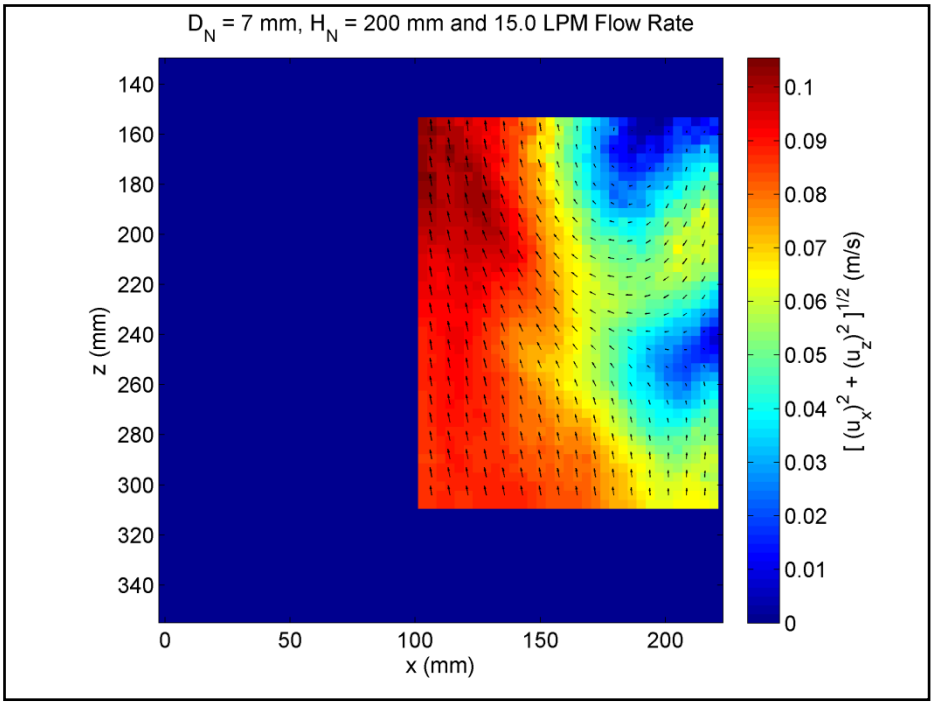

Figure A-12 Water velocity field for 7 mm D_N, 200 mm H_N and 15.0 LPM water flow rate

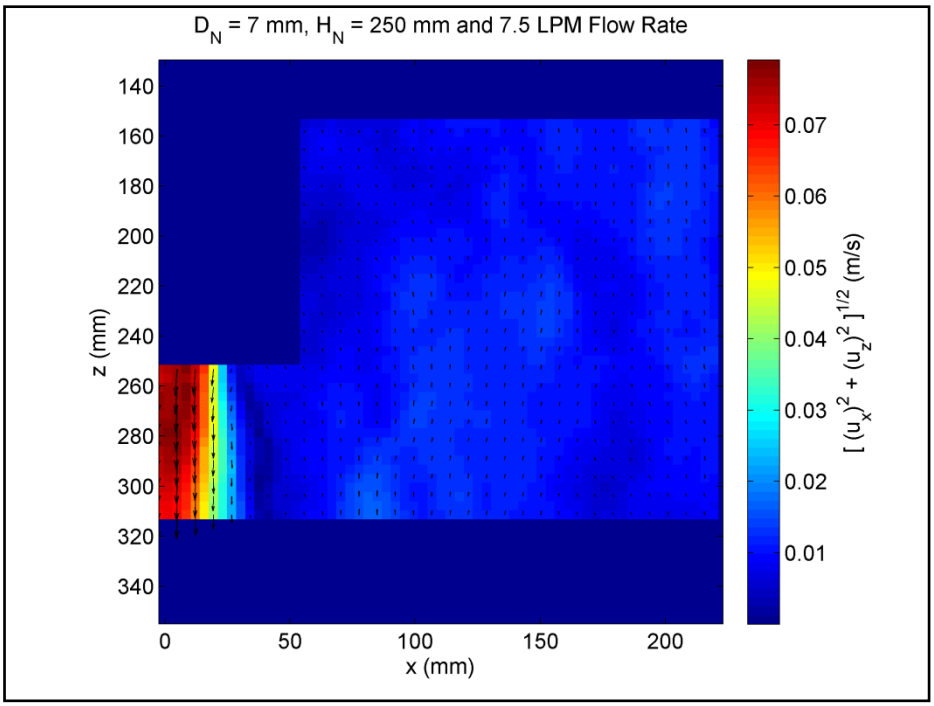

Figure A-13 Water velocity field for 7 mm D_N, 250 mm H_N and 7.5 LPM water flow rate

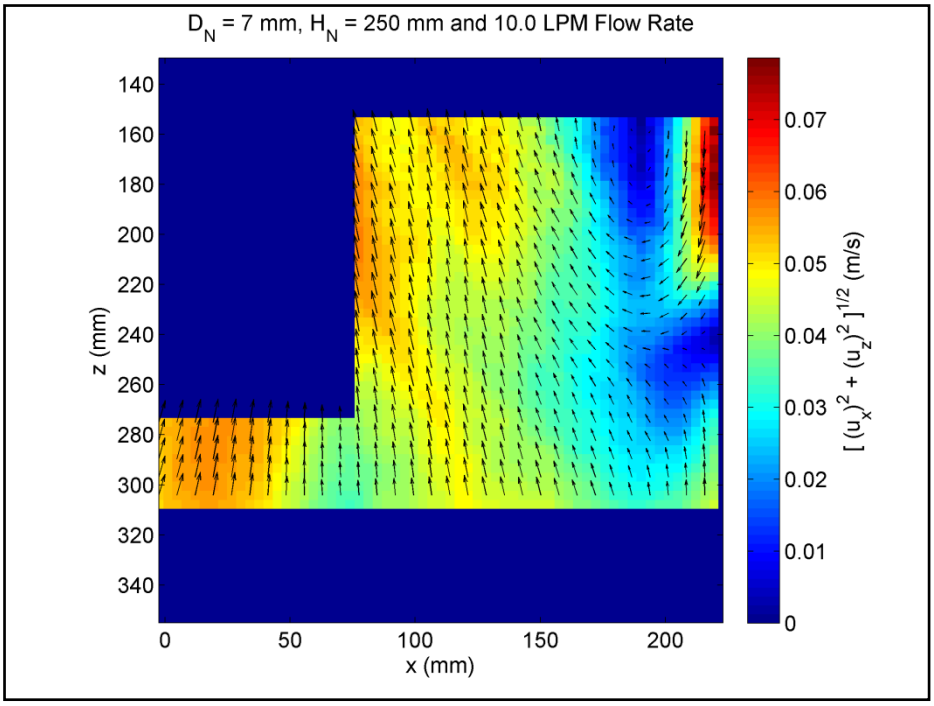

Figure A-14 Water velocity field for 7 mm D_N, 250 mm H_N and 10.0 LPM water flow rate

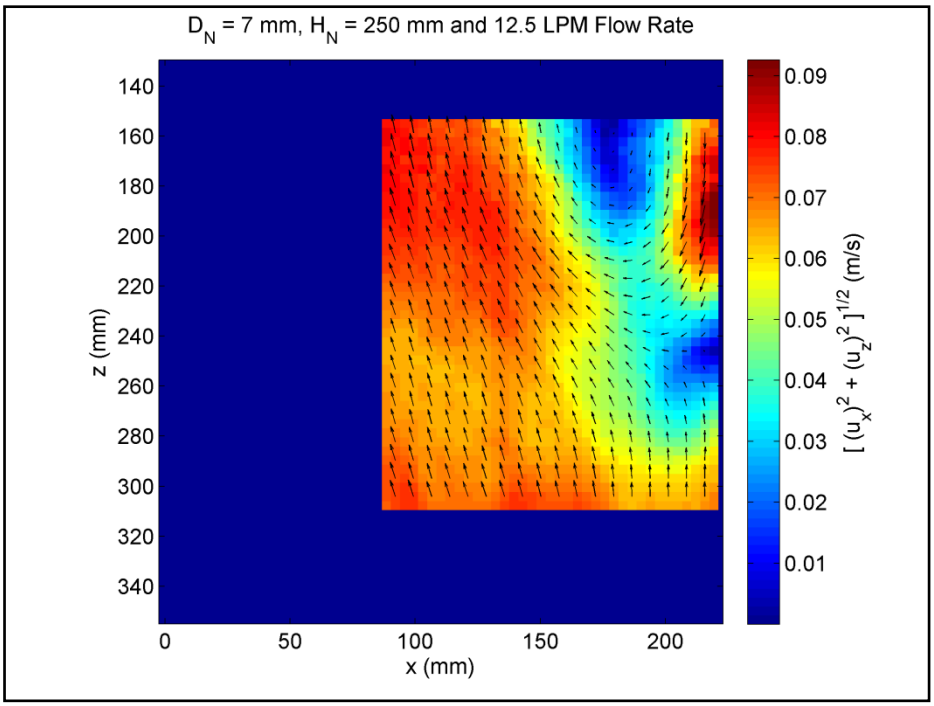

Figure A-15 Water velocity field for 7 mm D_N, 250 mm H_N and 12.5 LPM water flow rate

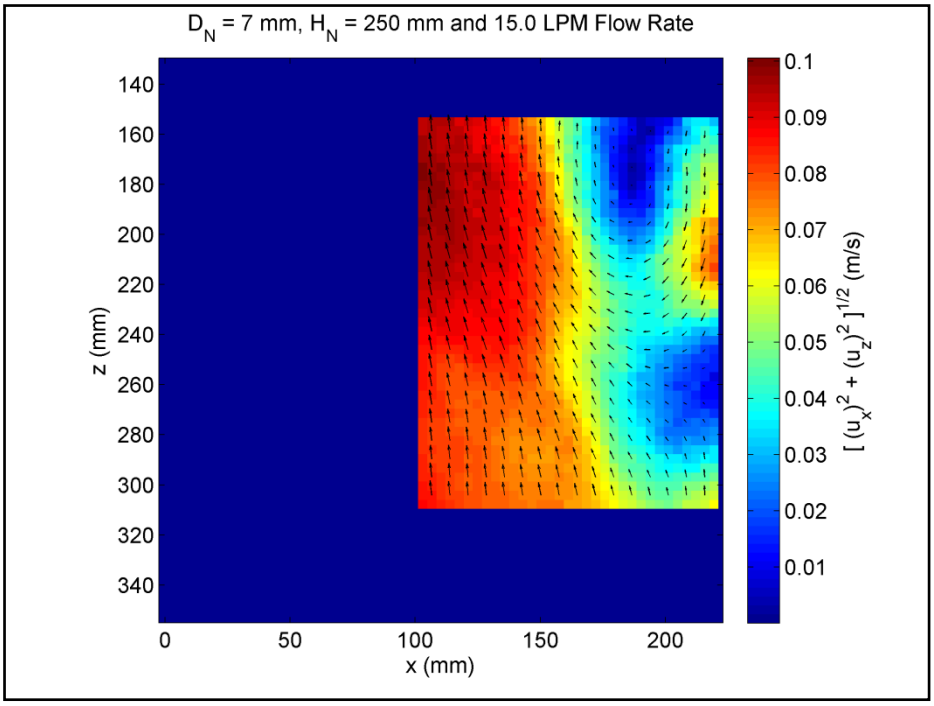

Figure A-16 Water velocity field for 7 mm D_N, 250 mm H_N and 15.0 LPM water flow rate

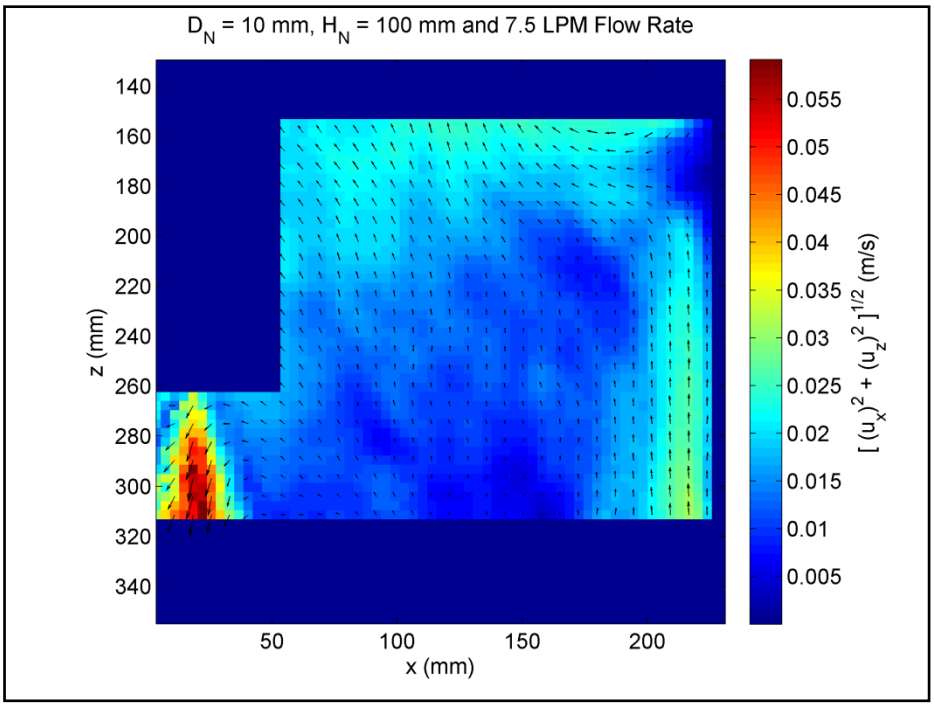

Figure A-17 Water velocity field for 10 mm D_N, 100 mm H_N and 7.5 LPM water flow rate

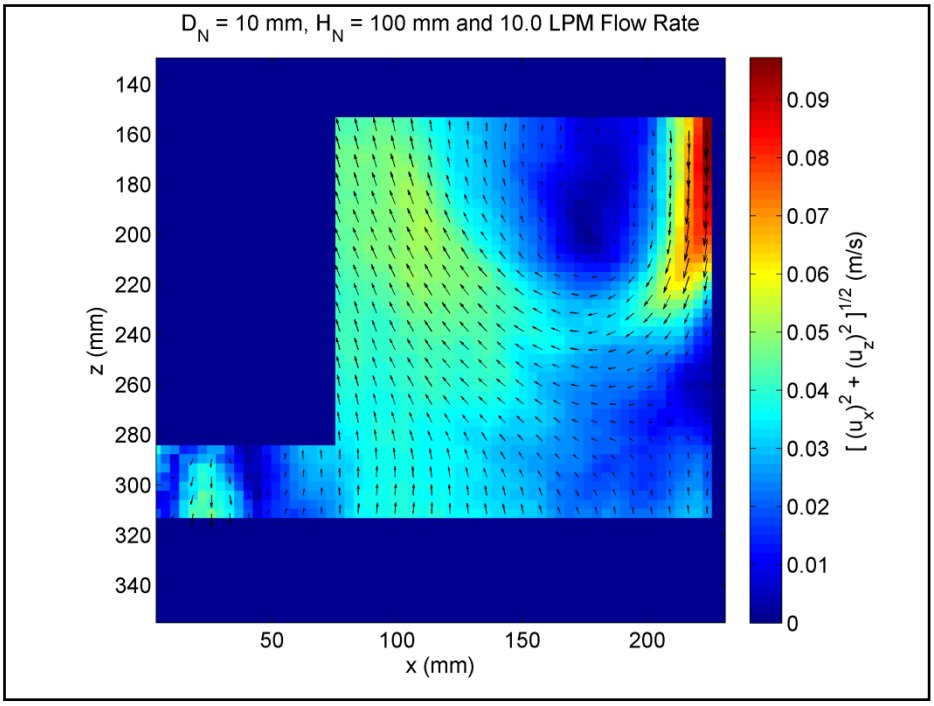

Figure A-18 Water velocity field for 10 mm D_N, 100 mm H_N and 10.0 LPM water flow rate

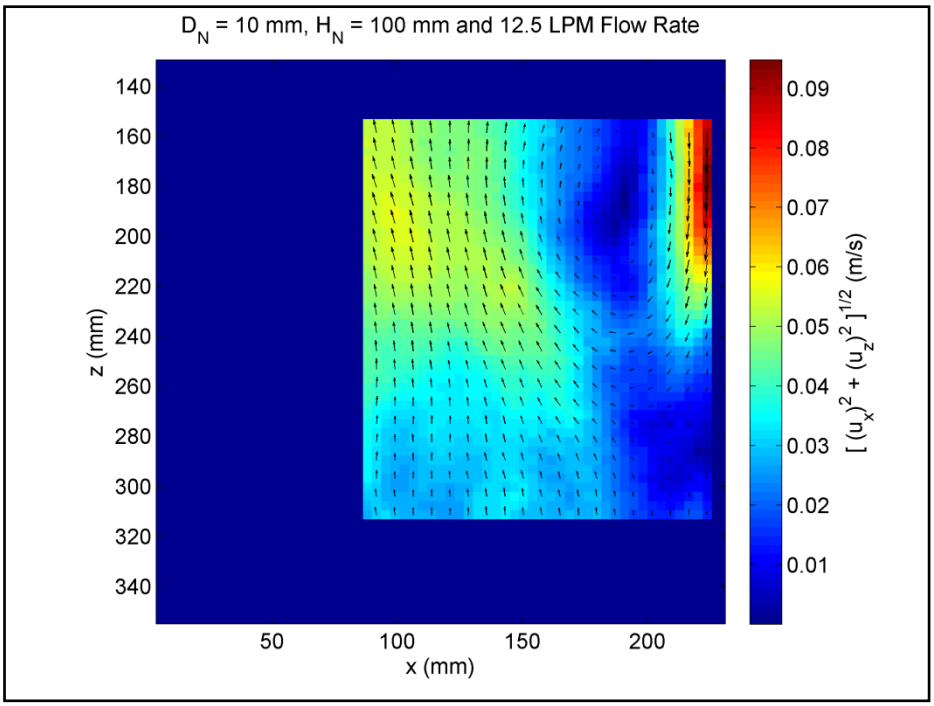

Figure A-19 Water velocity field for 10 mm D_N, 100 mm H_N and 12.5 LPM water flow rate

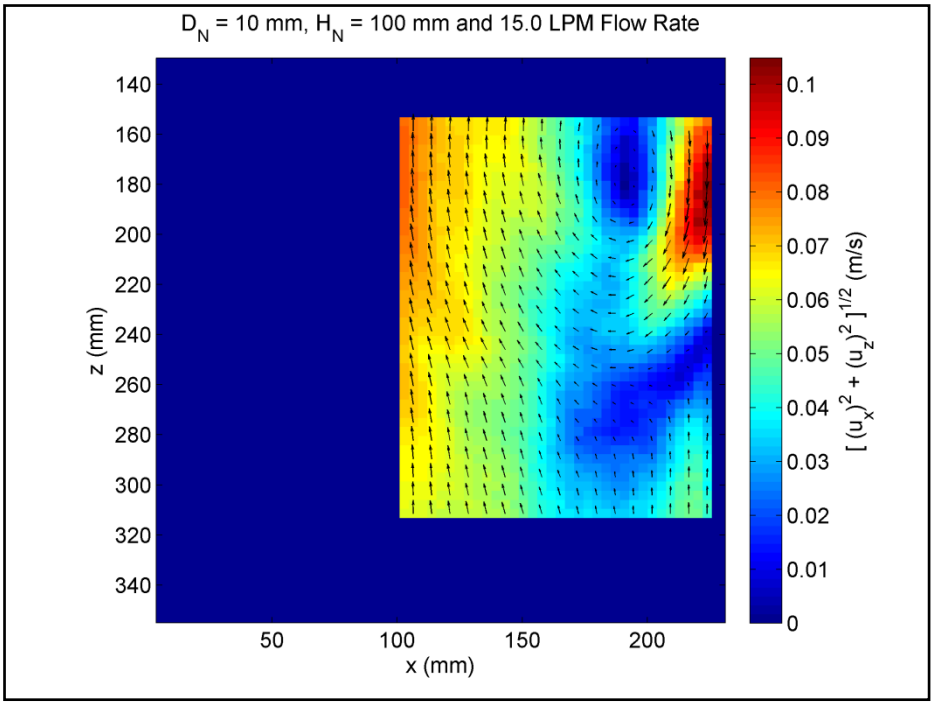

Figure A-20 Water velocity field for 10 mm D_N, 100 mm H_N and 15.0 LPM water flow rate

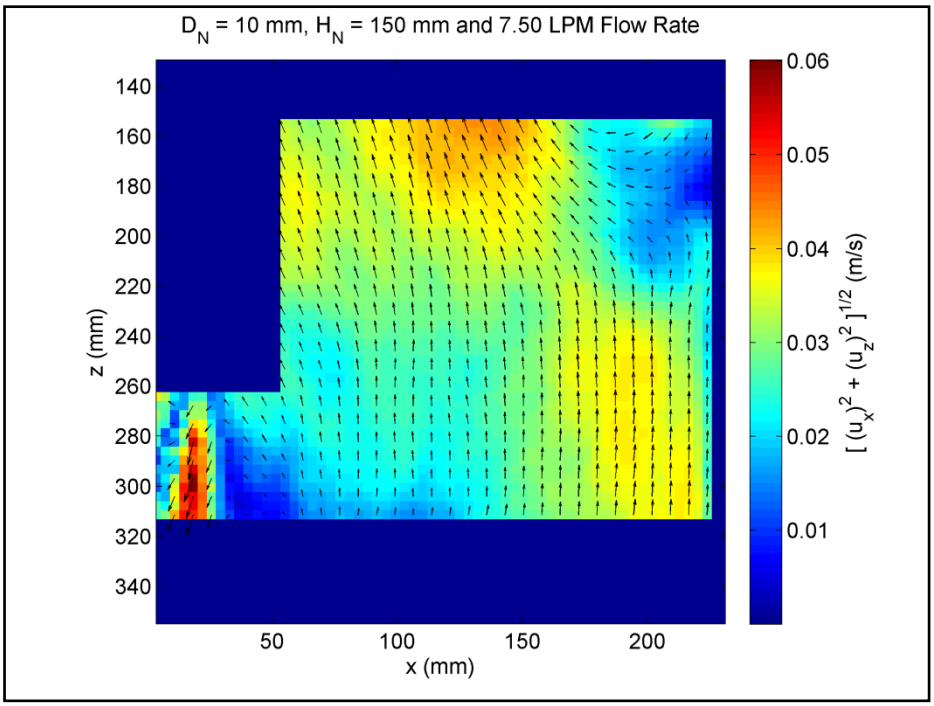

Figure A-21 Water velocity field for 10 mm D_N, 150 mm H_N and 7.5 LPM water flow rate

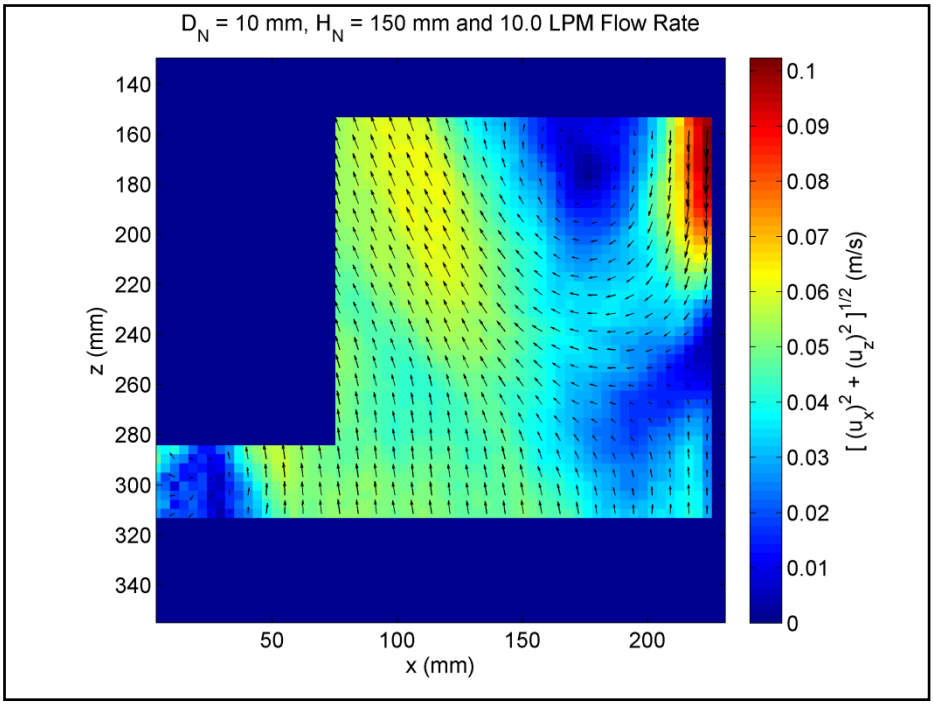

Figure A-22 Water velocity field for 10 mm D_N, 150 mm H_N and 10.0 LPM water flow rate

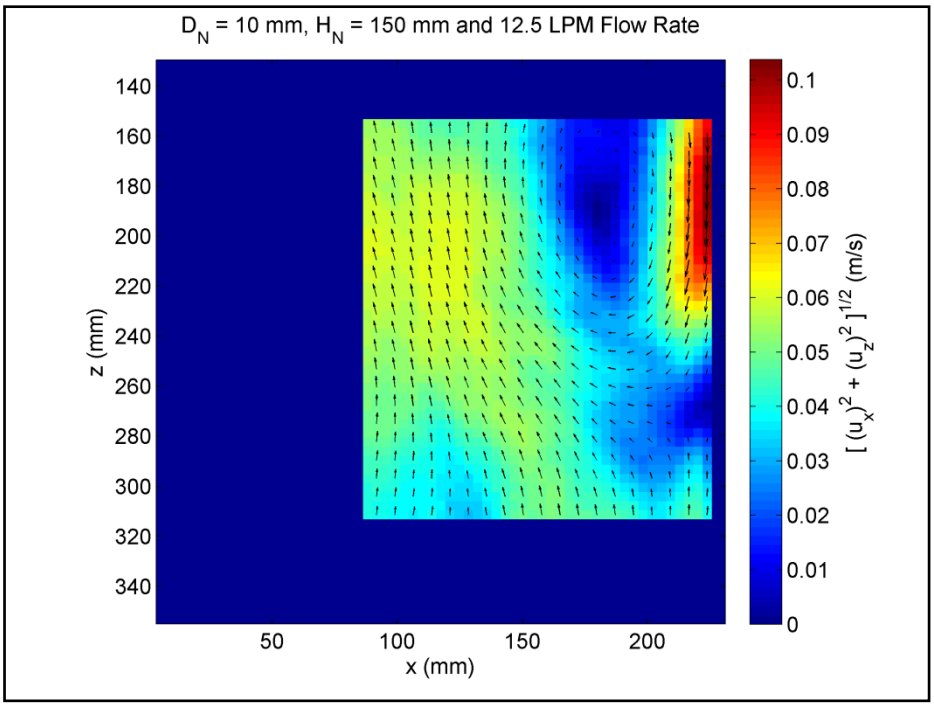

Figure A-23 Water velocity field for 10 mm D_N, 150 mm H_N and 12.5 LPM water flow rate

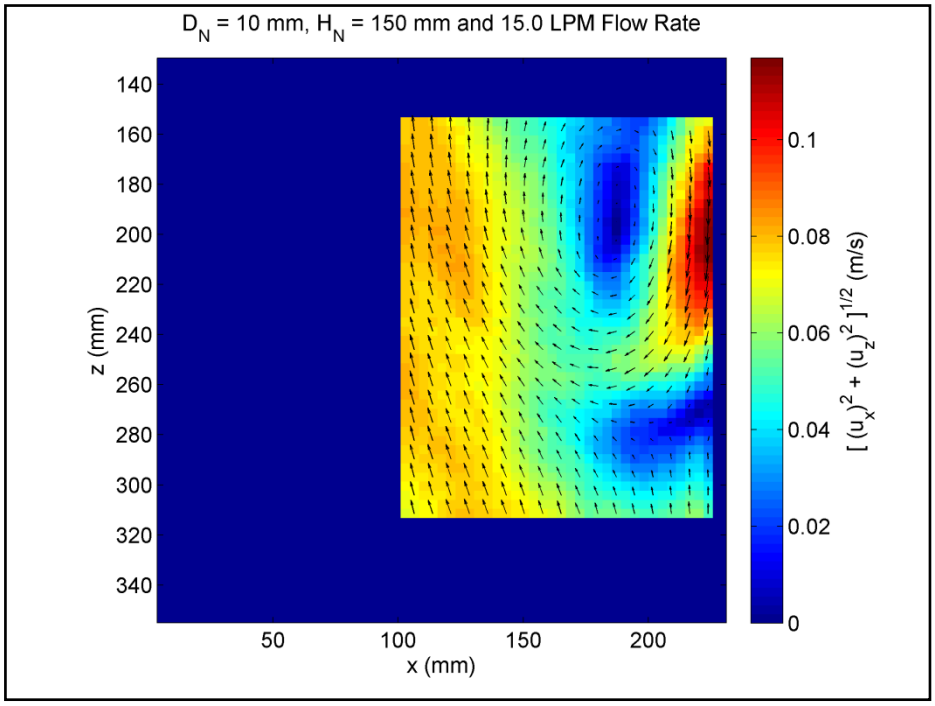

Figure A-24 Water velocity field for 10 mm D_N, 150 mm H_N and 15.0 LPM water flow rate

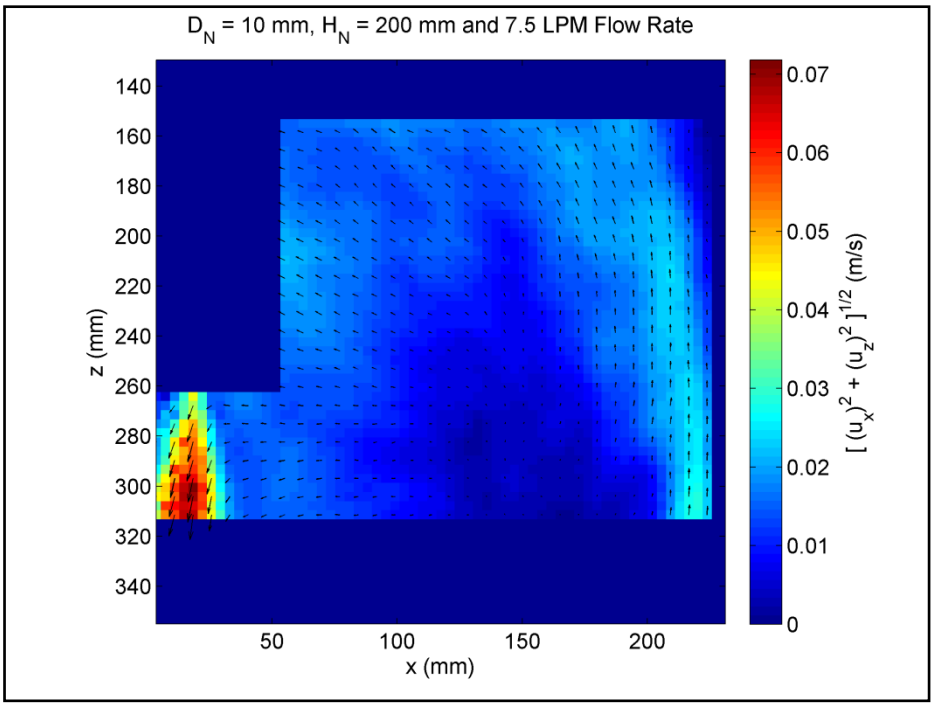

Figure A-25 Water velocity field for 10 mm D_N, 200 mm H_N and 7.5 LPM water flow rate

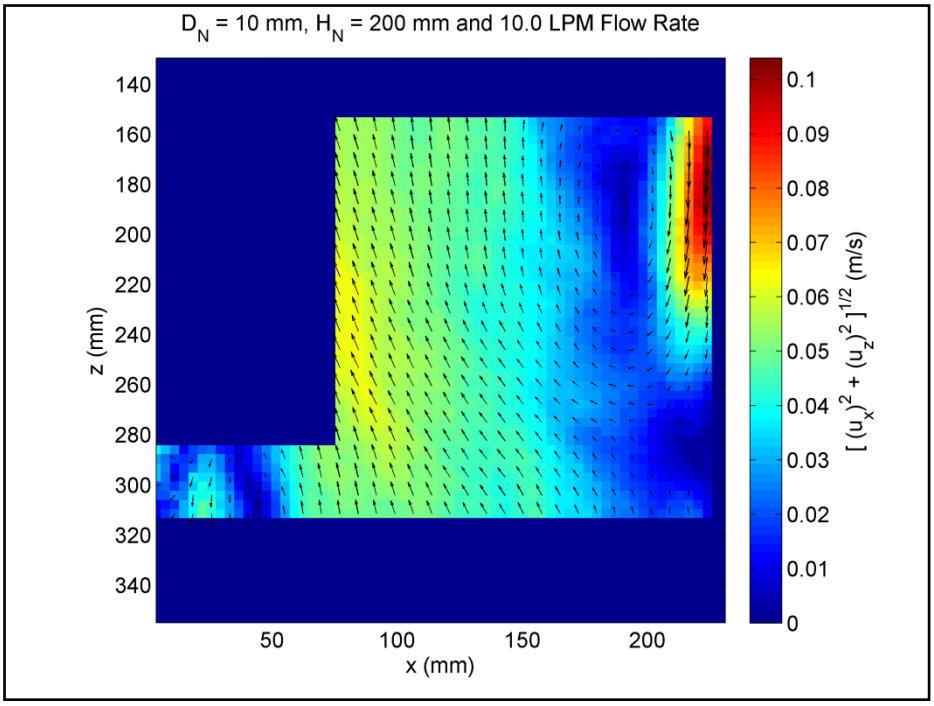

Figure A-26 Water velocity field for 10 mm D_N, 200 mm H_N and 10.0 LPM water flow rate

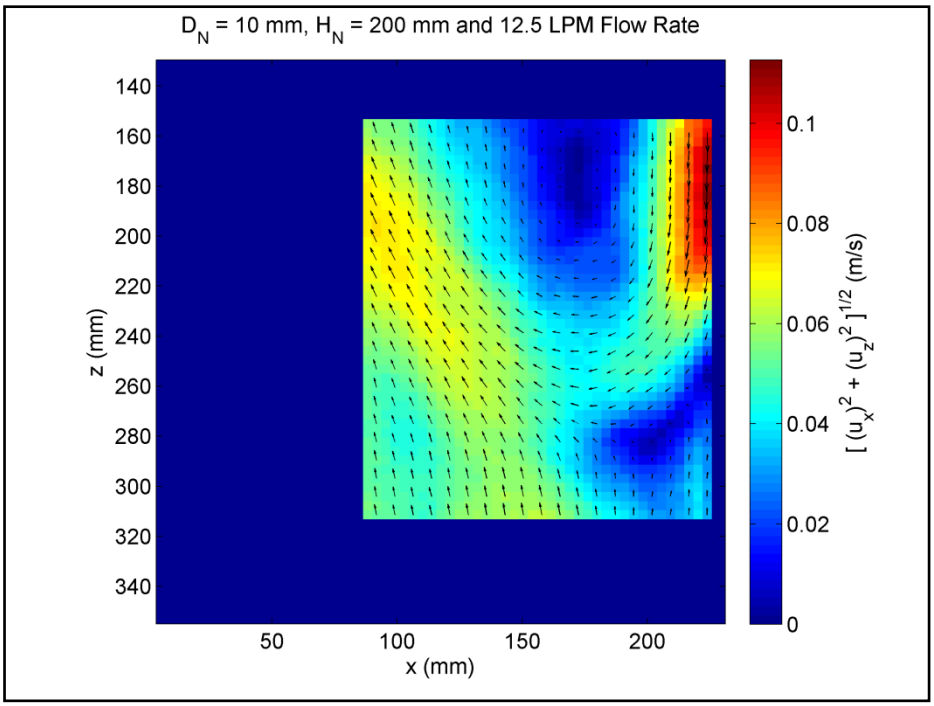

Figure A-27 Water velocity field for 10 mm D_N, 200 mm H_N and 12.5 LPM water flow rate

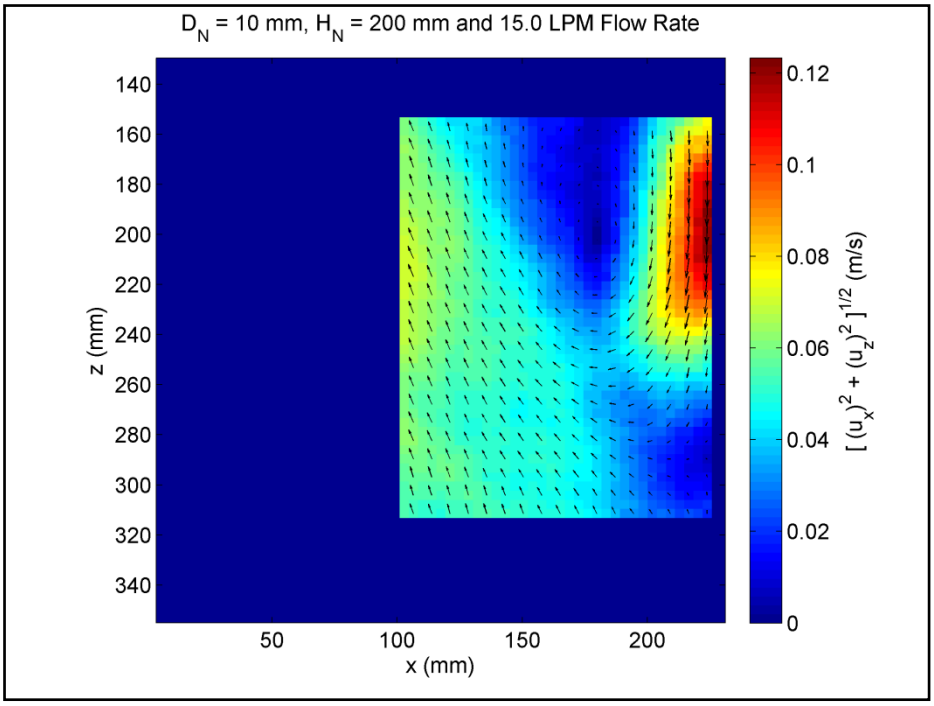

Figure A-28 Water velocity field for 10 mm D_N, 200 mm H_N and 15.0 LPM water flow rate

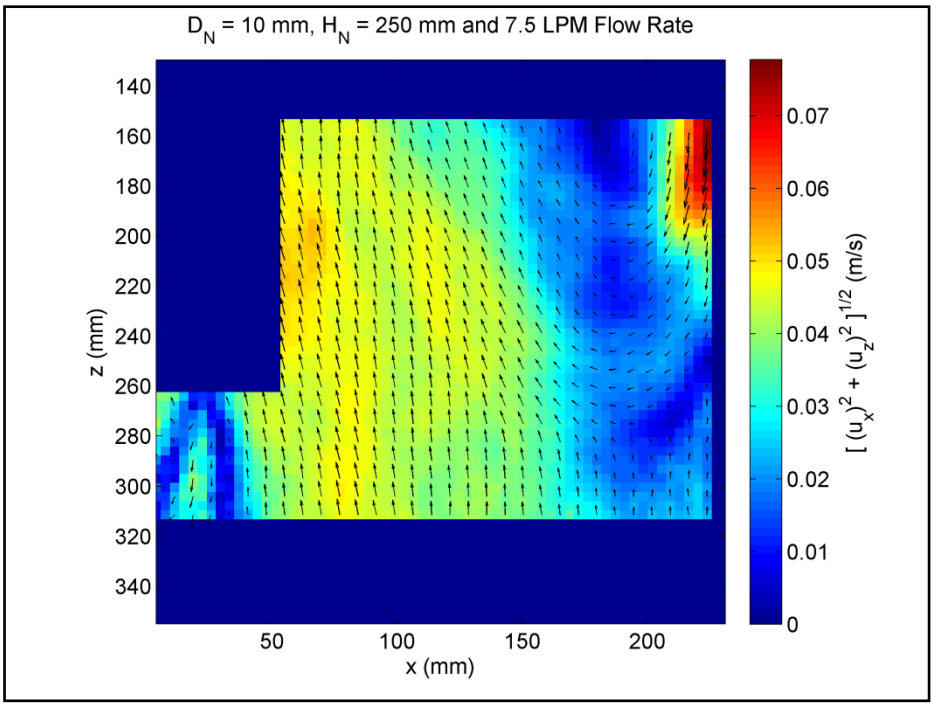

Figure A-29 Water velocity field for 10 mm D_N, 250 mm H_N and 7.5 LPM water flow rate

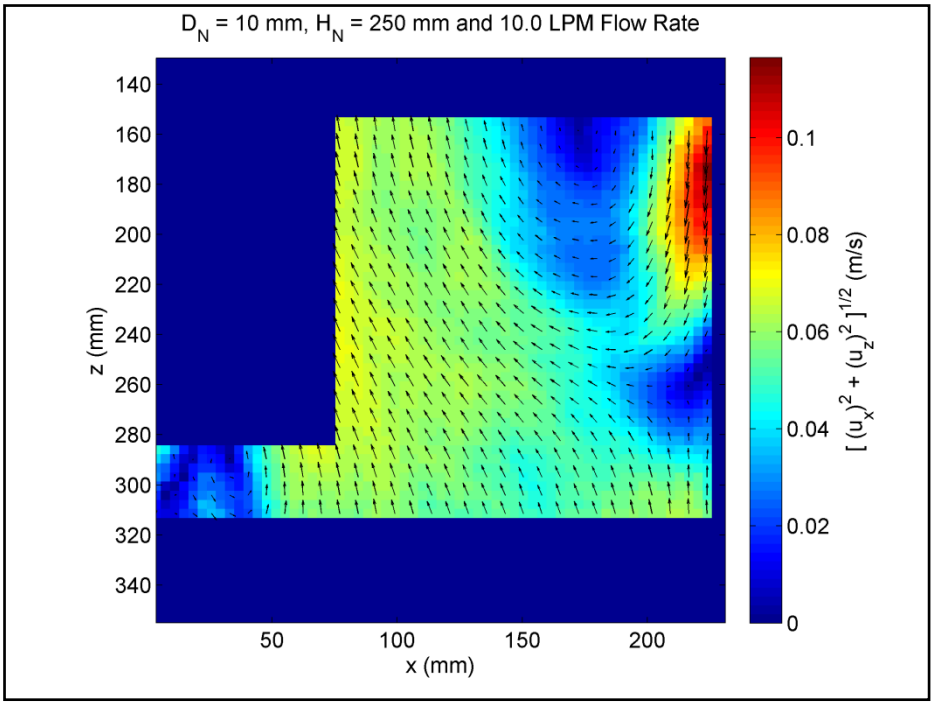

Figure A-30 Water velocity field for 10 mm D_N, 250 mm H_N and 10.0 LPM water flow rate

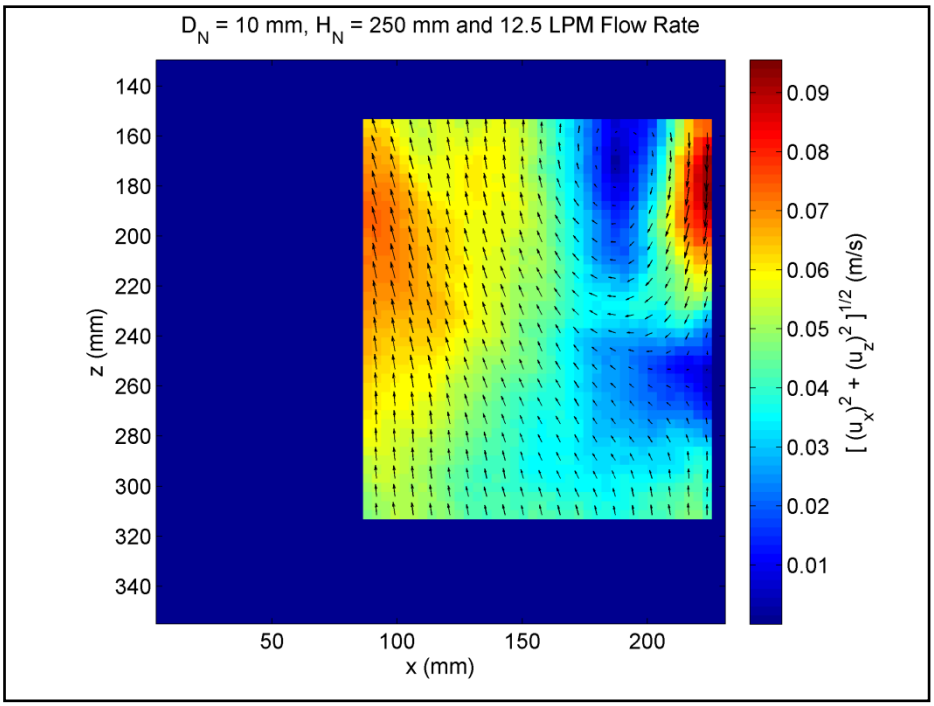

Figure A-31 Water velocity field for 10 mm D_N, 250 mm H_N and 12.5 LPM water flow rate

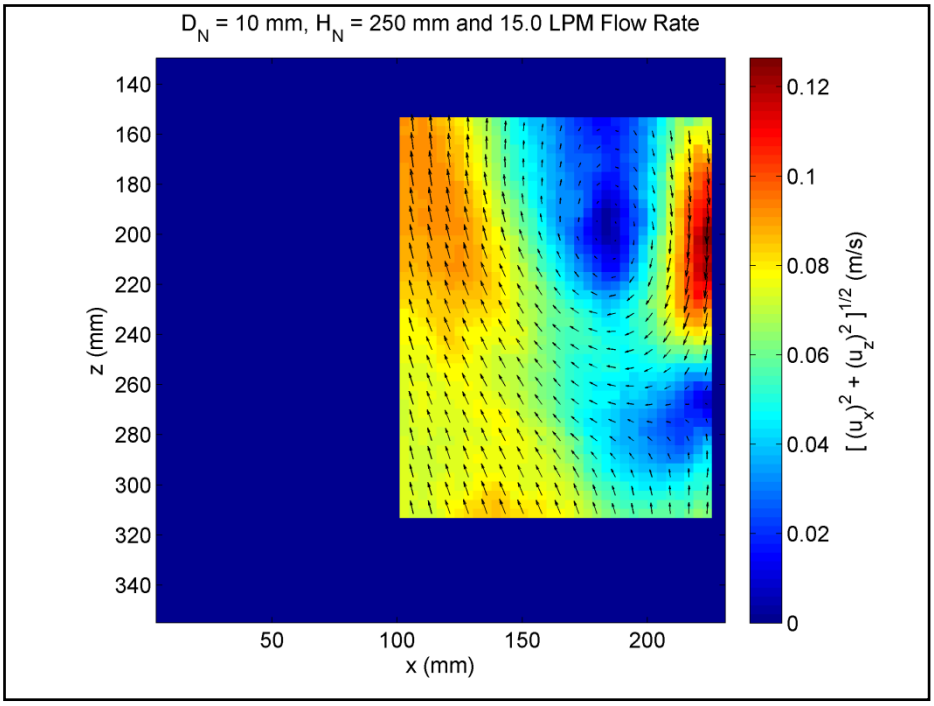

Figure A-32 Water velocity field for 10 mm D_N, 250 mm H_N and 15.0 LPM water flow rate

Appendix B MATLAB Programs for Image Processing of High Speed Camera Photographs

B.1 Script for Splitting Multipage Tiff Files

```
clear all, clc, close all

name='34 mm dc, 7mm id, 10 cm Jet Length, 12.5 LPM, 50 FPS, 1a'; %Input file name here

fname=[name,'.tif'];

info=imfinfo(fname); %Genrates information for the fname structure

num_images=numel(info); %Produces number of arrays

for k = 1:num_images

    A=imread(fname, k);
```

```
outputfile = [name, int2str(k), '.tif']%Dynamic creation of string arrays
imwrite(A, outputfile, 'tif', 'compression', 'none')
end

fname='34 mm dc, 7mm id, 10 cm Jet Length, 12.5 LPM, 50 FPS, 1b.tif';
info=imfinfo(fname);
num_images=numel(info);
for k = 1:num_images
    A=imread(fname, k);
outputfile = [name, int2str(1500+k), '.tif']
imwrite(A, outputfile, 'tif', 'compression', 'none')
end
fname='34 mm dc, 7mm id, 10 cm Jet Length, 12.5 LPM, 50 FPS, 1c.tif';
info=imfinfo(fname);
num_images=numel(info);
for k = 1:num_images
    A=imread(fname, k);
outputfile = [name, int2str(3000+k), '.tif']
imwrite(A, outputfile, 'tif', 'compression', 'none')
end
fname='34 mm dc, 7mm id, 10 cm Jet Length, 12.5 LPM, 50 FPS, 1d.tif';
```

```
info=imfinfo(fname);

num_images=numel(info);

for k = 1:num_images

    A=imread(fname, k);

outputfile = [name, int2str(4500+k), '.tif']

imwrite(A, outputfile, 'tif', 'compression', 'none')

end
```

B.2 Script for Bubble Plume Boundary Detection

```
clc; clear all; close all;

tic

bcground=(imread('Background.tif'));

bcground=rgb2gray(bcground);

bcground=imcrop(bcground, [188 0 326 480]);

% Declaring Variables

film=uint8(zeros(434, 327, 6000));

leftcontour=zeros(233,2,6000);

rightcontour=zeros(233,2,6000);

contourthickness=zeros(233,2,6000);

aveleftcontour=zeros(233,2);

averightcontour=zeros(233,2);

%Declaring depth matrix
```

```
depth=zeros(6000,3);

for k=1:6000

k

filenamea=['34 mm dc, 7mm id, 10 cm Jet Length, 12.5 LPM, 50 FPS, 1a',
int2str(k), '.tif']; %Provide image file name

a=(imread(filenamea));

a=rgb2gray(a);

a=imcrop(a, [188 0 326 480]);

asubtracted=imsubtract(imcomplement(a),imcomplement(bcground));

ave=asubtracted;

ave=imcrop(ave, [1 47 326 433]); %Cropping to remove air space

ave(410:end,:)=0;

ave(1:40,:)=1;

ave(:,1:24)=0;

ave(:,301:end)=0;

avebw=im2bw(ave, 15/256); %Thresholding

avebwd=imdilate(avebw, strel('disk', 9));

avebwde=imerode(avebwd, strel('disk', 9));

avebwdef=imfill(avebwde, 'holes');

avebwdefe=imerode(avebwdef, strel('disk', 8));

avebwdefee=imreconstruct(avebwdefe, avebwdef);
```

```
[B,L] = bwboundaries(avebwdefee,8,'noholes');
for count = 1:length(B)
    count
    if count>1
        bcground=ones(6000,120,3); %It has been put as a safeguard to avoid code execution due to prsence of more than one objects
    end
boundary = B{count};
num=(size(boundary, 1));
%Genration of boundary coordinates
for rindex=1:233
idx=find(boundary(:,1)==rindex);
colmax=max(boundary(idx,2));
colmin=min(boundary(idx,2));
leftcontour(rindex,:,k)=[rindex, colmin];
rightcontour(rindex,:,k)=[rindex, colmax];
contourthickness(rindex,:,k)=[rindex, (colmax-colmin)];
end
aveleftcontour=aveleftcontour+leftcontour(:,:,k);
averightcontour=averightcontour+rightcontour(:,:,k);
%Generating depth matrix
```

```
depcol=165;

deprowidx=find(boundary(:,2)==depcol);

deprow=max(boundary(deprowidx,1));

depth(k, :, :)=[k, deprow, depcol];

%Making film

film(:, :, k)=ave;

for r=1:num

   film(boundary(r, 1),boundary(r, 2),k)=255;

end

end

end

aveleftcontour=aveleftcontour./6000;

averightcontour=averightcontour./6000;

t0=toc

implay(film)

matrix2video(film, 10, 3, 1,0)

% Plotting depth matrix

figure, plot(depth(:,1), depth(:,2)) % Plots depth of the plume over 6000 image frames in pixel values
```

B.3 Script for Transforming Boundary Coordinates from Image Space to Spatial Coordinate Space

```
figure, hleft=plot((aveleftcontour(41:end,2)-165)/1.1,(434-
aveleftcontour(41:end,1))/1.1, 'r', 'LineWidth',1 );

hold on

hright=plot((averightcontour(41:end,2)-165)/1.1,(434-
averightcontour(41:end,1))/1.1, 'r', 'LineWidth',1 );

set(gca,'XTick',-175:50:175)

set(gca,'XMinorTick','on')

set(gca,'YTick',0:50:425)

set(gca,'YMinorTick','on')

y=linspace(434/1.1,201/1.1,44);

xl=(ones(length(y))*143-165)/1.1;

htubel=plot(xl, y, 'k', 'LineWidth',2);

xr=(ones(length(y))*187-165)/1.1;

htuber=plot(xr, y, 'k', 'LineWidth',2);

xbase=0;

ybase=0;

hbase=plot(xbase,ybase);

xlabel('X(mm)')

ylabel('Z(mm)')

tit=sprintf('%s\n%s', 'Time Averaged Bubble Plume Profile','D_N = 7 mm, H_N =
100 mm and 12.5 LPM Flow Rate');

title(tit,'interpreter','tex')
```

```
xright=165/1.1;

xleft=-xright;

hrightp=plot(xright,0);

hleftp=plot(xleft,0);

axis image

grid on

leftcontour_sq=leftcontour;

for k=1:6000

leftcontour_sq(:,2,k)=(leftcontour(:,2,k)-aveleftcontour(:,2)).^2;

end;

rmsleft=sqrt(sum(leftcontour_sq, 3)/6000);

avadded_rmsleft=aveleftcontour(:,2)+rmsleft(:,2);

avminus_rmsleft=aveleftcontour(:,2)-rmsleft(:,2);

hrmsleftadd=plot((avadded_rmsleft(41:end)-165)/1.1,(434-
aveleftcontour(41:end,1))/1.1, '--b' );

hrmsleftsub=plot((avminus_rmsleft(41:end)-165)/1.1,(434-
aveleftcontour(41:end,1))/1.1, '--g' );

rightcontour_sq=rightcontour;

for k=1:6000

rightcontour_sq(:,2,k)=(rightcontour(:,2,k)-averightcontour(:,2)).^2;

end;
```

```
rmsright=sqrt(sum(rightcontour_sq, 3)/6000);

avadded_rmsright=averightcontour(:,2)+rmsright(:,2);

avminus_rmsright=averightcontour(:,2)-rmsright(:,2);

hrmsrightadd=plot((avadded_rmsright(41:end)-165)/1.1,(434-
averightcontour(41:end,1))/1.1, '--g' );

hrmsrightsub=plot((avminus_rmsright(41:end)-165)/1.1,(434-
averightcontour(41:end,1))/1.1, '--b' );

legend( [hleft, hrmsleftadd, hrmsleftsub],'Average', 'Average-rms',
'Average+rms', 'Location', 'SouthEast');

print -dtiff -r300 '34 mm dc, 7mm id, 10 cm Jet Length, 12.5 LPM.tif'

save('34 mm dc, 7mm id, 10 cm Jet Length, 12.5 LPM.mat');

save('34 mm dc, 7mm id, 10 cm Jet Length, 12.5 LPM depth matrix.mat',
'depth');
```

Appendix C Ensemble Averaged Bubble Plume Boundaries

Ensemble Averaged Bubble Plume profiles for the test cases of Test Matrix 1 and 2 (Tables 2-1 and 2-2) are being provided below:

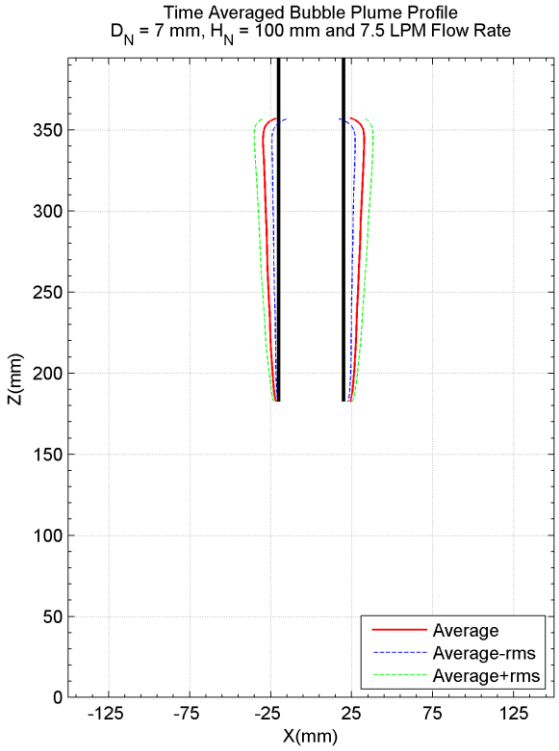

Figure C-1 D_N = 7 mm, H_N = 100 mm and Water Flow Rate = 7.5 LPM

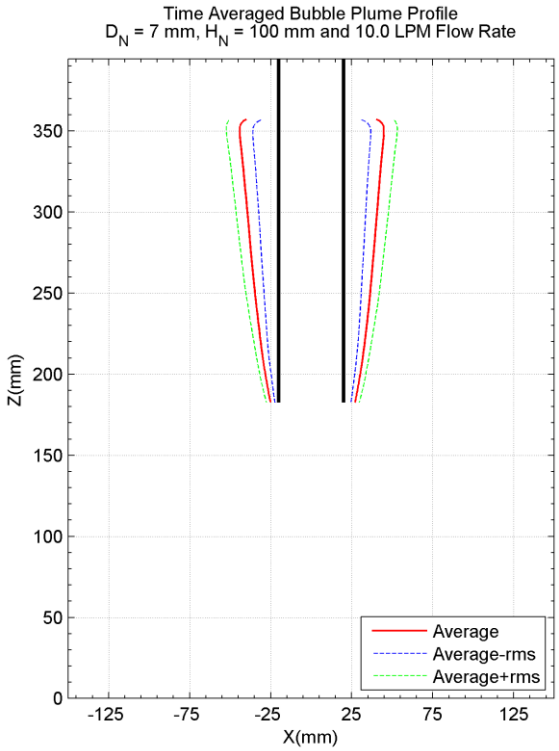

Figure C-2 D_N = 7 mm, H_N = 100 mm and Water Flow Rate = 10.0 LPM

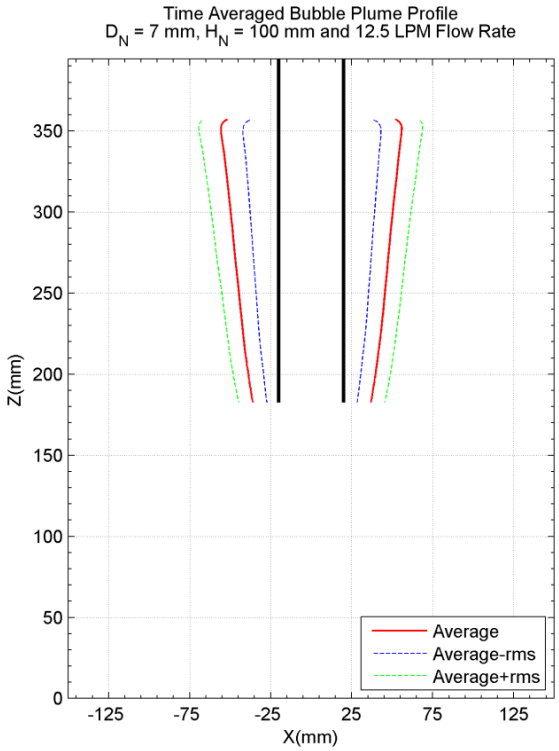

Figure C-3 D_N = 7 mm, H_N = 100 mm and Water Flow Rate = 12.5 LPM

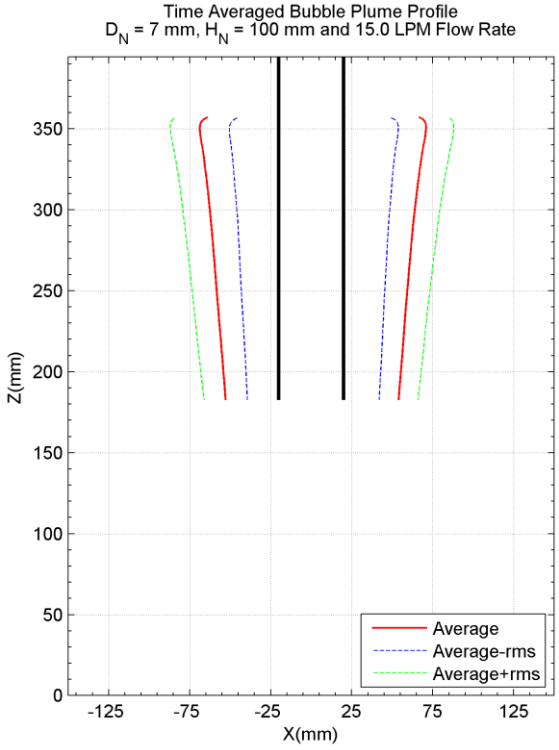

Figure C-4 D_N = 7 mm, H_N = 100 mm and Water Flow Rate = 15.0 LPM

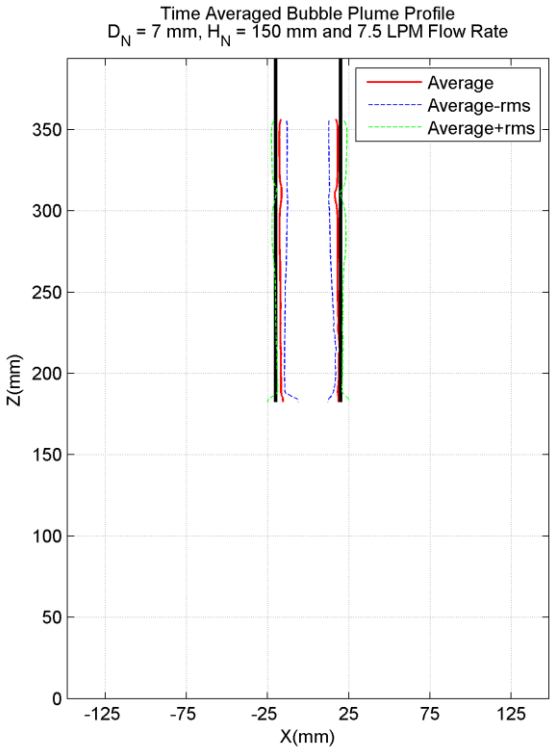

Figure C-5 D_N = 7 mm, H_N = 150 mm and Water Flow Rate = 7.5 LPM

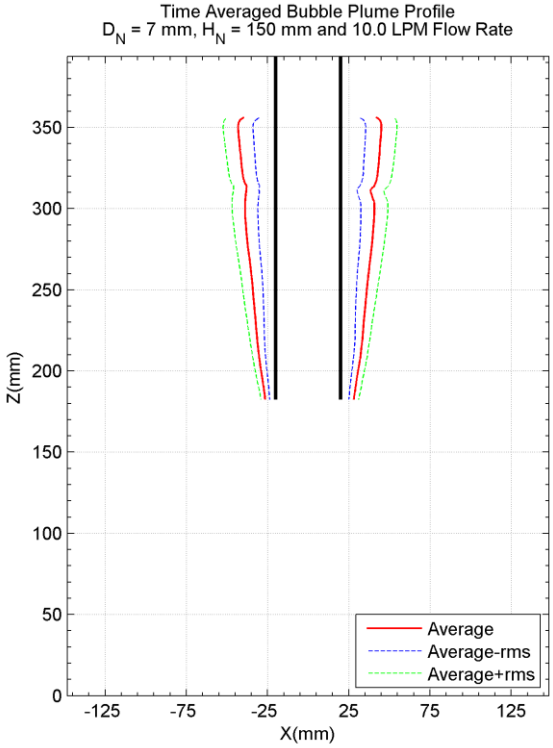

Figure C-6 D_N = 7 mm, H_N = 150 mm and Water Flow Rate = 10.0 LPM

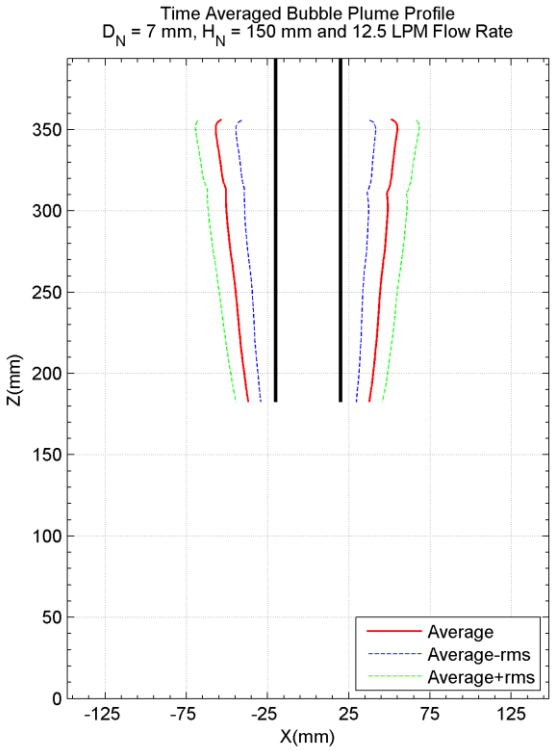

Figure C-7 D_N = 7 mm, H_N = 150 mm and Water Flow Rate = 12.5 LPM

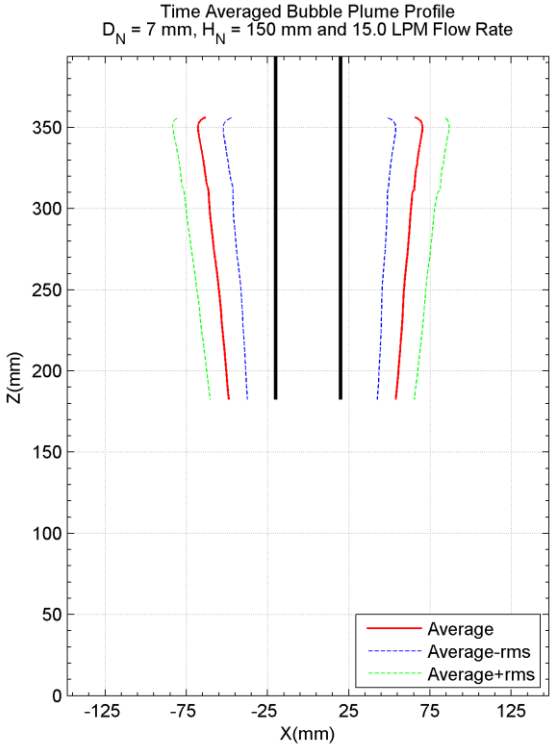

Figure C-8 D_N = 7 mm, H_N = 150 mm and Water Flow Rate = 15.0 LPM

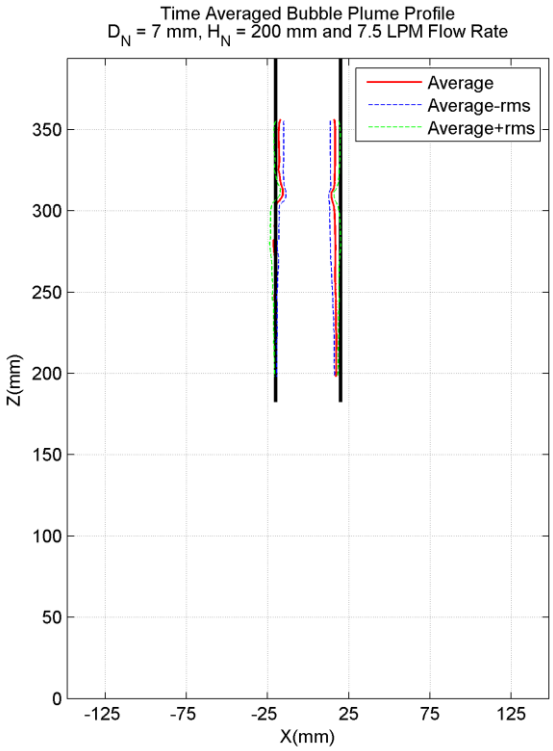

Figure C-9 D_N = 7 mm, H_N = 200 mm and Water Flow Rate = 7.5 LPM

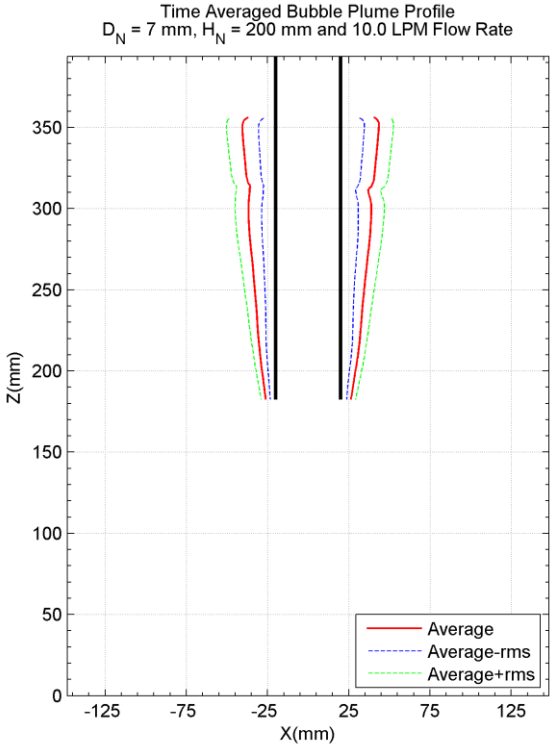

Figure C-10 D_N = 7 mm, H_N = 200 mm and Water Flow Rate = 10.0 LPM

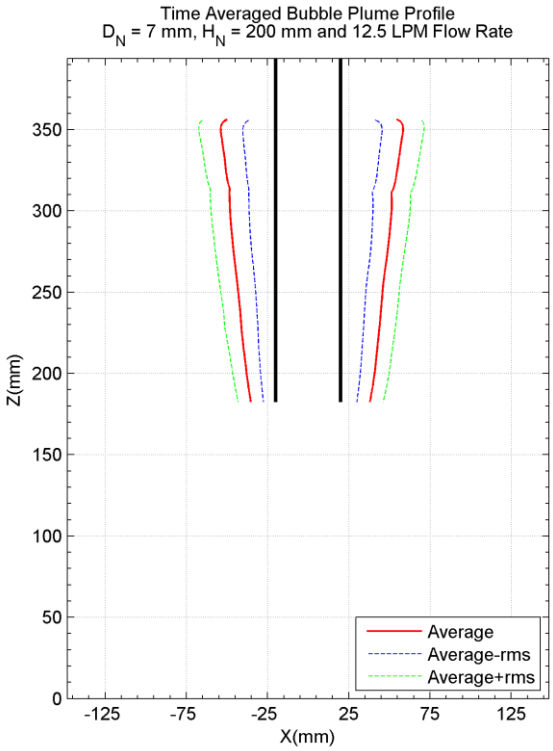

Figure C-11 D_N = 7 mm, H_N = 200 mm and Water Flow Rate = 12.5 LPM

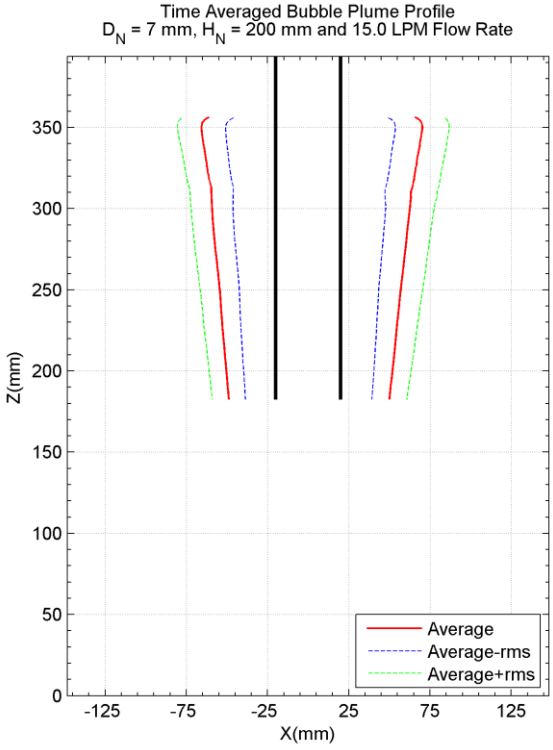

Figure C-12 D_N = 7 mm, H_N = 200 mm and Water Flow Rate = 15.0 LPM

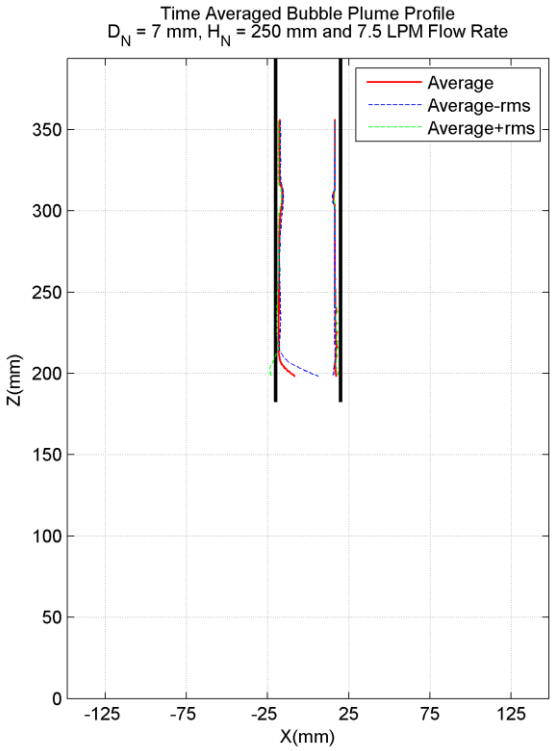

Figure C-13 D_N = 7 mm, H_N = 250 mm and Water Flow Rate = 7.5 LPM

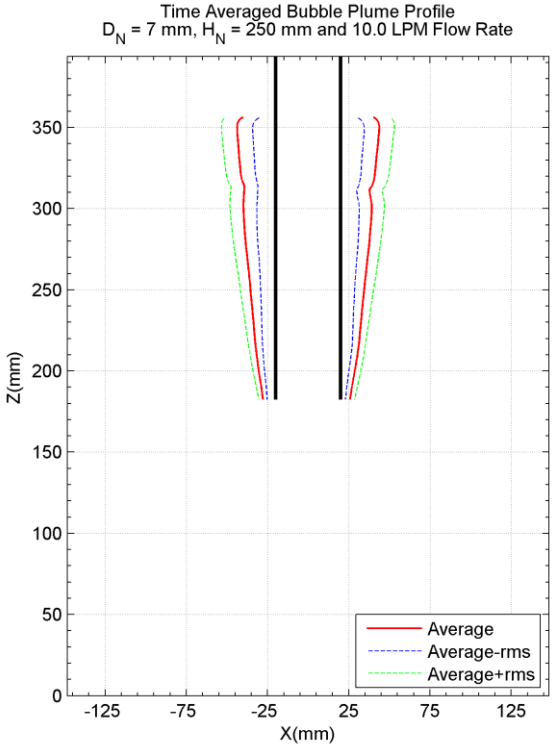

Figure C-14 D_N = 7 mm, H_N = 250 mm and Water Flow Rate = 10.0 LPM

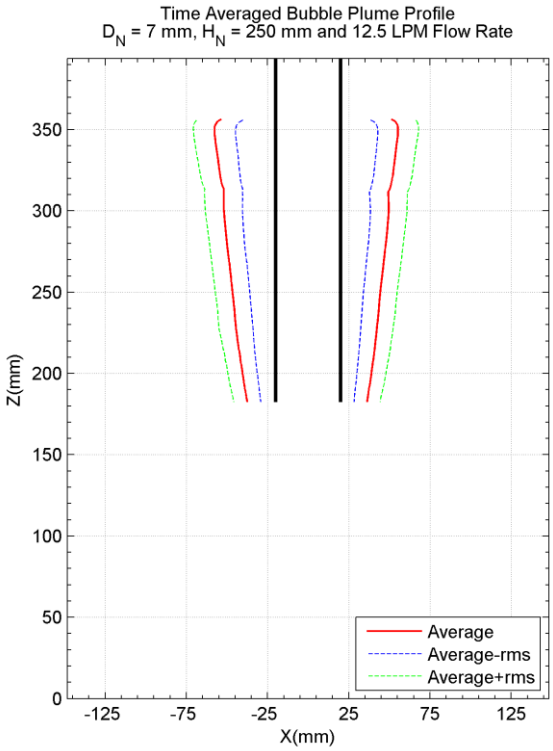

Figure C-15 D_N = 7 mm, H_N = 250 mm and Water Flow Rate = 12.5 LPM

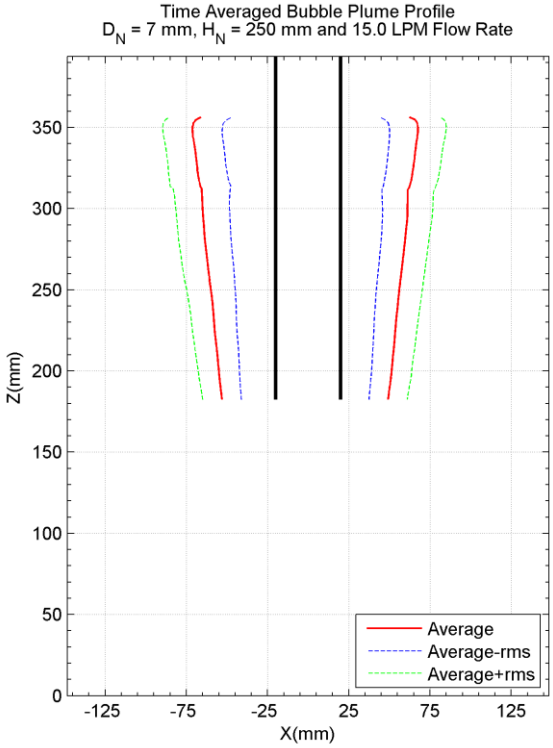

Figure C-16 D_N = 7 mm, H_N = 250 mm and Water Flow Rate = 15.0 LPM

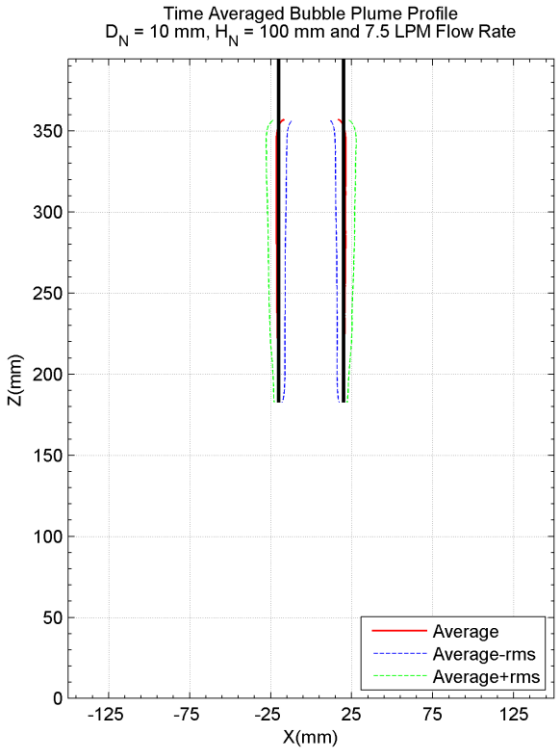

Figure C-17 D_N = 10 mm, H_N = 100 mm, Water Flow Rate = 7.5 LPM

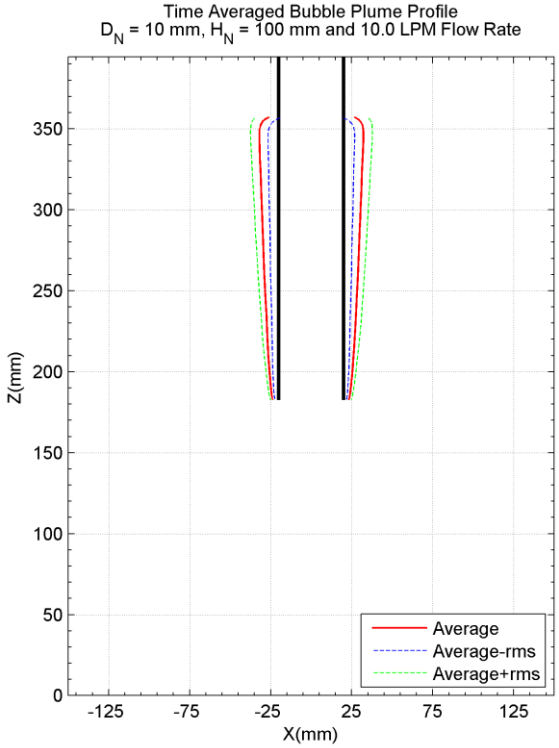

Figure C-18 D_N = 10 mm, H_N = 100 mm, Water Flow Rate = 10.0 LPM

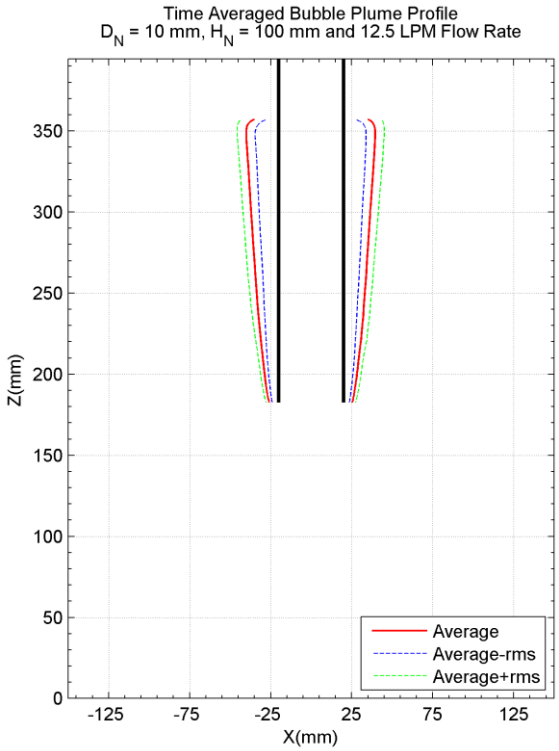

Figure C-19 D_N = 10 mm, H_N = 100 mm, Water Flow Rate = 12.5 LPM

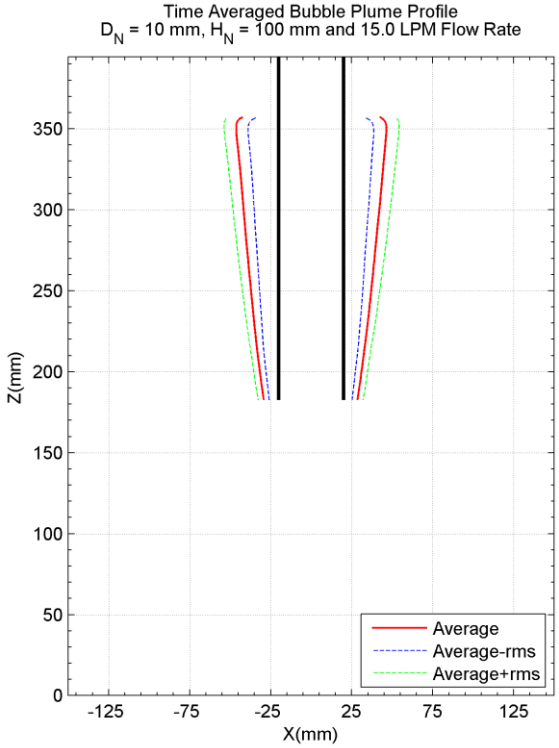

Figure C-20 D_N = 10 mm, H_N = 100 mm, Water Flow Rate = 15.0 LPM

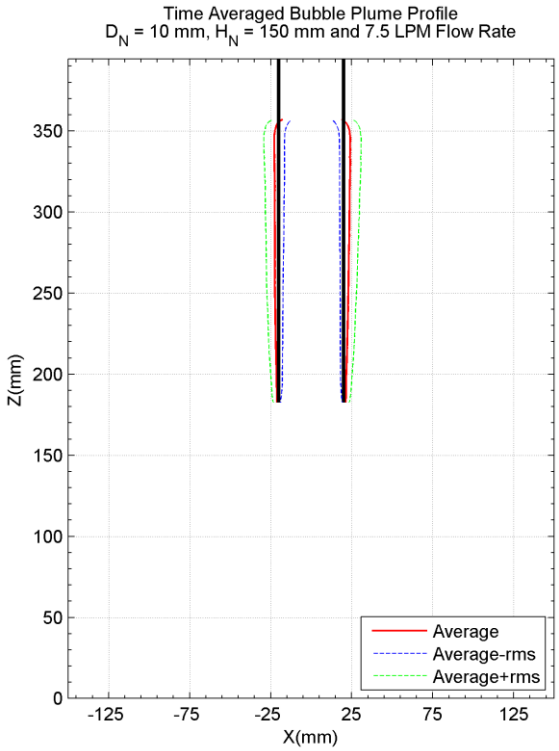

Figure C-21 D_N = 10 mm, H_N = 150 mm, Water Flow Rate = 7.5 LPM

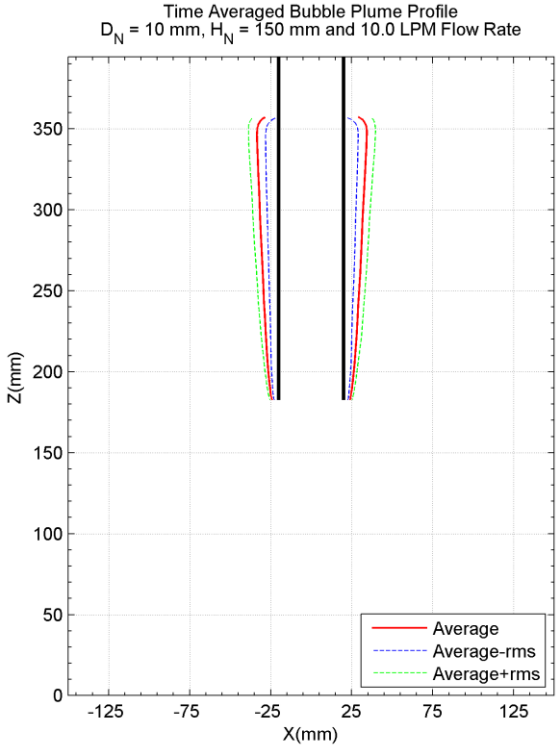

Figure C-22 D_N = 10 mm, H_N = 150 mm, Water Flow Rate = 10.0 LPM

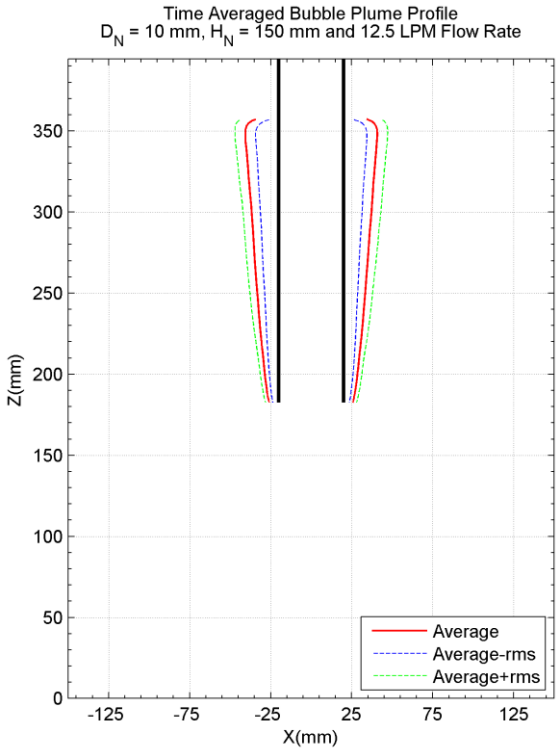

Figure C-23 D_N = 10 mm, H_N = 150 mm, Water Flow Rate = 12.5 LPM

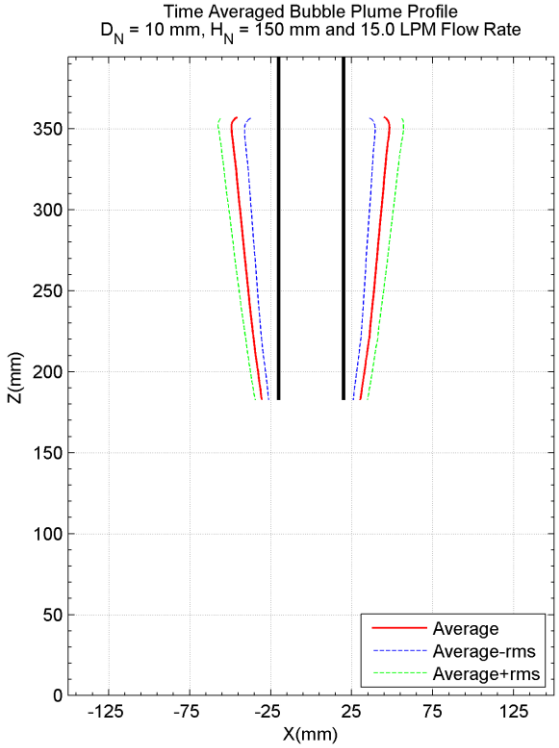

Figure C-24 D_N = 10 mm, H_N = 150 mm, Water Flow Rate = 15.0 LPM

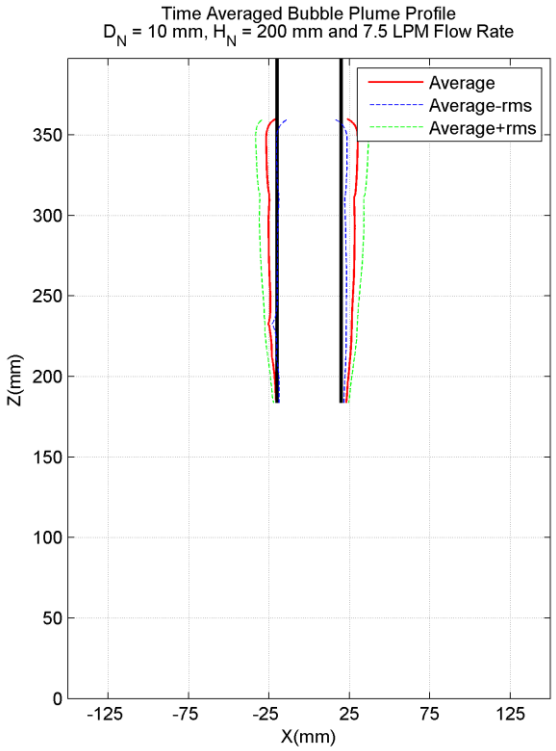

Figure C-25 D_N = 10 mm, H_N = 200 mm, Water Flow Rate = 7.5 LPM

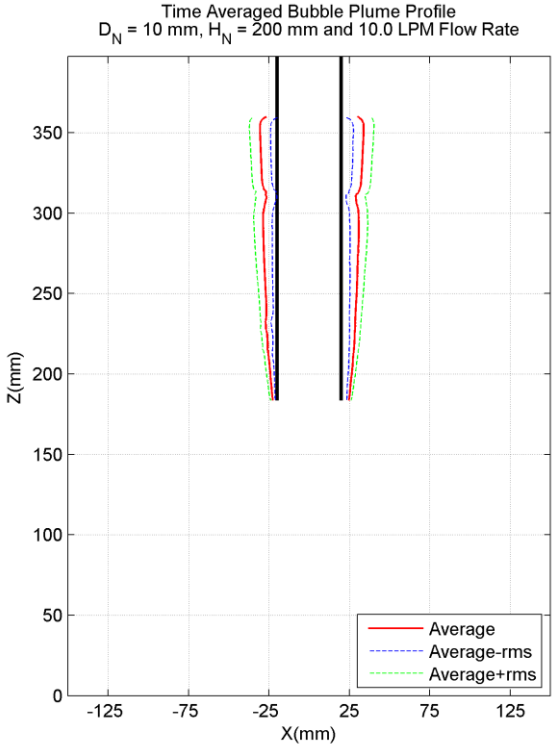

Figure C-26 D_N = 10 mm, H_N = 200 mm, Water Flow Rate = 10.0 LPM

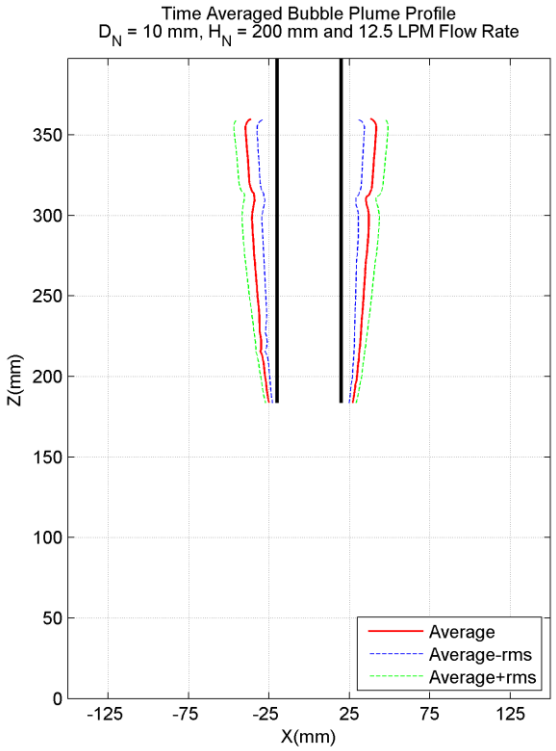

Figure C-27 D_N = 10 mm, H_N = 200 mm, Water Flow Rate = 12.5 LPM

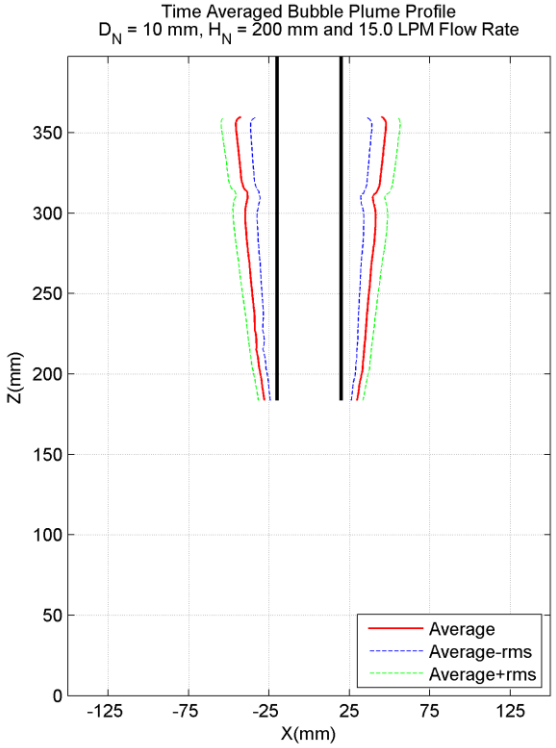

Figure C-28 D_N = 10 mm, H_N = 200 mm, Water Flow Rate = 15.0 LPM

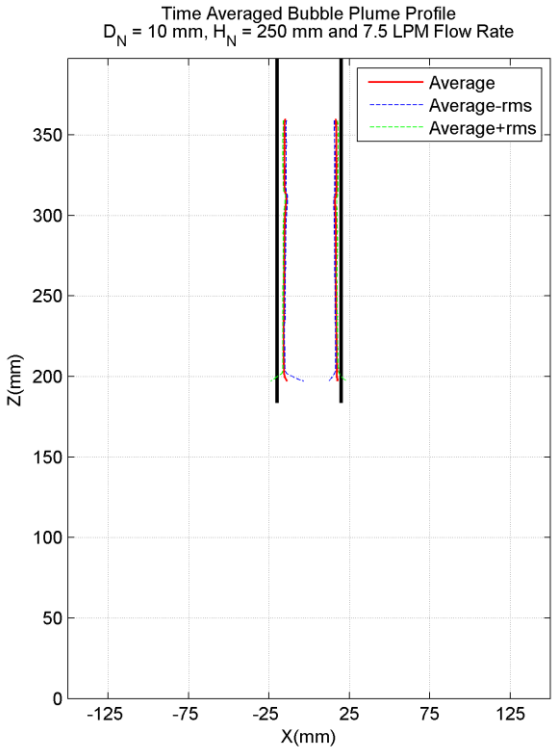

Figure C-29 D_N = 10 mm, H_N = 250 mm, Water Flow Rate = 7.5 LPM

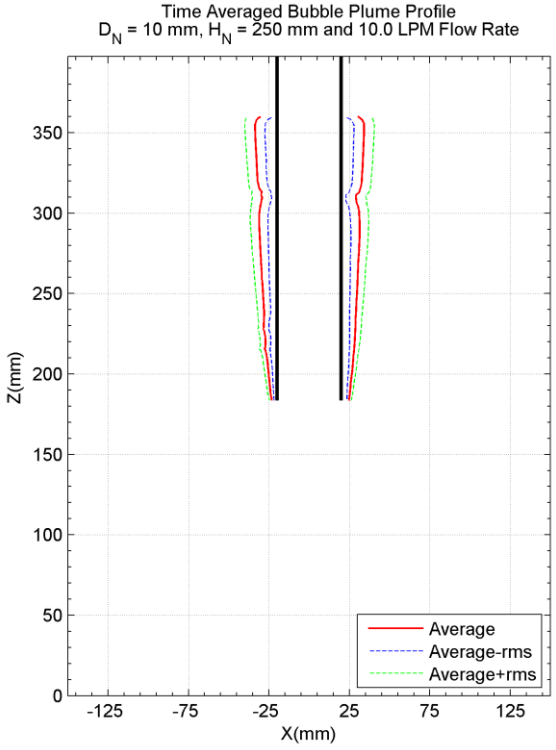

Figure C-30 D_N = 10 mm, H_N = 250 mm, Water Flow Rate = 10.0 LPM

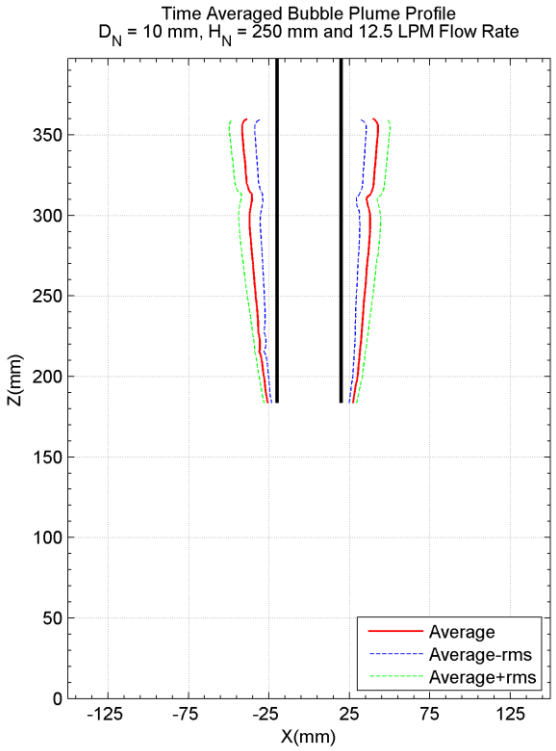

Figure C-31 D_N = 10 mm, H_N = 250 mm, Water Flow Rate = 12.5 LPM

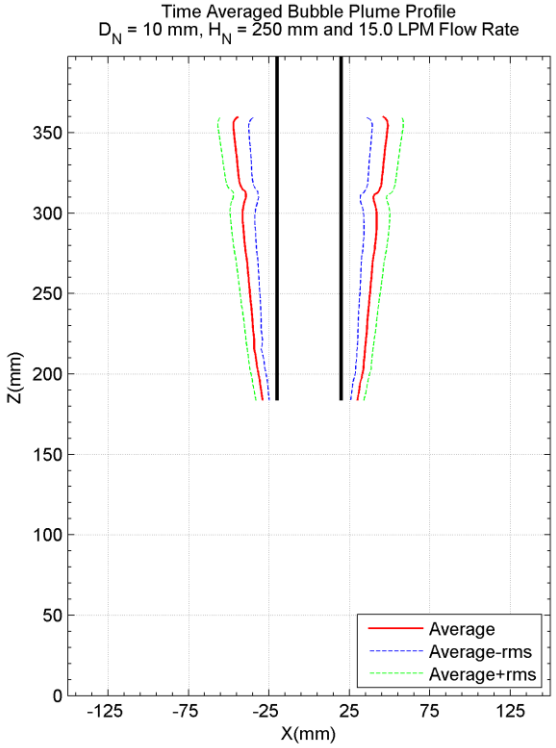

Figure C-32 D_N = 10 mm, H_N = 250 mm, Water Flow Rate = 15.0 LPM